THE KINETICS OF ORDERING, GRAIN GROWTH AND CHEMICAL SEGREGATION IN NONEQUILIBRIUM Fe_3X ALLOYS ($X = Al, Si$ and Ge)

Thesis by

Zheng-Qiang Gao

In Partial Fulfillment of the Requirements
for the Degree of
Doctor of Philosophy

California Institute of Technology
Pasadena, California

1994

(Defended May 18, 1994)

To my parents

and my wife

Acknowledgments

First and foremost, I would like to express my sincere gratitude to my advisor, Professor Brent Fultz, for his superb guidance, constant support and encouragement throughout my graduate studies at Caltech. His creativity, enthusiasm and technical insights have been my constant inspiration. His help is far beyond the limit of science, but also in language and culture adjustments. It has been a privilege to be a member of his highly motivated and talented group.

I have benefited greatly from the stimulating discussion and the courses offered by Professor William. L. Johnson and Dr. Channing Ahn. I also own special thanks to Carol Garland for her great assistance and instruction in operating electron microscope.

Many thanks go to the various past and present members of the Fultz group, especially Dr. James Okamoto, Dr. Hao Ouyang, Dr. Lawrence Anthony, Liubo Hong, Tab Stephens and Professor Chandrahas Bansal. Working with them makes scientific research a lot more fun. I would also like to thank Dr. Frank Shi, Dr. Carl Krill, Dr. Zezhong Fu, Dr. Yoshio Abe, Dr. Cho-Jen Tsai, Dr. Mo Li and Mohit Jain for their help and friendship.

This research was supported by the United States Department of Energy under grant DE-FG03-86ER45270 and the National Science Foundation under grant DMR-9213447. I would also like to thank Dr. Robert D. Shull of the National Institute of Standard and Technology for performing magnetic property measurements for us.

Finally, my deep gratitude goes to my parents. During those difficult years when I grew up, it was their love and encouragement that kept me in the right direction and progressed continually. I am very grateful to my wife, Ying, and my daughters, Diana and Nina, for their love and the happy time we shared during last a few years. I would also thank my sisters, Dr. Zhengping Gao and Dr. Zhenghong Gao, for their constant support and encouragement.

Abstract

Experimental studies on the kinetics of microstructural evolution in highly nonequilibrium Fe_3X based alloys (X = Al, Si and Ge) are the topic of this dissertation research. The kinetics of ordering especially, and other processes of microstructural evolution including grain growth and chemical segregation, were studied.

Materials far from their states of thermodynamic equilibrium were first prepared by rapid quenching and ball milling methods. Heat treatments at relatively low temperatures were used to allow the alloy microstructure to evolve towards equilibrium. Mössbauer spectroscopy was used heavily for measuring short range ordering, but X-ray diffractometry and transmission electron microscopy were also used extensively for microstructural characterization.

The initial states of the Fe_3X (X = Al, Si and Ge) binary alloys were chemically disordered bcc polycrystals (nearly random solid solution). Kinetics of disorder → order transformations were studied by plotting the kinetic paths through the space spanned by two order parameters. The kinetic paths for Fe_3Al showed a strong temperature dependence, but no temperature dependence was observed for kinetic paths of Fe_3Si and Fe_3Ge. A thermodynamically unexpected transient B32 ordered structure was observed in the early stages of ordering in Fe_3Al annealed at 300 °C.

The kinetics of microstructural evolution, especially grain growth was also studied on nanocrystalline $(Fe_3Si)_{0.95}Nb_{0.05}$ alloys. The Nb atoms were first forced into solid solution in bcc Fe-Si by ball milling. Upon annealing, Nb atoms segregated to grain boundaries, and impeded grain growth. The inter-dependence of grain growth, chemical segregation and chemical ordering was studied. A better understanding of such kinetics, we believe, can be an important step towards the controlled synthesis of new nonequilibrium materials.

Table of Contents

List of Figures

LRO parameters is slightly different, but nevertheless kinetic paths are different for samples annealed at different temperatures.

Figure 4.3 Mössbauer spectra of Fe_3Al as-quenched and after annealed at 300 °C for 392 hours.

Figure 4.4 Hyperfine magnetic field distributions for the as-quenched Fe_3Al sample and Fe_3Al samples after annealing at 300 °C for various times. Number on top of the figure identify the resonances from ^{57}Fe atoms with different numbers of 1nn Al atoms.

Figure 4.5 Experimentally derived kinetic paths of short range ordering (SRO) for Fe_3Al. The nearly-disordered initial state is on the lower left . The dotted lines were calculated by assuming the growth of $D0_3$ order only (center), 50% $D0_3$ order with 50% B2 order (top), and 25% $D0_3$ order with 75% B32 order (bottom).

Figure 4.6 Growth of superlattice diffraction peaks in initially piston-anvil quenched Fe_3Al samples annealed at 300 °C for various times.

Figure 4.7 Dark-field micrographs from (a) $(\frac{1}{2}\,\frac{1}{2}\,\frac{1}{2})$ and (b) (100) superlattice diffractions. The specimen was a foil of piston-anvil-quenched Fe_3Al that was annealed *in situ* at 300 °C for 1 hour with a heating holder in the transmission electron microscope. Simulated images with approximately the same scale are in the upper left-hand corners.

Figure 4.8 Evolution of B2, D03 and B32 order parameters with the kinetic master equation method ($V_{AA}{}^1 = V_{AA}{}^2 = 1.60$). (From Anthony and Fultz 1989a).

List of Tables

List of Publications

Parts of this thesis have been or will be published under the following titles:

Chapter 2

B. Fultz and Z. Q. Gao, "A Mössbauer Spectrometry Study of Hyperfine Magnetic Fields and Ordering in Fe_3Al," *Nucl. Instr. and Methods, Phys. Res. B,* **76**, 115 (1993).

B. Fultz, Z. Q. Gao, H. H. Hamdeh and S. R. Oliver, "Local and Nonlocal Isomer Shifts in bcc Fe-X Alloys (X=Al, Si, Ga, Ge)," *Phys. Rev.* B., **49**, 6312 (1994).

Chapter 3

B. Fultz and Z. Q. Gao, "A Mössbauer Spectrometry Study of Hyperfine Magnetic Fields and Ordering in Fe_3Al," *Nucl. Instr. and Methods, Phys. Res. B,* **76**, 115 (1993).

Chapter 4

C. Bansal, Z. Q. Gao, L. B. Hong and B. Fultz, "Phases and Phase Stabilities of Fe_3X alloys (X=Al, As, Ge, In, Sb, Si, Sn, Zn) Prepared by Mechanical Alloying," submitted to *J. Mater. Res.*

Z. Q. Gao and B. Fultz, "Kinetics of Ordering in Fe_3Al and Fe_3Si," *Hyperfine Interact.*, in press.

H. H. Hamdeh, J. Kramer, B. Fultz, Z. Q. Gao and S. A. Oliver, "Hyperfine Field and Chemical Ordering in Fe-Ge," *Hyperfine Interact.*, in press.

H. H. Hamdeh, S. A. Oliver, B. Fultz and Z. Q. Gao, "Structure and Magnetic Properties of Sputtered Thin Films of $Fe_{0.79}Ge_{0.21}$," *J. Appl. Phys.*, **74**, 5117 (1993).

Z. Q. Gao and B. Fultz, "Transient B32-like Order during the Early Stages of Ordering in Undercooled Fe_3Al," *Phil. Mag.* B, **67**, 787 (1993).

Z. Q. Gao and B. Fultz, "Transient B32-like Order in Nonequilibrium Fe_3Al," in *Kinetics of Ordering Transformations in Metals,* edited by H. Chen and V. K. Vasudevan, *TMS Symp. Proc.* 151 (1992).

B. Fultz, Z. Q. Gao and L. Anthony, "Kinetics of Ordering in Fe_3Al: Experiment," in *Alloy Phase Stability and Design,* edited by G. M. Stocks, D. P. Pope and A. F. Giamei, *Mater. Res. Soc. Symp. Proc.,* **186**, 187 (1991).

B. Fultz, Z. Q. Gao and H. H. Hamdeh, "Short Range Ordering in Fe_3Al: Experimental Study via Mössbauer Spectrometry," *Hyperfine Interact.* **54**, 799 (1990).

Chapter 5

Z. Q. Gao and B. Fultz, "Inter-dependence of Grain Growth, Nb Segregation and Chemical Ordering in Fe-Si-Nb Nanocrystals," submitted to *Nanostructured Materials*.

Z. Q. Gao and B. Fultz, "The Stability of Fe_3Si-Based Nanocrystalline Materials," *Hyperfine Interact.*, in press.

Z. Q. Gao and B. Fultz, "The Thermal Stability of Nanocrystalline Fe-Si-Nb Prepared by Mechanical Alloying," *Nanostructured Materials*, **2**, 231 (1993).

Chapter 1 Introduction

Highly nonequilibrium materials have been studied more and more intensively during the last few decades. The novel properties found in some of the most well-known highly nonequilibrium materials such as amorphous materials and more recently, nanocrystalline materials, further stimulated research in this field.

On the route to its state of thermodynamic equilibrium, an initially highly nonequilibrium system passes through a chain of kinetic states. Many kinetic phenomena, such as how the system chooses the intermediate states and how long is spent in these states, are still not well understood. The practical importance as well as the fundamental significance is obvious: a better understanding of the kinetics of relaxations in these highly nonequilibrium materials towards equilibrium is an important step towards the controlled synthesis of new nonequilibrium materials. In this dissertation research I started by studying the kinetics of the relaxation of one kind of highly nonequilibrium state: chemically disordered crystalline alloys. Later this work expanded to the more complex problem of stability of nanocrystalline materials.

§1.1 Disordered and Ordered States

Dissolving an atom species into another can result in an alloy where both species of atoms are distributed over the positions on one crystal lattice. In thermodynamic equilibrium, the randomness or order of this distribution depends on the competition between the internal energy and the product of temperature and entropy. For an alloy tending to develop chemical order, an increase in the probability of forming unlike atom pairs over the probability for a random distribution decreases the internal energy and the configurational entropy simultaneously. More recent study shows that the difference in vibrational entropy also plays a role in this competition (Anthony, Okamoto and Fultz 1993; Fultz, Nagel, Anthony and Okamoto 1994). Moreover the elastic distortions due to the differences in the atomic radii of the components as well as extended lattice defects such as grain boundaries, dislocations or stacking faults also may give rise to deviations from the random occupation of the lattice positions by the alloy atoms.

Throughout this thesis, "disordered" means that all the lattice positions are occupied by alloy atoms randomly, while "ordered" means that the lattice sites are grouped into sublattices, each of which is occupied predominantly by one species of atoms. Since the distribution of the atom species over the lattice sites depends on the strength of the interatomic interaction potentials compared to the actual temperature, temperature plays a critical role in this competition between disorder and order. There exits a "critical temperature" for long range ordering, above which long range order vanishes. R. W. Cahn makes a practical distinction between two types of ordering alloys (Cahn 1989; Cahn 1994): *permanently ordered alloys*, which are tenaciously ordered up to their melting point, and *reversibly ordered alloys*, which have a critical temperature for long range ordering below their melting point. The technological importance of the permanently ordered alloys is well-known; this class of materials includes structural aluminides, superconductors and hard ferromagnets. However, in studying disorder → order transformations, the same kinds of atom movements are expected in both reversibly ordered alloys and permanently ordered alloys.

§1.2 Kinetics of Disorder → Order Transformations

The theoretical study of the kinetics of ordering has been developed along two lines. The more conventional one is based on thermodynamic free energy control over the kinetics of ordering. From this theory, the rate of change of an order parameter, η, is expected to depend on the sensitivity of the free energy, F, to this order parameter (Khachaturyan 1975):

$$\frac{d\eta(t)}{dt} = \frac{L(\mathbf{k}_0)c(1-c)}{k_B T}\frac{\partial F(c,\eta)}{\partial \eta}, \tag{1.1}$$

where t is the time, c is the composition, k_B is the Boltzmann constant, T is an absolute temperature, and $\mathbf{k}_0$ is the superlattice wave vector within the Brillouin zone of the disordered alloy which generates the superstructure. $L(\mathbf{k}_0)$ is the kinetic coefficient related to the Fourier transform of probabilities of a diffusional jump during a time unit, so it is a mobility indicator that depends on the specific kinetic mechanism (a diffusion mechanism, for example).

The second way of studying the kinetics of ordering is based on activated state rate theory. This approach is basically an atomic diffusion theory used to predict rates of change of order parameters. In this theory the elementary kinetic step for atom movements in a lattice is considered to be the atom-vacancy exchange (or atom-atom exchange, but this is less realistic, especially at low temperature). The jump rate is determined by the activation energy barrier for the exchange and the interatomic interactions of the moving atom with its neighbors. Using the example of binary alloy, the jump rate, Γ_A, for an A atom is:

$$\Gamma_A = \nu n_v \exp\left(E_A^*\right) \exp\left(n_A V_{AA} + n_B V_{AB}\right), \tag{1.2}$$

where n_V is the number of vacancy neighbors, n_A is the number of like neighbors (A atoms) and n_B is the number of unlike neighbors (B atoms). ($n_A + n_B + n_V = z$, and z is the lattice coordination number.) ν is the attempt frequency and $E_A{}^*$ is an activation energy barrier for the A atom. V_{AA} and V_{AB} are the A-A and A-B pair interaction energies, respectively. (The energies are in units of kT.)

Analytical calculations have done based on the activated state rate theory, most notably the master equation method in the point (or Bragg-Williams) approximation (Anthony and Fultz 1989), and the path probability method or master equation method in the pair (or Bethe) approximation (Kikuchi 1960 and 1966; Sato and Kikuchi 1976; Gschwend, Sato and Kikuchi 1978; Fultz 1991b and 1992; Anthony and Fultz 1991 and 1994). Monte Carlo simulations were also used to study the kinetics of ordering, and these Monte Carlo simulations employ a single vacancy and the same mechanism of atom movement as the analytical theories (Anthony and Fultz 1991 and 1994).

Most previous experimental studies of disorder → order transformations were performed on states not far from thermodynamic equilibrium, usually on reversibly ordered alloys, and usually near their critical temperatures for ordering. Such work includes studies of Fe_3Al (Lawley, Vidoz and Cahn 1961; Lawley and Cahn 1961; Naumova, Semenovskaya and Umamskii 1970; Naumova and Semenovskaya 1971; Oki, Hasaka and Eguchi 1974; Park, Stephenson, Allen and Ludwig 1992), FeCo (English 1966; Clegg and Buckley 1973; Buckley 1975; Mal'tsev, Goman'kov, Puzey, Makarov and Kozis 1975; Smith and Rawlings 1976; Seehra and Silinsky 1976), Ni_3Fe (Calvayrac and Fayard 1973; Morris, Brown, Piller and Smallman 1976; Drijver, van de Woude and Radelaar 1975), Cu_3Au (Nagy and Nagy 1962; Hashimoto, Miyoshi and Ohtsuke 1976) and Ni_3Mn (Collins and Teh 1973; Hatta and Shiboya 1978). More recent research put more emphasis on synthesizing disordered alloys that are far from thermodynamic equilibrium (i.e., with large stored enthalpies). For example, using less conventional techniques, chemically disordered Ni_3Al, a permanently ordered alloy, was obtained by high vacuum evaporation (Harris, Pearson and Fultz 1991), sputtering (Sumiyama, Hirose and Nakamura 1989), laser quenching (West, Manos and Aziz 1991), irradiating (Carpenter and Schulson 1981) and ball milling (Jang and Koch 1990, Gianella, Cahn, Malagelada, Surinach and Baro 1991).

In this dissertation, I will present experimental results on the preparation of disordered Fe_3X (X = Al, Si and Ge) binary alloys that are far from their states of thermodynamic equilibrium. These materials were then used for studies of the kinetics of ordering and the kinetics of other processes of microstructural evolution (grain growth and chemical segregation).

§1.3 Possible Ordered States and Ground States of bcc Fe_3X Alloys

The $D0_3$, B2 and B32 structures are three possible bcc-based ordered structures for the Fe_3X stoichiometry (X = Al, Si and Ge). The notation for the disordered structure on the bcc lattice is A2. These ordered structures can be best described with a four-sublattice model. As shown in Figure 1.1, a bcc lattice can be divided into four interpenetrating fcc sublattices with a doubled lattice parameter,

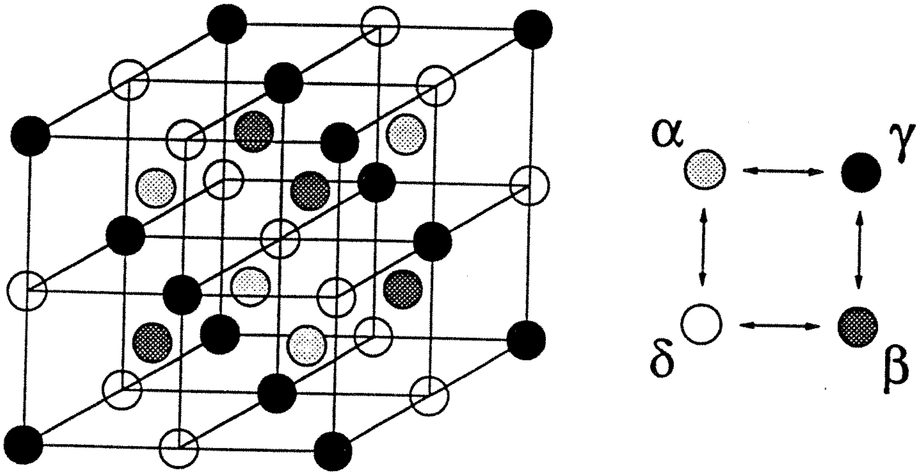

Figure 1.1 Four sublattice model for bcc lattice. A bcc lattice is divided into four interpenetrating fcc sublattices. The arrows indicate the nearest neighbor relations between pairs of sublattices.

representing four possible atomic sites. The arrows between the sublattice symbols indicate pairs of sublattice with atoms as first nearest neighbors.

In the disordered state (A2), there is no preference of Fe or the solute atoms for any of the four sublattices, so the atoms occupy all lattice sites randomly (Figure 1.2a). If the alloy has $D0_3$ order, then all the solute atoms will occupy one of the four sublattices (for example, the α sublattice) and Fe atoms will occupy the other three (β, γ and δ) (Figure 1.2b). If the alloy has B2 order, two non-adjacent sublattices (e.g., α and β) are occupied by iron atoms exclusively, and the other two are occupied by 50% iron, 50% solute atoms randomly (Figure 1.2c). For the other possible ordered structure, B32 order, two adjacent sublattices (e.g., α and γ) are occupied by iron atoms exclusively, and the other two (β and δ) are occupied by 50% iron and 50% solute atoms randomly (Figure 1.2d).

It is also interesting, and very useful for Chapter 4, to look at the probability distribution of solute atoms in the first nearest neighbor (1nn) shell of Fe atoms for the four ordered structures of the Fe_3X stoichiometry (Figure 1.2). Figure 1.3 presents the calculated probabilities of Fe atoms with different numbers of solute atoms in their 1nn shell for A2 , B2, B32 and $D0_3$ structures. For the disordered A2 structure, the solute atoms are distributed randomly on the eight sites in the 1nn shell of Fe, so the probability distribution is a binomial distribution:

$$\mathcal{F}_{A2} = f(x, 8, 0.25) = \binom{8}{x} 0.25^{x} (1-0.25)^{8-x}, \quad x = 0, 1, 2, ..., 8. \tag{1.3}$$

For the B32 ordered structure, the solute atoms are distributed randomly on four sites, instead of all eight sites, in the 1nn shell of Fe. The other four sites are occupied by other Fe atoms, so the probability distribution for B32 order is still a binomial

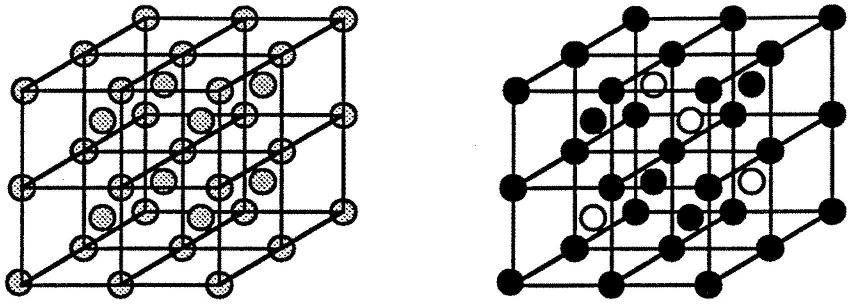

(a): A2 or bcc disorder

(b): D0$_3$ order

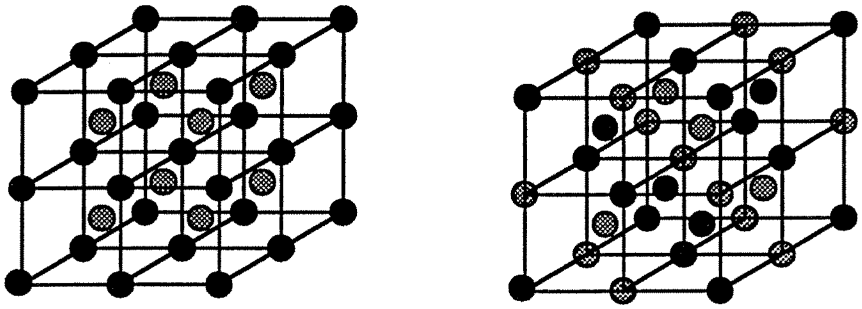

(c): B2 order

(d): B32 order

Figure 1.2 Four possible ordered states for bcc lattice of A_3B stoichiometry. (●: pure Fe atom; ▩: 50% Fe atom and 50% solute atom randomly; ◍: 75% Fe atom and 25% solute atom randomly; and ○: pure solue atom.)

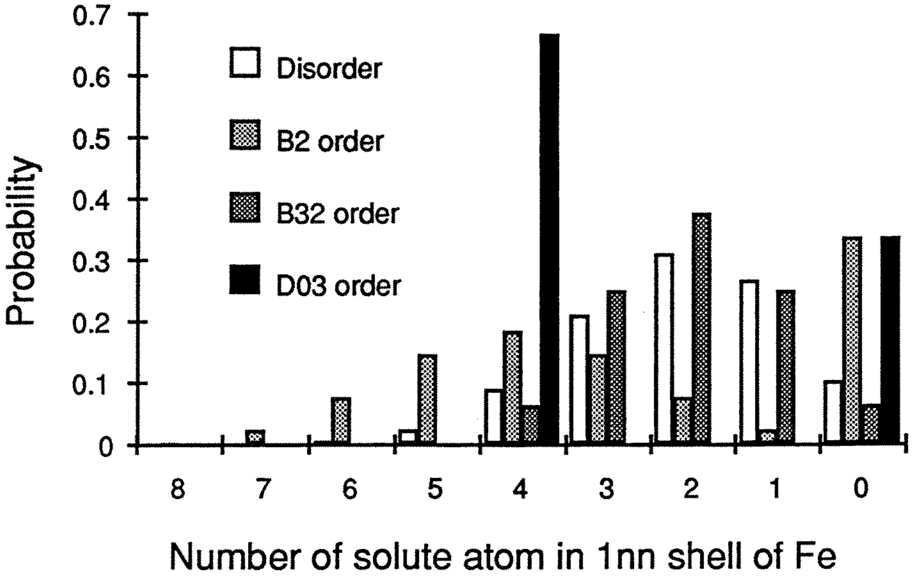

Figure 1.3 Calculated probabilities of Fe atoms with different numbers of solute atoms in their 1nn shell for A2, B2, B32 and $D0_3$ ordered structures.

distribution but involving only four sites. The distribution of solute atoms in the 1nn shell of an Fe atom is:

$$\mathcal{F}_{B32}=f(x, 4, 0.5)=\binom{4}{x}0.5^{x}(1-0.5)^{8-x}, \quad x=0, 1, 2, 3, 4. \tag{1.4}$$

In the B2 structure, one third of the Fe atoms are surrounded by eight Fe atoms and two thirds of the Fe atoms are surrounded by four Fe atoms and four solute atoms distributed randomly. The distribution gives:

$$\begin{aligned}\mathcal{F}_{B2}&=\frac{2}{3}f(x, 8, 0.5)+\frac{1}{3}\delta(0)\\ &=\frac{2}{3}\binom{8}{x}0.5^{x}(1-0.5)^{8-x}+\frac{1}{3}\delta(0), \quad x=0, 1, 2,..., 8.\end{aligned} \tag{1.5}$$

Finally for the D0$_3$ ordered structure, there are two different Fe sites. One is surrounded by eight Fe atoms, the other is surrounded by four Fe atoms and four solute atoms. The probability distribution is:

$$\mathcal{F}_{D03}=\frac{2}{3}\delta(4)+\frac{1}{3}\delta(0). \tag{1.4}$$

Richards, Allen, and Cahn analyzed the ground state structures of bcc ordered alloys (Richards and Cahn 1971; Allen and Cahn 1972). For different chemical compositions, they classified the ground state ordered structures in terms of the signs and strengths of the first- and second-nearest neighbor (1nn and 2nn) interatomic interactions. The ground states for bcc alloys of the A$_3$B stoichiometry, are shown in Figure 1.4 (Anthony 1993).

§ 1.4 Overview

The main topic of this thesis is the experimental study of the kinetics of

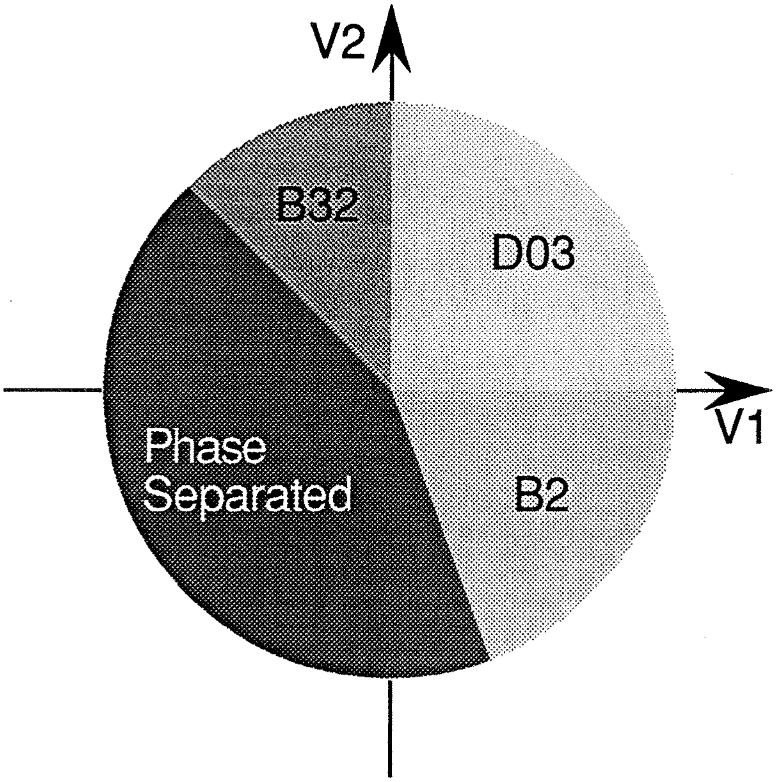

Figure 1.4 Ground states for bcc binary alloys of the A_3B stoichiometry and with different 1nn and 2nn interatomic interactions, V1 and V2, respectively. (From Anthony 1993)

ordering and other processes of microstructural evolution in highly nonequilibrium materials. Since Mössbauer spectrometry was used extensively, in the second chapter I will explain the physical background as well as theoretical models used to interpret experimental data. The experimental procedures, including the techniques used to synthesize highly nonequilibrium materials and characterize their microstructures, are discussed in Chapter 3.

In analytical studies of the kinetics of ordering, "kinetic paths," that are chains of states connecting the initial disordered state to the final equilibrium state (Fultz 1991), were found to be significantly different at different temperatures or with different chemical interactions, even though the final equilibrium state was unchanged, or changed only insignificantly. The same idea of "kinetic paths" was used in this experimental work and in the fourth chapter I present studies of "kinetic paths" for Fe_3Al, Fe_3Si and Fe_3Ge alloys at different temperatures. I also present, in Chapter 4, an experimental observation of transient B32 ordered structure that appears in the early stages of ordering in Fe_3Al. This structure, incompatible with thermodynamic arguments, was predicted in previous analytical studies of ordering for bcc lattices (Anthony and Fultz 1989, 1994).

In Chapter 5 the kinetics of ordering, as well as the kinetics of grain growth and chemical segregation, were investigated for $(Fe_3Si)_{0.95}Nb_{0.05}$ nanocrystalline materials. This investigation unveiled the inter-dependency between chemical ordering, chemical segregation and grain growth. The results could be of practical use in determining the optimum heat treatment for nanocrystalline Fe-Si-Nb alloy to obtain a small grain with minimum strain, and thus optimal soft magnetic properties.

In the final chapter, a summary of the results of my research and a perspective are presented.

References

ALLEN, S. M., and CAHN, J. W., *Acta Metall.* **20**, 423 (1972).

ALLEN, S. M., and CAHN, J. W., *Acta Metall.* **23**, 1017 (1975).

ALLEN, S. M., and CAHN, J. W., *Acta Metall.* **24**, 425 (1976).

ANTHONY, L. and FULTZ, B.: in Alloy Phase Stability and Design, G. M. Stocks, D. P. Pope and A. F. Giamei, eds., (*Mat. Res. Soc. Symp. Proc.*, **186**, Pittsburgh, PA, 1991), p. 181.

ANTHONY, L. and FULTZ, B.: *J. Mater. Res.*, **4**, 1132 (1989).

ANTHONY, L. and FULTZ, B.: *J. Mater. Res.*, **9**, 348 (1994).

ANTHONY, L.; OKAMOTO; J. K. and FULTZ, B.: *Phys. Rev. Lett.*, **70**, 1128 (1993).

ANTHONY; L.: Ph.D. Thesis, California Institute of Technology, 1993.

BUCKLEY, R. A.: *Metal Sci.*, **9**, 243 (1975).

CAHN, R. W.: "The Place of Atomic Order in the Physics of Solids and in Metallurgy," in Physics of New Materials - A Status Report, F. E. Fujita ed., (Springer-Verlag, Berlin, Heidelberg 1994), Chapter 7, p. 179.

CAHN, R. W.: *Metals Materials and Processes*, **1**, 1 (1989).

CALVAYRAC, Y. and FAYARD, M.: *Phys. Stat. Solid.*, **(a)** **17**, 407 (1973).

CARPENTER, L. J. C. and SCHULSON, E. M.: *Scripta Metall.*, **15**, 549 (1981).

CLEGG, D. W. and BUCKLEY, R. A.: *Metal. Sci.*, **7**, 48 (1973).

COLLINS, M. R. and TEH, H. C.: *Phys. Rev. Lett.*, **30**, 781 (1973).

DRIJVER, J. F.; VAN DE WOUDE, F. and RADELAAR, S.: *Phys. Rev. Lett.*, **34**, 1026 (1975).

ENGLISH, A. T.: *Trans. AIME*, **236**, 12 (1966).

FULTZ, B.; NAGEL; L. J., ANTHONY; L. and OKAMOTO, J. K.: submitted to *Phys. Rev. Lett.*, (1994).

FULTZ, B.: *J. Lessc. Met.*, **168**, 145 (1991a).

FULTZ, B.: J. *Mater. Res.*, **7**, 946 (1992).

FULTZ, B.: *Phys. Rev.*, **B 44**, 9805 (1991b).

GIANELLA, S.; CAHN, R. W.; MALAGELADA, J.; SURINACH, S. and BARO, M. D.: "Disordering of Ni_3Al by Ball-Milling," in Ordering and Disordering in Alloys, A. R. Yavari, ed., (Elsevier Applied Science, New York, 1991).

GSCHWEND, K.; SATO, H. and KIKUCHI, R.: *J. Chem. Phys.*, **69**, 5006 (1978).

HARRIS, S. R.; PEARSON, D. H.; GARLAND, C. M. and FULTZ, B.: *J. Mater. Res.*, **6**, 2019 (1991).

HASHIMOTO, T.; MIYOSHI, T. and OHTSUKE, H.: *Phys. Rev.*, **B 13**, 1119 (1976).

HATTA, I. and SHIBOYA, M.: *J. Phys. Soc. Japan,* **45**, 487 (1978).

JANG, J. S. C. and KOCH, C. C.: *J. Mater. Res.*, **5**, 498 (1990).

KHACHATURYAN, A. G.: "Ordering in Substitutional and Interstitial Solid Solutions," in Progress in Materials Science, ed. by B. Chalmers, J. W. Christian and T. Massalski, 22, (Pergamon Press, Oxford, 1975), p. 1.

KIKUCHI, R.: *Ann. Phys.*, **10**, 127 (1960).

KIKUCHI, R.: *Prog. Theor. Phys. Suppl.*, **35**, 1 (1966).

LAWLEY, A. and CAHN, R. W.: *J. Phys. Chem. Solids*, **20**, 203 (1961).

LAWLEY, A.; VIDOZ, E. A. and CAHN, R. W.: *Acta Metall.*, **9**, 287 (1961).

MAL'TSEV, Y. I.; GOMAN'KOV, V. I.; PUZEY, I. M.; MAKAROV, V. A. and KOZIS, Y. V.: *Fiz. Metal. Metalloved.*, **39**, 543 (1975).

MORRIS, D. G.; BROWM, G. T.; PILLER, R. C. and SMALLMAN, R. E.: *Acta Metall.*, **24**, 21 (1976).

NAGY, E. and NAGY, I.: *J. Phys. Chem. Solids*, **23**, 1605 (1962).

NAUMOVA, M. M. and SEMENOVSLAYA, S. V.: *Sov. Phys. - Solid State*, **12(12)**, 2954 (1971).

NAUMOVA, M. M.; SEMENOVSLAYA, S. V. and UMANSKII, Y. S.: *Sov. Phys. - Solid State*, **12(4)**, 764 (1970).

OKI, K.; HASAKA, M. and EGUCHI, T.: *Japan J. Appl. Phys.*, **12**, 143 (1974).

PARK, B.; STEPHENSON, G. B.; ALLEN, S. M. and LUDWIG, K. F.: *Phys. Rev. Lett.*, **68**, 1742 (1992).

RICHARDS, M. J., and CAHN, J. W., *Acta Metall.* **19**, 1263 (1971).

SATO, H. and KIKUCHI, R.: *Acta Metall.*, **24**, 797 (1976).

SEEHRA, M. S. and SILINSKY, P.: *Phys. Rev.*, **B 13**, 5183 (1976).

SMITH, A. W. and RAWINGS, R. D.: *Phys. Stat. Solid.*, **(a) 34**, 117 (1976).

SUMIYAMA, K.; HIROSE, H. and NAKAMURA, Y.: *Phys. Stat. Solidi.*, **(a) 114**, 693 (1989).

WEST, J. A.; MANOS, J. T. and AZIZ, M. J.: *Mat. Res. Soc. Symp. Proc.*, **213**, (1991).

Chapter 2 Mössbauer Effect and Hyperfine Magnetic Fields

Since Mössbauer spectroscopy was used extensively in this thesis research, in this chapter I will discuss some fundamental features of the Mössbauer effect. In the first section I will explain the basic idea and physical background of the Mössbauer effect. Then in the second section, I will discuss the general features of hyperfine interactions and their effects on Mössbauer spectra. Finally in the third section, I will discuss in more detail the solute-induced perturbations of ^{57}Fe hyperfine magnetic fields. These perturbations will be used extensively in this thesis research to measure local chemical environments in iron alloys.

§2.1 Introduction to the Mössbauer Effect

Using classical physics, we can calculate the recoil energy, E_R, when a γ-ray photon is emitted from a nucleus at rest:

$$E_R = \frac{p_\gamma^2}{2M} = \frac{E_\gamma^2}{2Mc^2} \approx \frac{E_0^2}{2Mc^2}, \tag{2.1}$$

where p_γ, E_γ are the momentum and energy of emitted γ-ray photon, and $E_\gamma \approx E_0$, the change of the energy level because of the emission of γ-photon. Using the first excited state of ^{57}Fe as an example, $E_0 = 14.4$ keV and $M = 57$ g/mol, we get $E_R \approx 2\text{x}10^{-3}$ eV.

From the uncertainty principle, we can estimate the natural linewidth for the excited state as:

$$\Gamma \approx \frac{h}{2\pi\tau}, \tag{2.2}$$

where h is Planck's constant, and τ is the mean lifetime of the excited state. Also using the first excited state of ^{57}Fe as example, $\tau = 140$ nsec, and we get the natural linewidth $\Gamma \approx 5\text{x}10^{-9}$ eV. The nuclear resonance is very sharp, having an energy-to-linewidth ratio, Q, of 14.4 keV/5x10^{-9} eV $\approx$ 3x10^{12}.

The recoil energy loss, when it occurs on a free nucleus, can cause a displacement between emission and absorption line which can be a million times larger than the natural linewidth, thus breaking the condition for resonance. Resonant absorption of the γ-ray by a second nucleus will not occur if energy is lost in the recoil of the nucleus that emits the γ-ray.

However, if both the source nucleus and the absorber nucleus are embedded in crystal lattice, the recoil momentum does not always induce a change in the phonon spectrum of the crystal. The existence of such a zero-phonon process makes it possible for γ-rays to be emitted and absorbed by nuclei with negligible recoil energy transferred to internal excitations of the lattice. (Or we can still use the classical argument: as M becomes the mass of the whole lattice instead of being the mass of only one nucleus, it is more than a million times larger, and thus E_R becomes more than a million times smaller.)

Recoilless nuclear resonance was first discovered and interpreted by Rudolf L. Mössbauer in 1958 (Mössbauer 1958) Since then, it has become a powerful tool in many disciplines of natural science ranging from nuclear physics to biology.

Recoil-Free Fraction

From general quantum mechanics (Debrunner and Frauenfelder 1971), when a γ-ray photon is emitted or absorbed by a nucleus in a crystal, the probability of the crystal vibrational state changing from its initial state $\langle i|$ to a final state $\langle j|$ is: $\left|\langle j|e^{i\mathbf{k}\cdot\mathbf{x}}|i\rangle\right|^2$. Here **k** is the wave vector of γ-ray, and **x** is the coordinate of the center mass of the decaying nucleus. If $\langle i| = \langle j|$, that is, the γ-ray photon is emitted or absorbed without an energy level change of the lattice, then we have the probability or fraction of the number of recoilless γ-ray resonance events (emission or absorption). This probability is defined as the "*recoil-free fraction*":

$$f=\left|\langle i|e^{i\mathbf{k}\cdot\mathbf{x}}|i\rangle\right|^2. \tag{2.3}$$

A simple Einstein model for lattice vibrations predicts:

$$f=\exp\left(-k^2\left\langle x^2\right\rangle\right)=\exp\left(-\frac{4\pi^2\left\langle x^2\right\rangle}{\lambda^2}\right), \tag{2.4}$$

where $<x^2>$ is the mean-square vibrational amplitude, and λ is the wavelength of the γ-ray. With this equation we have obtained an important result for the Mössbauer effect: (1) the recoil-free fraction decreases with decreasing λ, i.e., higher energy γ-rays, and (2) the recoil-free fraction is a measure of the vibrational amplitude of the resonating atom in the direction of observation. Higher temperatures will increase $<x^2>$, and thus decrease the recoil-free fraction.

To get a more accurate result, a Debye model can be used to consider the large number of oscillator levels in the solid and their frequency distribution. The Debye model gives the following expression for the recoil-free fraction (Gonser 1975):

$$f=\exp\left\{-\frac{3E_R}{2k_B\theta_D}\left[1+4\left(\frac{T}{\theta_D}\right)^2\int_0^{\theta_D/T}\frac{x\,dx}{e^x-1}\right]\right\}, \tag{2.5}$$

where E_R is the recoil energy of free atom, T is the temperature, and θ_D is the Debye temperature. In the limit of low or high temperature we obtain approximately:

$$f=\exp\left[-\frac{3}{2}\frac{E_R}{k_B\theta_D}\right], \qquad T \ll \theta_D; \tag{2.6a}$$

$$f=\exp\left[-\frac{6E_R}{k_B\theta_D}\frac{T}{\theta_D}\right], \qquad T > \theta_D. \tag{2.6b}$$

The recoil-free fraction for bcc iron alloys at room temperature is about 0.7 to 0.8. More importantly, the variation in recoil-free fraction with temperature for bcc iron alloys is not large up to fairly high temperature (~1000 K), so Mössbauer studies on these alloys can be done at a relatively large temperature range.

Transmission Intensity

The energy distribution of both the emitted γ-ray and the absorption level of a nucleus in the sample are Lorentzian functions (Jackson 1955). The observed absorption is thus the convolution of these two distributions (Cowley 1981). Neglecting the self-absorption of γ-rays by the source (Atsushi 1974), the transmitted intensity of the Mössbauer spectrum of ^{57}Fe for a sample of uniform thickness, t, is given as a function of Doppler velocity, v, by (Margulies and Ehrman 1961):

$$P(v)=(1-f_s)+f_s\int_{-\infty}^{\infty} S(E-v)\exp\left(-\frac{T\Gamma^2/4}{(E-V_0)^2+\Gamma^2/4}\right)dE, \tag{2.7}$$

where

$V_0 = V_A - V_S,$

V_S = centroid of the emitted γ-ray energy spread when $v = 0$,

V_A = centroid of the absorption energy level spread,

f_S = recoil-free fraction for the source,

$S(E) = \frac{2}{\pi\tau} \frac{T\Gamma^2/4}{E^2+\Gamma^2/4}$, energy distribution function of the γ-ray,

Γ = half width of the energy distribution = 4.67×10^{-9} eV = 0.097 mm/sec,

(for first active state of ^{57}Fe at 14.4 keV,)

$T = f_A\, n_A\, a_A\, \sigma_0\, t$, an normalized thickness,

f_A = recoil-free fraction for the absorber,

n_A = number of iron nuclei per cm^3 in the absorber,

a_A = fractional abundance of the ^{57}Fe isotope in the absorber,

σ_0 = total absorption cross section.

If there are several absorption levels, Equation (2.7) becomes:

$$P(v)=(1-f_s)+f_s \int_{-\infty}^{\infty} S(E-v)\exp\left(-\sum_i \frac{Tq_i\Gamma^2/4}{(E-V_i)^2+\Gamma^2/4}\right)dE, \tag{2.8}$$

where q_i is the normalized probability of the ith transition ($\sum_i q_i=1$), and V_i is the difference between the centroid of the ith absorption level and that of the emitted γ-ray when $v = 0$.

For a very thin absorber, $T \ll 1$, the exponential in Equation (2.6) can be linearized and:

$$P(v)\approx 1-f_s\sum_i \frac{Tq_i}{2}\frac{\Gamma^2}{(v-V_i)^2+\Gamma^2}.$$

$$=1-f_s\sum_i L_i(v), \tag{2.9}$$

where the Lorentzian function, L_i, is defined as:

$$L_i(v) = \frac{Tq_i}{2} \frac{\Gamma^2}{(v - V_i)^2 + \Gamma^2}. \tag{2.10}$$

In summary, for thin absorbers, in practice 5 μ m for pure natural iron, the transmission intensity is proportional to the recoil-free fraction, and the peak shape is a sum of Lorentzian functions.

Mössbauer Spectrometry

The nuclear absorption energies are perturbed slightly by the solid in which the nuclei are incorporated. The absorption profile as a function of the energy of the emitted γ-ray can then be used to study the local chemical environment surrounding the nuclei. The method of studying local atomic arrangements in materials using absorption profiles is what I call *Mössbauer Spectrometry*.

The γ-ray energy shift in an experiment is accomplished by mechanically moving the radiation source. With a velocity v (positive when moving towards the absorber), the change of energy of the emitted γ-ray is

$$\Delta E = (v/c)E_0, \tag{2.11}$$

where c is the speed of light, and v is typically within about 1 cm/sec. The disparity between v and c is appropriate for a resonance with a Q (energy-to-linewidth ratio) of $\sim 10^{13}$.

Figure 2.1 shows two geometrical arrangements for measuring a Mössbauer spectrum. In transmission geometry, as the energy of γ-ray matches the excitation energy of nuclei in the absorber, the nuclear resonance causes greater absorption and therefore peaks of reduced intensity. In scattering geometry, at nuclear resonance the re-emitted radiations result in peaks of higher counting rate. In many Mössbauer

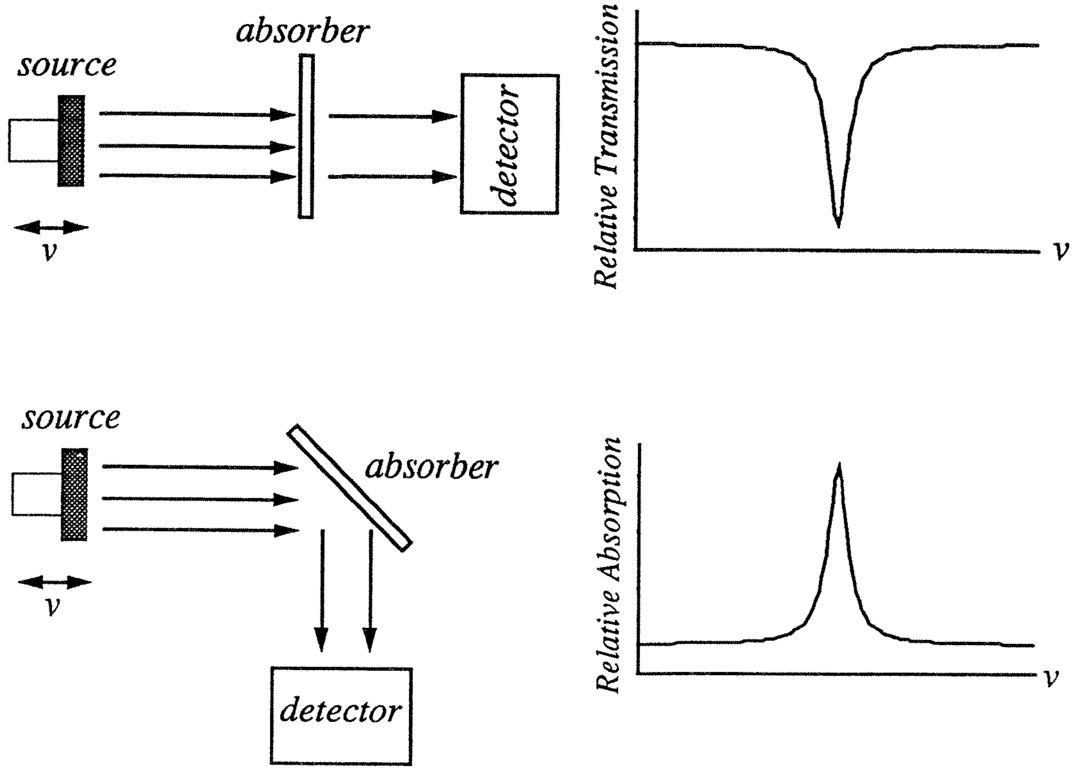

Figure 2.1 Schematic of experimental arrangements for obtaining Mössbauer spectra in transmission geometry (upper) and scattering geometry (lower).

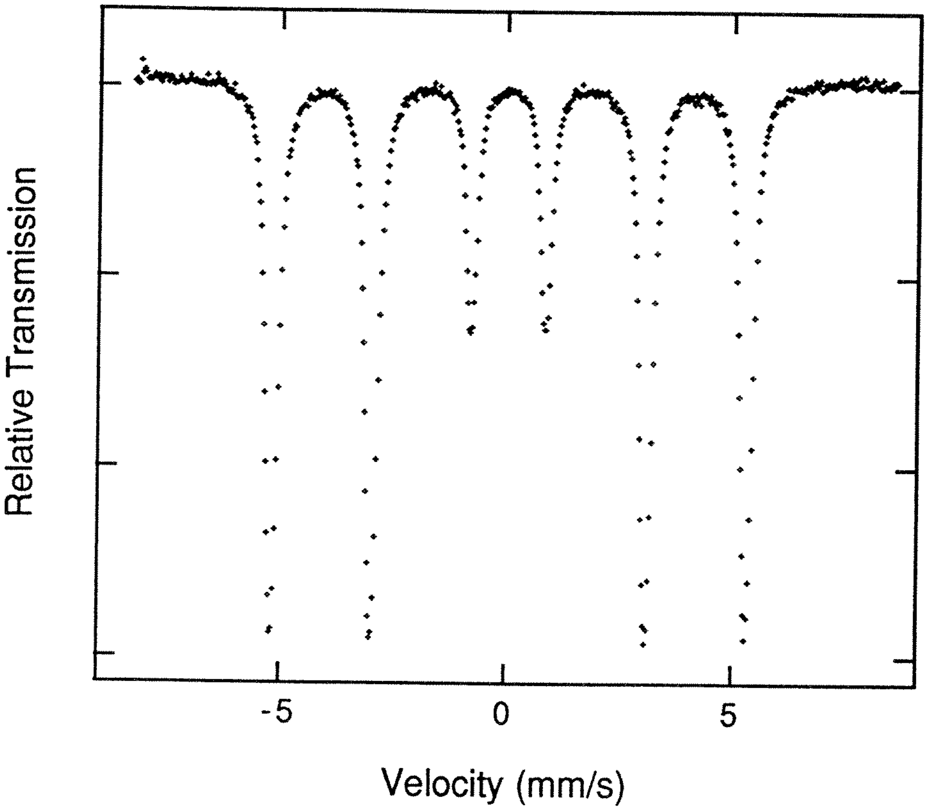

Figure 2.2 Transmission Mössbauer spectrum of α-Fe.

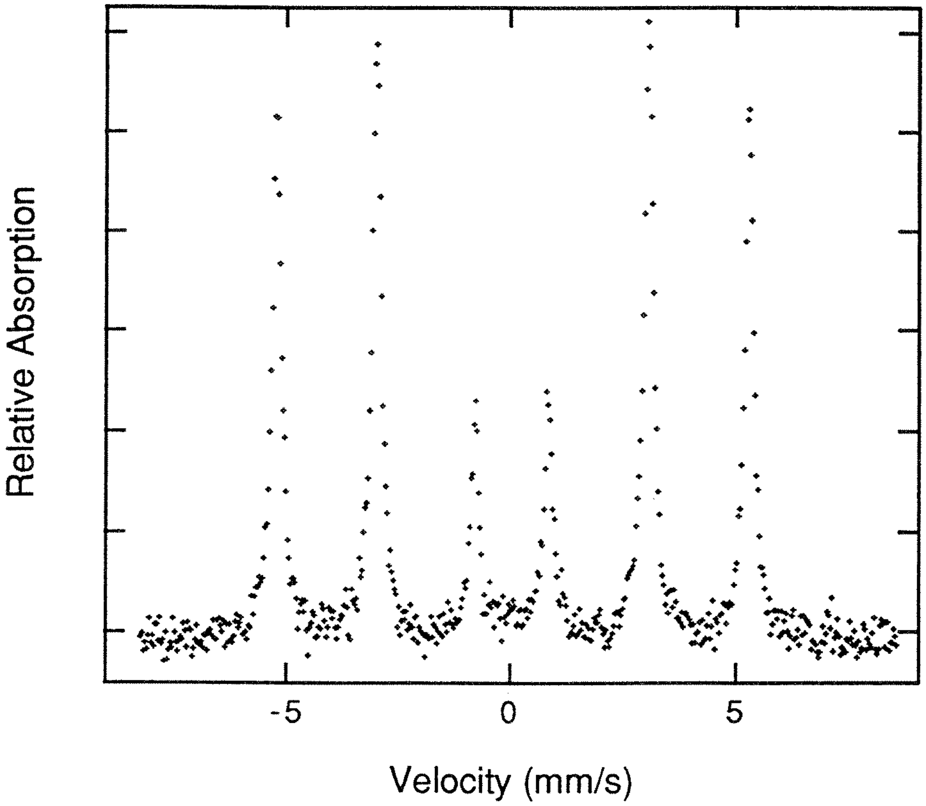

Figure 2.3 Backscatter conversion electron Mössbauer spectrum of α-Fe.

isotopes, including ^{57}Fe, the γ-ray radiation may be internally converted into a conversion electron, and subsequently an X-ray, so there are three possible radiations useful for obtaining a Mössbauer spectrum in scattering geometry: the scattered γ-rays, the conversion X-rays, and the conversion electrons.

Typical examples of both a transmission γ-ray Mössbauer spectrum from a thin iron foil and a backscatter conversion electron Mössbauer spectrum from a thin iron film are presented in Figure 2.2 and Figure 2.3, respectively.

§ 2.2 Hyperfine Interactions

The peaks of a Mössbauer spectrum are parameterized by their intensity, width, position, and splitting. The intensity and the natural lineshape have been discussed in the previous section. This section describes the more important features of the line position and splitting.

There are three major hyperfine interactions affecting the nuclear energy levels, and these correspond to the nuclear moments: the electric monopole interaction, the magnetic dipole interaction, and the electric quadrupole interaction. Figure 2.4 shows schematically the hyperfine interactions for ^{57}Fe.

Magnetic Dipole Interaction — Nuclear Zeeman Effect

The nuclear Zeeman effect is caused by the interaction of the nuclear magnetic dipole moment, μ, with the magnetic field, H, at the nucleus (hyperfine magnetic field). A nuclear state with spin I (I>0), will be split into (2I + 1) sublevels with the energy levels:

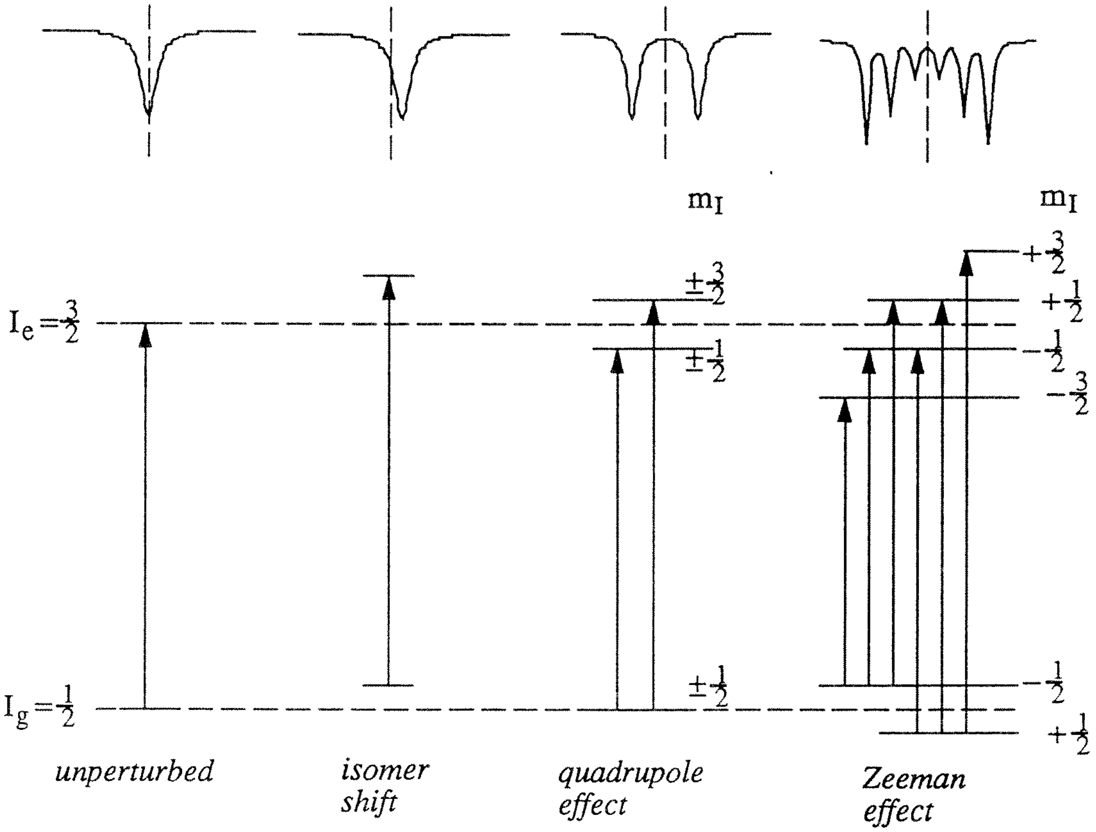

Figure 2.4 Schematic of hyperfine interactions for ^{57}Fe.

$$E_m = -\frac{\mu H m_I}{I} = -g_N \beta_N H m_I, \qquad (2.12)$$

where m_I is the magnetic quantum number with the values $m_I = I, I\text{-}1, ..., \text{-}I$. The nuclear magnetic moment is related to the nuclear Bohr magneton β_N by the nuclear Landé splitting factor g_N: $\mu = g_N \beta_N I$.

The isotope ^{57}Fe has I = 1/2 for its ground state and I = 3/2 for the 14.4 keV first excited state. A magnetic field at the site of nucleus (hyperfine magnetic field) causes a splitting of the nuclear states, as shown in Figure 2.4. The ordering of the sublevels m_I indicates the fact that the ground state magnetic moment is positive and the excited state magnetic moment is negative. The allowed transitions (with the selection rule $\Delta m = 0,\ 1$) leads to a six-line pattern. Mössbauer spectra from ferromagnetic α-Fe specimens are shown in Figures 2.2 and 2.3.

The angular dependences of the allowed transitions in the nuclear Zeeman pattern are given in Table 2.1, where θ_m is the angle between the direction of the magnetic field at the nucleus and the propagation of the γ-ray. For a polycrystalline sample free of texture and without any external magnetic field, the total radiation pattern should be isotropic. By integrating over all directions we can get the relative line intensities for the six Zeeman-split lines of a randomly oriented magnetic material, which are 3 : 2 : 1 : 1 : 2 : 3.

Electric Monopole Interaction — Isomer Shift

The isomer shift is an energy translation of a Mössbauer peak. The origin of isomer shift δ is the result of the Coulombic interaction of the nuclear charge distribution and the electron charge density at the nucleus (Kistner and Sunyar 1960, Shirley 1964). The s electrons have wavefunctions that do not vanish at the nucleus,

Table 2.1. Angular dependence of the allowed transitions in a pure Zeeman pattern of ^{57}Fe.

Transition	Δm	Angular dependence
$\pm 3/2 \rightarrow \pm 1/2$	± 1	$3/4\ (1 + \cos^2\theta_m)$
$\pm 1/2 \rightarrow \pm 1/2$	0	$\sin^2\theta_m$
$\mp 3/2 \rightarrow \pm 1/2$	∓ 1	$1/4\ (1 + \cos^2\theta_m)$

and changes in s electron densities are largely responsible for changes in the isomer shift.

The electrostatic shift of a nuclear level can be calculated with the following model (DeBenedetti, Lang and Ingalls 1961). The nucleus is assumed to be a uniformly charged sphere with radius R, and the electronic density, $e|\Psi(0)|^2$, is assumed to be uniform over nuclear dimensions. The difference between the electrostatic interaction of a hypothetical point nucleus and one of actual radius R, both having the same charge, is:

$$\delta E = \int_0^\infty e|\Psi(0)|^2 \left(V - V_{pt}\right) 4\pi r^2 dr, \tag{2.13}$$

where the electrostatic potential for the point nucleus, V_{pt}, is Ze/r, and the potential for the finite one, V, is $(Ze/R)[\frac{3}{2} - (r^2/2R^2)]$ for r R and Ze/r for r > R, thus Equation 2.13 becomes:

$$\delta E = \frac{2\pi}{5} Ze^2 |\Psi(0)|^2 R^2. \tag{2.14}$$

Equation (2.14) relates the electrostatic energy of the nucleus to its radius, which in general is different for each nuclear energy state Observations, however, are made not on the location of individual nuclear levels, but on γ-rays resulting from transitions between two such levels. The transition energies in a source and in an absorber are:

$$E_S = E_0 + \frac{2\pi}{5} Ze^2 |\Psi_S(0)|^2 \left(R_{ex}^2 - R_{gd}^2\right), \tag{2.15a}$$

$$E_A = E_0 + \frac{2\pi}{5} Ze^2 |\Psi_A(0)|^2 \left(R_{ex}^2 - R_{gd}^2\right), \tag{2.15b}$$

where, R_{ex} and R_{gd} are the nuclear radii for the excited and ground states, respectively. Using $\delta R = R_{ex} - R_{gd}$, we obtain the isomer shift, δ, as:

$$\delta = E_A - E_S = \frac{4\pi}{5} Ze^2R^2 \, \frac{\delta R}{R}\left(|\psi_A(0)|^2 - |\psi_S(0)|^2\right), \tag{2.16}$$

where $\delta R/R$ is the relative change of the nuclear radius between the excited and ground states, and the term in the parentheses is the difference between the total electron density evaluated at the nuclei of the absorber and source.

Electric Quadrupole Interaction — Quadrupole Splitting

The nonspherical charge distribution of both the excited and ground states gives the nucleus an electric quadrupole moment (eQ). The quadrupole splitting comes from the interaction of the nuclear quadrupole moment with the electric field gradient (EFG) at the nucleus. Such an interaction splits the nuclear state into sublevels with the eigenvalues

$$E_Q = \frac{eQV_{zz}}{4I(2I-1)}\left[3m_I^2 - I(I+1)\right]\left(1+\frac{\eta^2}{3}\right)^{1/2}, \tag{2.17}$$

where $V_{zz} = \ ^2V/\ z^2$, is the principal component of the diagonalized EFG tensor, and $\eta = (V_{xx} - V_{yy})/V_{zz}$, is the asymmetry parameter. (With $|V_{zz}| \rangle |V_{yy}| \rangle |V_{xx}|$ and $V_{zz} + V_{yy} + V_{xx} = 0$, $0 \quad \eta \quad 1$.) For I = 1/2 (ground state of ^{57}Fe and ^{119}Sn nuclei), $E_Q = 0$, so there is no nuclear energy level change. For I = 3/2, (first nuclear excited state for ^{57}Fe and ^{119}Sn)

$$E_Q = \pm\frac{1}{4}eQV_{zz}\left(1+\frac{\eta^2}{3}\right)^{1/2}. \tag{2.18}$$

The first excited nuclear state for ^{57}Fe and ^{119}Sn will be split into two sublevels if an electric field gradient exists at the nucleus.

It should be noted that in pure iron with cubic symmetry, no EFG is possible at a ^{57}Fe nucleus. Magnetostriction removes this cubic symmetry, but the resulting nuclear quadrupole effect is barely measurable (Spijkerman 1971, Violet and Pipkorn 1971). Even for iron atoms in a ferromagnetic alloys, such as Fe_3Al, the z-axis is determined by the direction of the hyperfine magnetic field because the interaction of I_z with this magnetic field is by far the dominant perturbation of the nuclear energy level. Although the presence of the solute atom as a nearest neighbor to an ^{57}Fe nucleus breaks the cubic symmetry, the EFG direction does not generally bear any predictable relationship to the magnetically defined z-axis. In this case only a broadening in the hyperfine magnetic field splitting of the Mössbauer absorption lines is expected.

§ 2.3 Hyperfine Magnetic Fields of ^{57}Fe in bcc Alloys

In general, the total hyperfine magnetic field (HMF) at an ^{57}Fe nucleus is the sum of the following contributions (Fultz, 1993):

$$H = H_{core} + H_{cond} + H_{ov} + H_{orb} + H_{mag} + H_{dip}, \tag{2.19}$$

where

H_{core}: Core polarization contribution, typically induced by changing the number of unpaired 3d electrons at the ^{57}Fe atom, which in turn exchange-polarize the 1s, 2s, 2p and 3s electrons;

H_{cond}: Conduction electron polarization, redistribution of charge and spin of 4s conduction electrons caused by nearest neighbor atoms;

H_{ov}: Contribution from the overlap of a nonmagnetic solute wave function with the ^{57}Fe atom, expected to scale with size differences between the solute atom and ^{57}Fe atom;

H_{orb}: Created by the spin-orbit interaction involving the nuclear spin and the unfilled 3d shell electrons;

H_{mag}: Contribution from the classical magnetic field equal to $4\pi M/3$, where M is the magnetization of lattice;

H_{dip}: Contribution from the magnetic dipole moment at each atom near the atom. In pure Fe this classical magnetic dipole contribution vanished because of the cubic symmetry, but it will change when an Fe atom is replaced with a solute atom.

While the last three terms can be understood with classical magnetics and atomic physics, they are generally less important contributions. The first three terms, which are more important contributions to the HMF of ^{57}Fe, depend on electron spin imbalances at a ^{57}Fe nucleus through the Fermi contact interaction (Fermi 1930).

Magnetic Polarization Model

Equation 2.19 shows the electronic origin of HMF perturbations, but in practice we need a simplified model which can be used to interpret the HMF obtained experimentally and extract short-range chemical information from it. The model presented here, the magnetic polarization model, was developed through work by Stearns (Stearns 1974; Stearns 1976), and Vincze and Campbell (Vincze and Campbell 1973; Vincze, Campbell and Meyer 1974) during the late 1960 s and the 1970 s. Further development was performed with Fe-Ni alloys (Fultz and Morris 1986), Fe-Co alloys (Hamdeh, Fultz and Pearson 1989; Fultz and Hamdeh 1989; Fultz 1991), and Fe-Al alloys (Fultz and Gao 1993).

The solute-induced change in the HMF at the ^{57}Fe nucleus can be obtained as the sum of two components, ΔH_L and ΔH_{NL}. ΔH_L is the change in local exchange polarization, includes the core polarization (CP) of 1s, 2s, (relativistic 2p) and 3s electrons, and the conduction electron polarization (CEP) of the 4s conduction electrons (i.e., H_{core} plus the part of H_{cond} when 4s conduction electrons are polarized by the 3d electrons at the ^{57}Fe atom itself). Changes in ΔH_L should be proportional to changes in the local magnetic moment at the ^{57}Fe atom, $\Delta\mu(0)$, which would be caused by neighboring solute atoms:

$$\Delta H_L = (\alpha_{CP} + \alpha_{CEP})\Delta\mu(0), \tag{2.20}$$

where α_{CP} and α_{CEP} are constants expressing the strengths of the core polarization and conduction electron polarization, respectively. Some solute atoms, notably transition metals to the right of Fe in the periodic table, have different bonding characteristics for the Fe 3d↑ and 3d↓ electrons. Such bonding alters the 3d spin imbalance at the ^{57}Fe atom. Some other solute atoms, like aluminum, silicon and germanium, perturb only slightly the magnetic moments at neighboring Fe atoms and contribute little to ΔH_L.

H_{NL} (nonlocal) is a transferred HMF, arising from spin polarizations of 4s electrons at ^{57}Fe nucleus caused by exchange interactions with spins at neighboring atoms. (It is the remaining part of H_{cond}. The H_{ov} term is neglected, assuming there is no big difference in atomic size.) If the neighbors of the ^{57}Fe atom have magnetic moments, $\mu(r)$, that are different from the moment of an Fe atom in pure Fe, μ_{Fe}^{0}, the change in H_{NL} with respect to that in pure Fe is:

$$\Delta H_{NL} = \alpha_{CEP} \sum_{r\neq 0} f(r)\left[\mu(r) - \mu_{Fe}^{0}\right]. \tag{2.21}$$

The constant α_{CEP} expresses the strength of the conduction electron polarization per magnetic moment at the site r, from which a fraction, $f(r)$, is carried to neighboring sites located at a distance, r, away.

When the site r is occupied by an Al (or Si and Ge) atom, we set $\mu(r) = 0$ because these solute atoms are never expected to develop a magnetic moment. Since Al (or Si and Ge) atoms affect only weakly the magnetic moments at neighboring Fe atoms (Budnick and Skalski 1967; Dean, Furley and Scurlock 1971), the host Fe atoms located near ^{57}Fe nuclei have their normal magnetic moments. We can therefore set $\mu(r) = \mu^0_{Fe}$ in Equation (2.21) when the site r is occupied by an Fe atom.

For the Fe-X (X = Al, Si, Ge) alloys we studied in this thesis research, we can obtain the total perturbation of the ^{57}Fe HMF due to a solute atom in the jth nearest neighbor shell of the ^{57}Fe atom, ΔH_j, as:

$$\Delta H_j = -\alpha_{CEP} \sum_{r \neq 0} \delta(r) f(r) \mu^0_{Fe} . \tag{2.22}$$

The delta function equals 1 when the site is occupied by an solute atom, and equals 0 when it is occupied by an Fe atom. For the set $\{\alpha_{CEP}f(1), \alpha_{CEP}f(2), \alpha_{CEP}f(3)\}$, we can use {-11.5, -3.5, +2.5} kG/mB. These parameters were obtained in calibration experiments with dilute Fe-Si alloys by Fultz and Morris (Fultz and Morris 1986). From these parameters we can obtain the total HMF perturbation at one ^{57}Fe atom at $r = 0$ for a given configuration of nearest neighbor solute atoms. Equation 2.22 works well for dilute alloys, and is still semi-quantitative for concentrated alloys. For large total HMF perturbations ($\rangle$100 kG), a nonlinearity is discernable where each solute atom causes a progressively larger HMF perturbation, and effectively stronger ΔH_1. Also, for concentrated alloys of Fe-Al (Si, Ge), it has been reported that ΔH_2 and ΔH_3 become smaller (Fultz and Gao 1993).

References

ASANO, A.: Ph.D. Thesis, Northwestern University at Evanston, Illinois, (1974).

BUDNICK, J. I. and SKALSKI, S.: in Hyperfine Interactions, A. Freeman and R. B. Frankel, eds., (Academic Press, New York 1967).

COWLEY, J. M.: Diffraction Physics, (North-Holland Publishing Company, Amsterdam-New York-Oxford, 1981) p. 27.

DEAN, R. H.; FURLEY, R. J. and SCURLOCK. R. G.: *J. Phys.*, **F 1**, 78 (1971).

DEBENEDETTI, S.; LANG, G. and INGALLS, R.: *Phys. Rev. Lett.*, **6**, 60 (1961).

DEBRUNNER, P. G. and FRANENFELDER, H.: in An Introduction to Mössbauer Spectroscopy, L. May, ed., (Plenum Press, London 1971) Chapter 1, p. 1.

FERMI, E.: *Z. Phys.*, **60**, 320 (1930).

FULTZ, B. and GAO, Z. Q.: *Nucl. Instr. and Methods, Phys. Res.*, **B 76**, 115 (1993).

FULTZ, B. and HAMDEH. H. H.: *Phil. Mag.*, **B 60**, 601 (1989).

FULTZ, B. and MORRIS, J. W. Jr.: *Phys. Rev.*, **B 34**, 4480 (1986).

FULTZ, B.: "Chemical Systematics of Iron-57 Hyperfine Magnetic Field Distributions in Iron Allors," in Mössbauer Spectroscopy Applied to Magnetism and Materials Science, G. J. Long and F. Grandjean, eds., (Plenum Press, New York, 1993) Chapter 1, p. 1.

FULTZ, B.: *Phys. Rev.*, **B 44**, 9805 (1991).

GONSER, U.: "From a Strange Effect to Mössbauer Spectroscopy," in Mössbauer Spectroscopy, U. Gonser, ed., (Springer-Verlag, New York 1975), Chapter 1, p. 1.

HAMDEH. H. H.; FULTZ, B. and PEARSON, D. H.: *Phys. Rev.*, **B 39**, 11233 (1989).

JACKSON, J. D.: *Can. J. Phys*, **33**, 575(1955).

KISTNER, D. C. and SUNYAR, A. W.: *Phys. Rev. Lett.*, **4**, 412 (1960).

MARGULIES, S. and EHRMAN, J. R.: *Nuclear Instr. and Methods*, **12**, 131 (1961).

MÖSSBAUER, R. L., Z.: *Physik*, **151**, 124 (1958).

SHIRLEY, D. A.: *Rev. Mod. Phys.*, **36**, 339(1964).

SPIJKERMAN, J. J.: *Phys. Rev. Lett.*, 26, 323 (1971).

STEARNS, M. B.: *Phys. Rev.*, **B 9**, 2311 (1974).

STEARNS, M. B.: *Phys. Rev.*, **B 13**, 1183 (1976).

VINCZE, I. and CAMPBELL, I. A.: *J. Phys.*, **F3**, 647 (1973).

VINCZE, I., CAMPBELL, I. A. and MEYER, A. J.: *J. Solid State Commun.*, **15**, 1495 (1974).

VIOLET, C. E. and PIPKORN, D. N.: *J. Appl. Phys.*, **42**, 4339 (1971).

WERTHEIM, G. K.: Mössbauer Effect: Principles and Applications, (Academic Press, New York 1964).

Chapter 3 Experimental Procedures

In this chapter I will describe the instruments and experimental techniques that were used to synthesize and characterize the materials studied in my thesis research.

§3.1 Sample Preparation

To study the kinetics of disorder to order transformations, especially the early stages of ordering kinetics, it is essential to prepare initial samples with little or no long range ordering. Several methods were used to get disordered Fe_3Al, Fe_3Si and Fe_3Ge samples.

Whether a particular rapid cooling method can be used to prepare disordered samples depends on the cooling rate of the method. How high the cooling rate needs to be to get an alloy disordered can be estimated roughly from the distance an atom in the alloy diffuses during the cooling process. The temperature during a quenching process can be assumed as a linear function of time:

$$T = T_0 - \kappa t, \tag{3.1}$$

where κ is the cooling rate for the process, and T_0 is the initial temperature. The distance an atom diffuses before the temperature reaches room temperature, T_r, (for quenching done at room temperature) is:

$$\ell = \sqrt{\int_0^{t_r} D(T)\,dt}\,, \tag{3.2}$$

where the diffusion coefficient $D(T) = A \exp(-Q/kT) = A \exp[-Q/k(T_0 - \kappa t)]$, and $t_r = (T_0 - T_r)/\kappa$. A is the frequency factor and Q is the activation energy. Substitute $t' = k(T_0 - \kappa t)/Q$, we can re-write Equation 3.2 and get the critical cooling rate as:

$$\kappa = \frac{AQ}{k\ell^2} \int_{\frac{kT_r}{Q}}^{\frac{kT_0}{Q}} \exp\left(-\frac{1}{t'}\right) dt' . \tag{3.3}$$

For Fe_3Al, $A = 1.74 \times 10^2$ cm²/s, and Q = 211.4 kJ/mol [for temperature the range 823 °K to 903 °K (Vasilev, Kamardin, Skatskii, Chermomorchenko and Schuppe 1955)]. Using the first nearest neighbor distance in Fe_3Al as ℓ ($\approx 2 \times 10^{-8}$ cm), and the critical temperature of ordering for T_0 ($\approx$1073 K), we get the cooling rate $\kappa \approx 5 \times 10^6$ K/s.

The piston-anvil quenching method proved to be the best way to prepare disordered samples of Fe_3Al, but its cooling rate was not fast enough to disorder Fe_3Si. Disordered Fe_3Si and Fe_3Ge samples were prepared by mechanical alloying. Table 3.1 summarizes the results from different sample preparation methods for different alloys.

Piston-Anvil Quenching Method:

To get a quenched foil sample, an ingot was first prepared from materials of 99.99% purity by arc-melting on a water cooled copper hearth under an argon atmosphere in an Edmund Bühler D-7400 arc-melting apparatus. The resulting ingots were inverted and remelted several times to insure homogeneity. The mass losses upon melting were negligible, and the composition was checked by electron microprobe analysis, atomic absorption spectrometry and energy dispersive x-ray spectrometry with a transmission electron microscope (TEM).

Table 3.1: Methods for sample preparation

Method	Fe_3Al	Fe_3Si	Fe_3Ge
piston-anvil quench	disordered	ordered	
ball milling	disordered*	disordered	disordered
sputtering	disordered	amorphous	disordered**

* The Fe_3Al ingot needed to be filed to powder format before ball milling. The as-filed powder was already disordered, and had an average grain size of 10 nm.

** Hamdeh, Kramer, Fultz, Gao and Oliver 1993.

Chemically disordered samples were obtained by piston-anvil quenching with an Edmund Bühler Ultra Rapid Quencher, shown schematically in Figure 3.1. A 2.2 MHz radio frequency (RF) power supply is connected to a conically shaped copper coil. This apparatus is operated by levitating and melting a small piece of an ingot (approximately 100 mg for Fe_3Al) under a purified argon atmosphere. As the RF current to the coil is removed, the molten droplet falls and triggers a detector which causes two polished copper pistons to accelerate toward each other. The colliding pistons impact the droplet as it falls, and the droplet is quenched rapidly into a foil of about 50 μm in thickness. Depending on the thermal conductivity and the thickness of the sample, quenching rates of 10^6 K/sec can be reached.

Ball Milling Method:

Ball milling of materials has been an important technique in the ceramics processing and powder metallurgy industries. While the objectives of normal milling include particle size reduction and mixing, high energy milling can also accomplish solid state alloying, i.e., mechanical alloying. This technique was first developed by J. S. Benjamin and his colleagues at the International Nickel Company to produce oxide dispersion strengthened alloys (Benjamin 1970 and 1976). During the past few years this technique was also used as a way to synthesize non-equilibrium materials like amorphous materials (Yermakov, Yurichikov and Barinov 1981; Koch, Cavin, McKamey and Scarbrough 1983) and nanocrystalline materials (Shingu, Huang, Niskitani and Nasu 1988; Fultz, Le Caër and Matteazzi 1989; Eckert, Holzer, Krill and Johnson 1992; Koch 1993).

There are several different types of hardware used for ball milling. In this thesis research we used a SPEX 8000 laboratory mill/mixer, shown schematically in

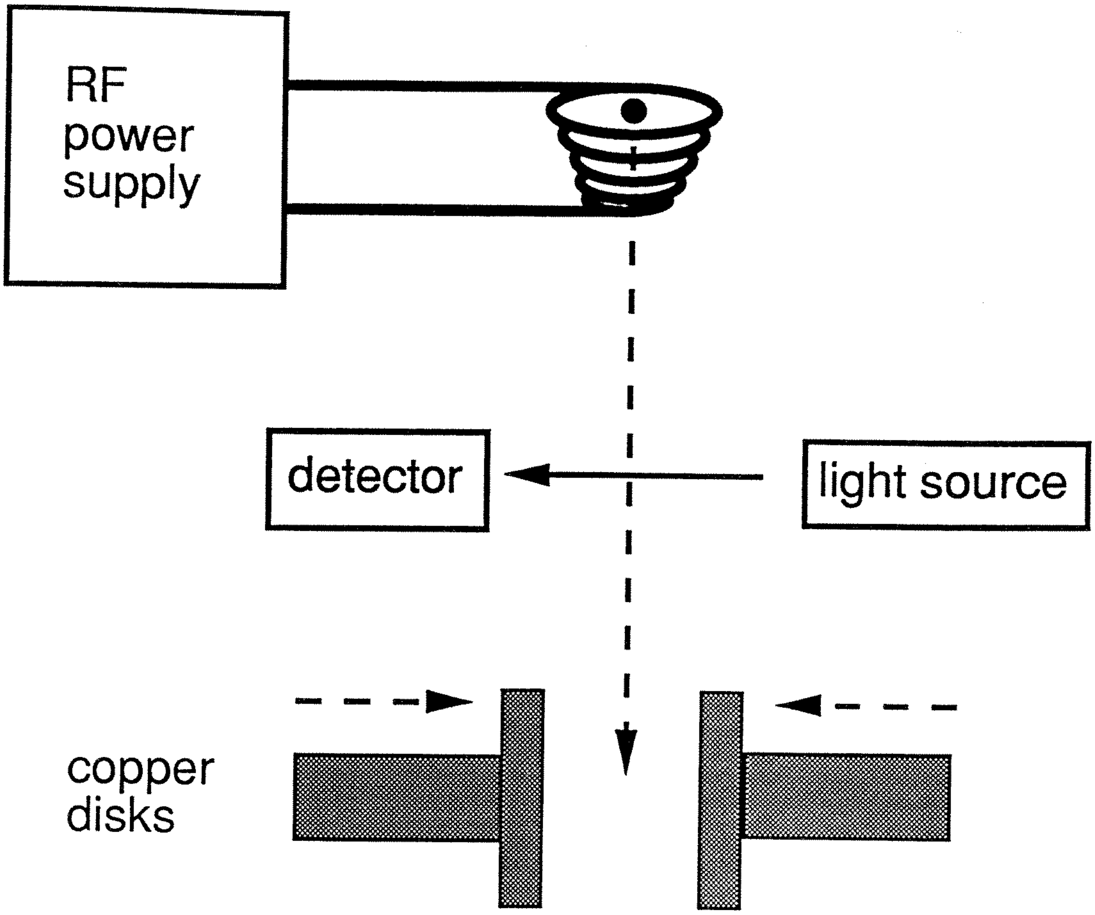

Figure 3.1 Schematic illustration for piston-anvil quenching apparatus. (After James Okamoto, 1993)

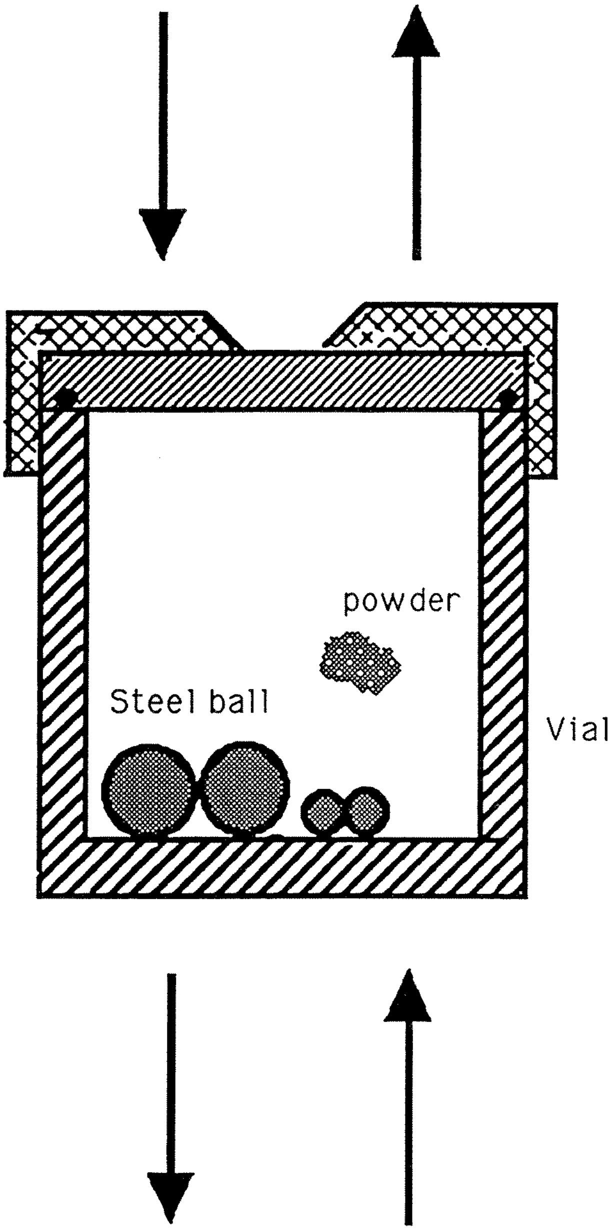

Figure 3.2 Schematic illustration for Ball-Milling process.

Figure 3.2. This kind of ball milling equipment is usually classified as a vibratory mill, and it provides very high milling intensity with ball velocities of 3 - 4 m/s.

The elemental powders of corresponding composition were first mixed, and then sealed under an argon atmosphere. Two different vial-ball pairs were used: tungsten carbide and hardened steel. The usual ball-to-powder weight ratio was 4:1. Disordered alloys were prepared by ball milling at room temperature. To induce chemical order, the as-milled powders were annealed at several temperatures for various times in evacuated quartz ampoules.

§3.2 X-ray Diffraction and Data Processing

Experimental Procedure for X-ray Diffraction Measurements

Two X-ray diffractometers were used in this thesis research. Some early X-ray diffractometry work was performed with a GE θ-2θ diffractometer using Cr Kα radiation. Most later X-ray diffractometry work was performed with an INEL CPS-120 diffractometer system using monochromatized Co Kα radiation and a curved position sensitive detector (PSD) spanning 127° in 2θ angle. With a PSD and a stationary sample (fixed glancing angle), the absorption corrections for our flat samples differ from those for a Bragg-Brentano diffractometer. We multiplied the integrated intensities of the peaks by a correction factor of $(\sin\phi+\sin(2\theta-\phi))/\sin(2\theta-\phi)$ so we could compare these intensities with intensities calculated for conventional θ–2θ x-ray diffractometry measurements. (This correction is described in Appendix A.) Here ϕ is the glancing angle of incidence for the x-ray beam on the flat sample, typically 15 degrees.

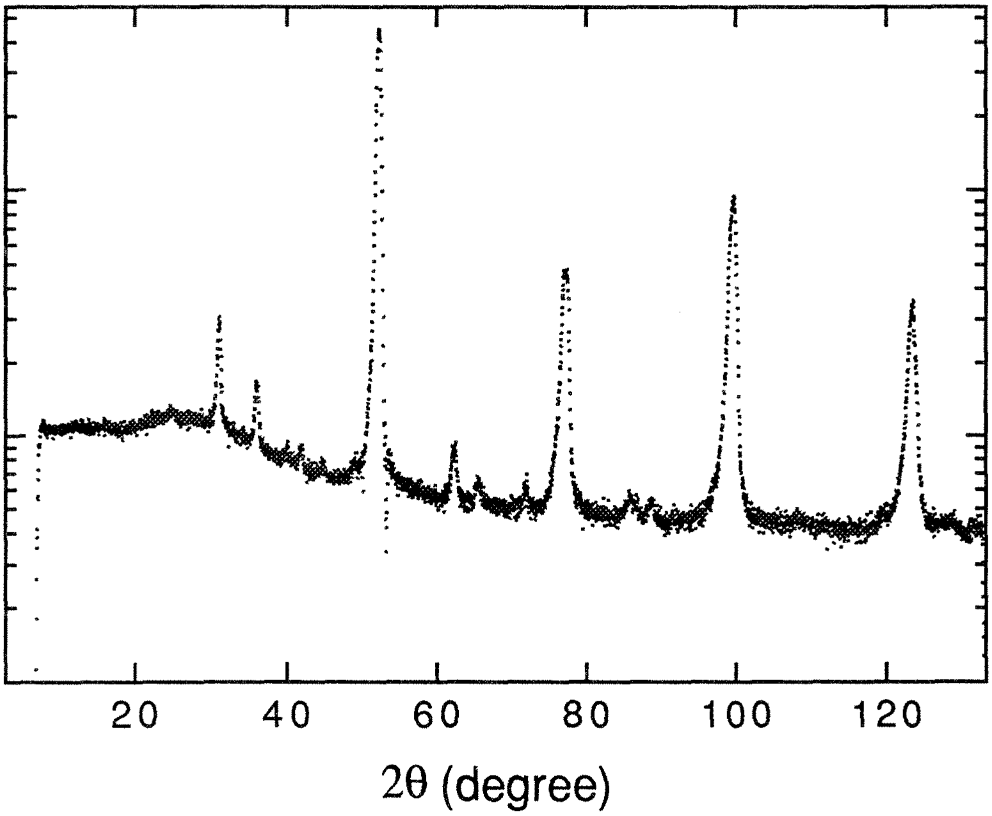

Figure 3.3 X-ray diffraction pattern from an ordered Fe_3Al sample.

An X-ray diffraction pattern from a well-ordered alloy of Fe_3Al is presented in Figure 3.3.

Determining Long Range Order From X-ray Data

The long range order (LRO) parameter, L, can be obtained from the experimentally measured intensity of the $\left(\frac{1}{2}\frac{1}{2}\frac{1}{2}\right)$ and (100) x-ray superlattice diffraction, $I^{Ex}_{\left(\frac{1}{2}\frac{1}{2}\frac{1}{2}\right)}$ and $I^{Ex}_{(100)}$. A long range order parameter can be written as:

$$L_{\left(\frac{1}{2}\frac{1}{2}\frac{1}{2}\right)} = \sqrt{\left(I^{Ex}_{\left(\frac{1}{2}\frac{1}{2}\frac{1}{2}\right)} \Big/ I^{Ex}_{(110)} \right) \Big/ \left(I^{Cal}_{\left(\frac{1}{2}\frac{1}{2}\frac{1}{2}\right)} \Big/ I^{Cal}_{(110)} \right)}, \tag{3.4a}$$

or

$$L_{(100)} = \sqrt{\left(I^{Ex}_{(100)} \Big/ I^{Ex}_{(110)} \right) \Big/ \left(I^{Cal}_{(100)} \Big/ I^{Cal}_{(110)} \right)}, \tag{3.4b}$$

where I^{Cal}'s are calculated diffraction intensities, and the (110) diffraction is a fundamental bcc diffraction which is independent of the ordered structure.

Table 3.2 gives the theoretical intensities of the $(\frac{1}{2}\,\frac{1}{2}\,\frac{1}{2})$ and (100) superlattice peaks relative to the (110) fundamental peak for various completely ordered structures of Fe_3Al, Fe_3Si and Fe_3Ge at 300 K, using Co Kα radiation with a wavelength $\lambda = 1.79$Å. These data were obtained by calculating x-ray powder diffraction intensities (Rotella 1983). They include the Lorentz-polarization factor (for a Bragg-Brentano diffractometer) and multiplicities. Note that if the alloy has only B2 order, the $(\frac{1}{2}\,\frac{1}{2}\,\frac{1}{2})$ superlattice peak is absent. For only B32 order, the (100)

Table 3.2: Calculated Relative Intensities of Superlattice Diffractions

Alloy	Ordering Structure	$I^{Cal}_{\left(\frac{1}{2}\frac{1}{2}\frac{1}{2}\right)} / I^{Cal}_{(110)}$	$I^{Cal}_{(100)} / I^{Cal}_{(110)}$
	B2	0	3.56
Fe_3Al	B32	3.50	0
	$D0_3$	7.00	3.56
	B2	0	3.21
Fe_3Si	B32	3.13	0
	$D0_3$	6.23	3.21
	B2	0	0.56
Fe_3Ge	B32	0.53	0
	$D0_3$	1.06	0.56

superlattice diffraction is absent.

Determining Sizes of Grains and Domains, and Magnitudes of Strain from X-ray Data

The finite widths of the Bragg peaks in X-ray diffraction patterns are caused by, besides the instrumental broadening, the grain or domain size and the atomic level strain (Warren 1969). Because of the small sizes of ordered domains in the early stages of ordering, which was our primary region of interest, the broadening of the superlattice diffraction peaks is dominated by effects of small domain sizes. By ignoring the strain effect, the ordered domain size can be estimated from the breadths of X-ray superlattice diffraction peaks with the Scherrer formula:

$$t \cong \frac{K\lambda}{B\cos\theta_B} \quad , \tag{3.5}$$

where t is the domain size and λ is the wavelength of X-ray. B is the full-width-at-half-maximum of the superlattice diffraction peaks at angle $2\theta_B$. K is a constant, typically 0.9 or so.

To determine both the grain size and the internal strain distribution simultaneously, we measured the k-dependence of the integral breadths of X-ray diffraction peaks (Klug and Alexander 1974). When both size and strain broadening are present, it is necessary to make an assumption as to the shapes of the two contributing line profiles. In this work they are presumed to be both Lorenzian functions (Cauchy). Thus we have the overall broadening effect as:

$$\Delta k = \Delta k^S + \Delta k^D, \tag{3.6}$$

where the size effect Δk^{S} can be obtained by rewriting the Scherrer formula in k space:

$$\Delta k^{S} = \frac{K}{L}, \tag{3.7}$$

here L is the grain size. The strain broadening in Equation 3.6 is (Wilson 1949):

$$\Delta k^{D} = 4e\frac{\sin\theta}{\lambda} = 2ek, \tag{3.8}$$

and thus:

$$\Delta k = \frac{1}{L} + 2ek, \tag{3.9}$$

wherein K of Equation 3.5 has been set equal to unity. By plotting Δk against k we can estimate from the ordinate intercept the mean crystallite dimension L, and from the slope the full range of lattice strain, e.

§3.3. Mössbauer Spectrometry Measurements

Experimental Procedure for Mössbauer Spectrometry Measurements

Mössbauer spectra were obtained, for our powder and foil samples, in transmission geometry with a constant acceleration spectrometer. A radiation source of between 10 and 30 mCi ^{57}Co in a Rh matrix was used, and transmission γ-ray spectra were obtained with an Ar-CH_4 flow-gas detector. Both the specimen and the source were at room temperature. For thin film samples, Mössbauer spectra were also obtained by using a conversion electron detector. This detector used He-CH_4 flow-gas.

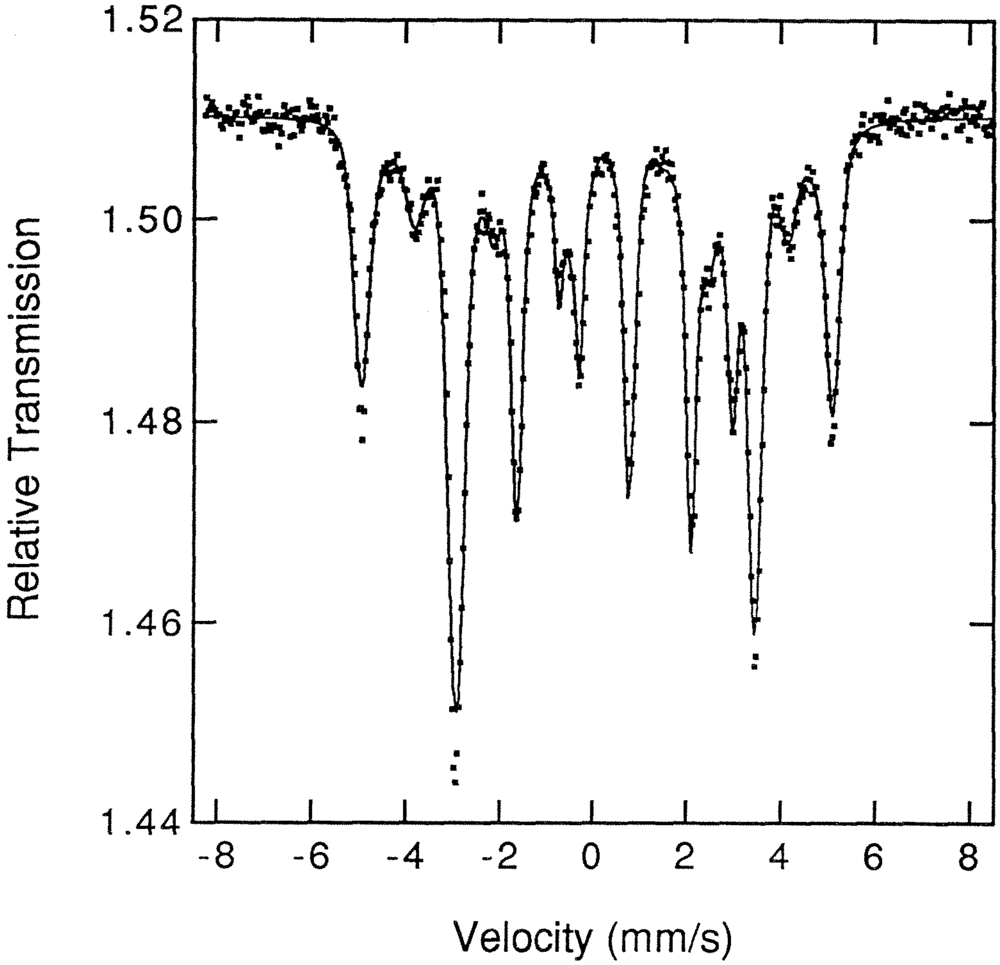

Figure 3.4 Transmission Mössbauer spectrum from a well-ordered Fe_3Si sample. The dotted one is the experimental spectrum, and the fitted spectrum is shown as a solid line.

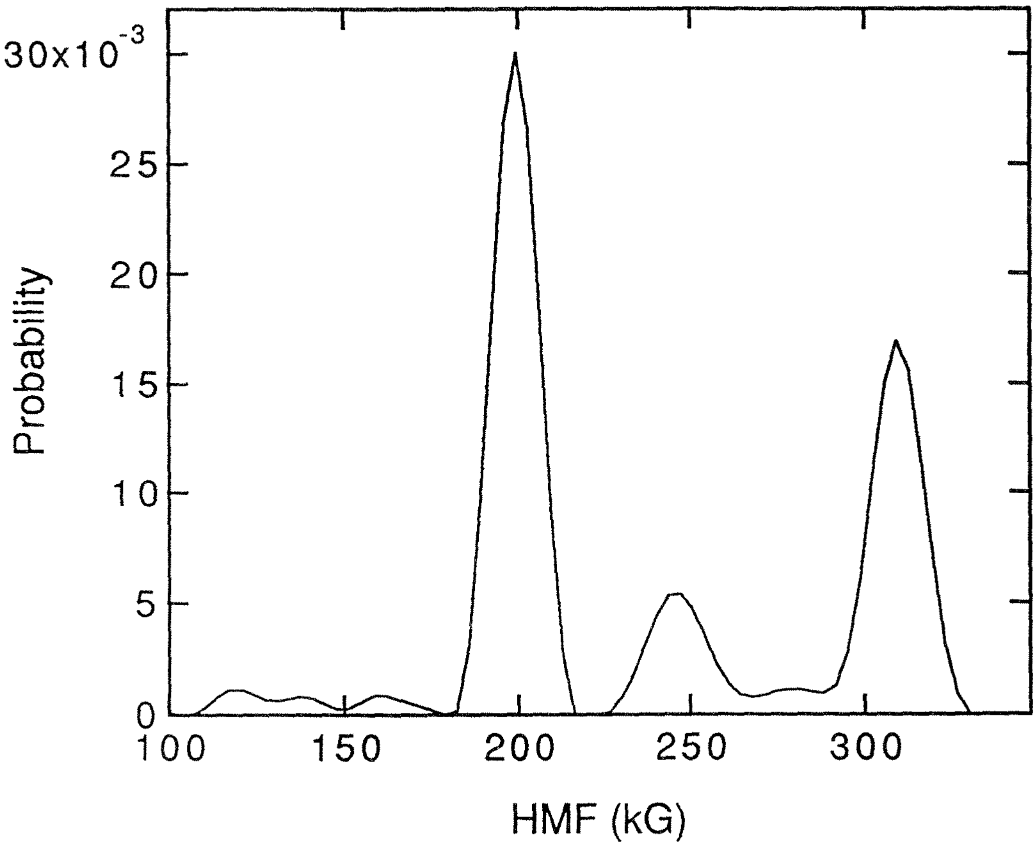

Figure 3.5 Hyperfine magnetic field distribution extracted from the spectrum shown in Figure 3.4, using the method of Le Caër and Dubois.

Determining the Short Range Order Parameter From Mössbauer Spectrum

As an example, a transmission Mössbauer spectrum from a well-ordered sample of Fe_3Si is shown in Figure 3.4. The raw Mössbauer spectrum comprises of a sum of overlapping ferromagnetic sextets, and the distribution of ^{57}Fe hyperfine magnetic fields (HMFs) can be obtained by processing these spectra using the method of Le Caër and Dubois (Le Caër and Dubois 1979). In this method, a set of sextets with progressive HMF of preset range were used to fit the experimental data. A linear dependence of the isomer shift, IS, on the HMF is assumed: IS = A * HMF + B. The constants A and B were determined by the quality of fit of a simulated spectrum to the experimental one. The hyperfine magnetic field (HMF) distribution obtained from the spectrum of Figure 3.4 is presented in Figure 3.5. In Figure 3.4, a fitted spectrum using the HMF distribution of Figure 3.5 is also presented as a solid line.

Hyperfine magnetic field (HMF) distributions from both disordered and ordered samples of Fe_3Si are presented in Figure 3.6. The most prominent features are the two peaks that grow at 190 and 310 kG. X-ray diffractometry showed that the ordered sample has a well developed $D0_3$ ordered structure, so these two peaks correspond to the two chemical sites for Fe in the $D0_3$ ordered structure. The peak at 310 kG is from iron atoms with zero (0) Si atoms in its first-nearest neighbor (1nn) shell, and the peak at 190 kG is from iron atoms with four (4) 1nn Si atoms. The other peaks in the HMF distribution can be understood approximately with a simple model in which the HMF at a particular ^{57}Fe atom is reduced in proportion to the number of Si atoms in its 1nn shell (Stearns 1963 and 1972; Fultz 1993). [As observed for Fe_3Al (Fultz and Gao 1993), in ordered Fe_3Si the 2nn and 3nn Si atoms cause ^{57}Fe HMF perturbations that are nearly negligible compared to the effects of 1nn Si atoms.] The peaks in Figure 3.6 are labeled by the number of 1nn Si atoms

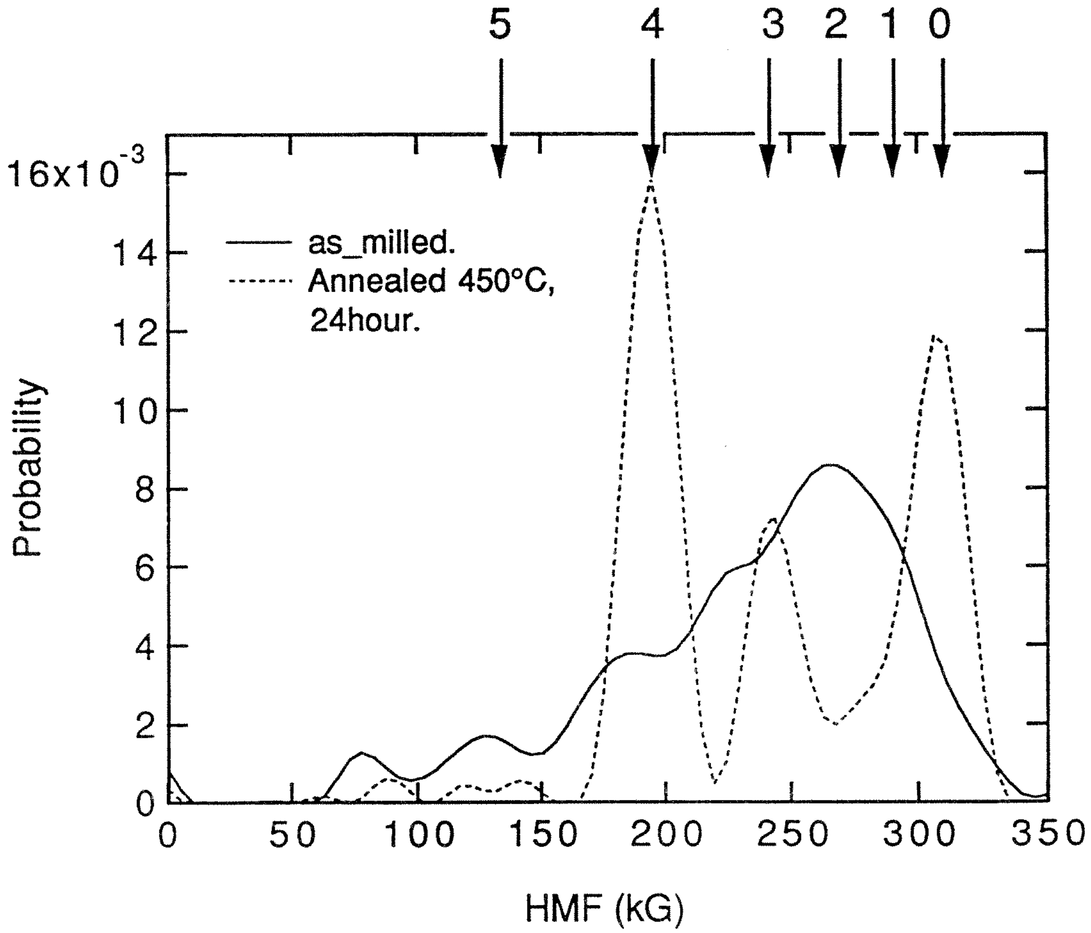

Figure 3.6 Hyperfine magnetic field distributions for Fe_3Si alloys as ball-milled and after annealed at 450 °C for 24 hours.

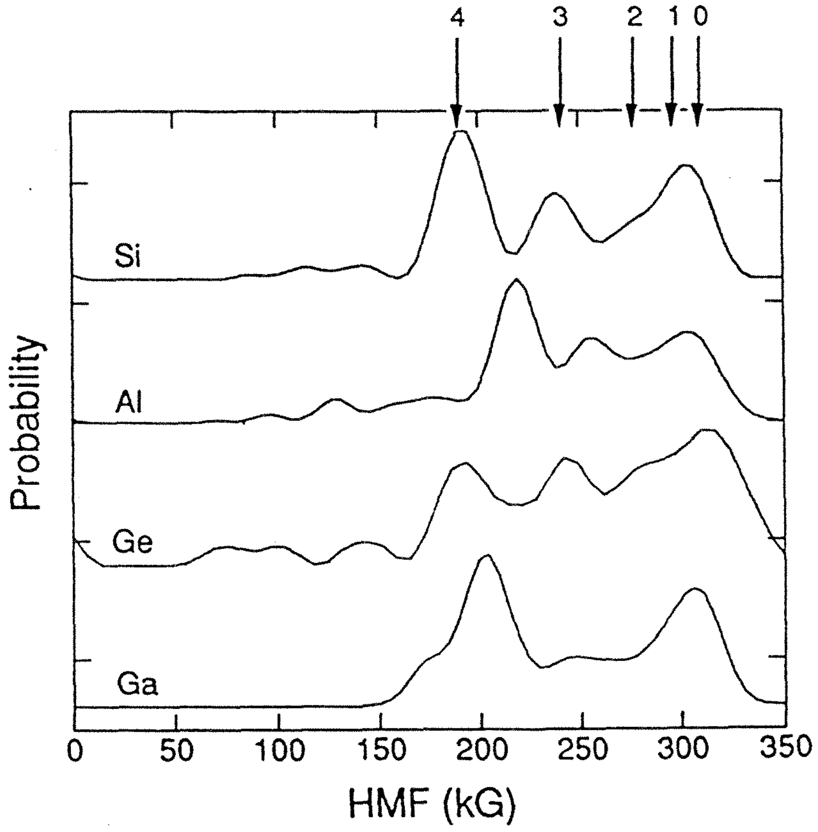

Figure 3.7 HMF distributions for Fe 25 at.% Al, Fe 24 at.% Si, Fe 25 at.% Ga and Fe 22 at.% Ge with approximately the same state of chemical short-range order.

around the ^{57}Fe atom. The areas of these peaks correspond approximately to the probability of each 1nn environment. Gaussian functions were fit independently to these peaks to obtain the fractional populations, P(n), of ^{57}Fe atoms having n Si 1nn atoms. HMF distributions for Fe_3Al and Fe_3Ge show similar features with slightly different peak positions. Typical HMF distributions for partially ordered Fe-Al, Fe-Si, Fe-Ge and Fe-Ga alloys are presented in Figure 3.7 (Fultz, Gao, Hamdeh and Oliver 1994). These HMF distributions show clear similarities.

In general, a short range order parameter, p(4), was obtained from the experimentally measured fractional population of ^{57}Fe atoms with (4) solute 1nn atoms, $P^{ex}(4)$:

$$p(4) = \frac{P^{ex}(4) - P^{dis}(4)}{P^{D03}(4) - P^{dis}(4)}, \tag{3.10}$$

here $P^{dis}(4) = 0.0865$ is the binomial probability for finding an ^{57}Fe atom with 4 solute neighbors in a random solid solution of 25 at.% solute, and $P^{D03}(4) = \frac{2}{3}$ is the fraction of ^{57}Fe atoms with 4 solute neighbors in the ordered alloy (from Figure 1.3 of Chapter 1). A similar procedure was used to obtain p(0) for the fractional population of ^{57}Fe atoms with (0) solute 1nn atoms. These are not the same as the traditional Warren-Cowley SRO parameters from X-ray diffraction, but p(0) and p(4) are legitimate SRO parameters in their own right. They denote the probabilities of ^{57}Fe atoms having (0) or (4) 1nn solute atoms.

Using Mössbauer Data to Estimate Chemical Composition

For binary Fe_3X alloys, the populations of the ^{57}Fe sites in the fully $D0_3$ ordered structure can be used to determine the actual composition. When the alloy is off-stoichiometric, there is a substantial modification of these fractional populations.

For example, in a sub-stoichiometric Fe_3X alloy, the ^{57}Fe atoms that would have had (4) solute atom neighbors now have some of those solute atoms replaced with Fe atoms. Assume these extra Fe atoms are distributed randomly over the solute sites. There is the probability, δc, for finding an Fe atom on any solute site:

$$\delta c = 1-4c. \tag{3.11}$$

Because the solute atoms occupy one of the four sublattices in $D0_3$ ordered structure (as discussed in Section §1.3), a small composition decrease for solute atoms will be concentrated into a composition change on one sublattice, which makes it seem four times larger, as shown in Equation 3.11. These extra Fe atoms do not change the environments of the ^{57}Fe atoms on the minority sites of the $D0_3$ ordered structure, which have (0) 1nn solute neighbors, since the 1nn shell of such a site is already fully occupied by Fe atoms. For those ^{57}Fe atoms on the majority sites, a random substitution of Fe atoms into their (4) 1nn solute neighbor sites gives a ratio for the number of ^{57}Fe environments with (4) and (3) solute neighbors (as calculated similarly in Section §1.3):

$$\frac{P_4}{P_3}=\frac{\frac{4!}{4!0!}\delta c^0(1-\delta c)^4}{\frac{4!}{3!1!}\delta c^1(1-\delta c)^3}=\frac{1-\delta c}{4\delta c}. \tag{3.12}$$

Similarly, for the super-stoichiometric Fe_3X alloy:

$$\delta c = 4c - 1. \tag{3.13}$$

There are two sites for Fe atoms in the $D0_3$ structure (as seen in Section §1.3). We do not believe that the extra solute atoms will replace Fe atoms in both sites, but rather we expect the solutes to replace Fe atoms in the minority site only, since these sites are in fact occupied by solute atoms in the B2 structure at higher temperature for

Fe_3Al. These sites are 1nn to the majority Fe sites, not the minority Fe sites. For those ^{57}Fe atoms on the majority sites a random substitution of solute atoms into their (4) 1nn Fe neighbor sites gives a ratio for the number of ^{57}Fe environments with (4) and (5) solute neighbors:

$$\frac{P_4}{P_5}=\frac{\frac{4!}{4!0!}\delta c^0(1-\delta c)^4}{\frac{4!}{3!1!}\delta c^1(1-\delta c)^3}=\frac{1-\delta c}{4\delta c}. \tag{3.14}$$

Equations 3.12 and 3.14 are particularly sensitive measures of δc, and hence the composition of the alloy. Because of approximations used to derive them, Equations 3.12 and 3.14 are valid only if δc is small.

Using this method, we can estimate the chemical composition for the sample in Figure 3.6 be about Fe-23.8 at.% Si. Since this is a sample prepared by ball milling, it is not surprising that there is some iron contamination from the steel vial and ball that causes an increase in the Fe composition.

§3.4 Transmission Electron Microscopy

A Philips EM430 TEM operated at 300 kV was used for the TEM studies. The Fe_3Al specimens for TEM examination were punched from the as-quenched foils, and thinned to electron transparency using a Fishione twin-jet electropolisher. In this electropolisher, the specimen is mounted between two jets of electrolyte and a voltage is applied across the electropolishing cell. To cool the electropolishing solution below room temperature, the apparatus is immersed in a bath of methanol cooled by liquid nitrogen. A light source and a photo-detector are used to stop polishing at the moment of perforation (Schoone and Fishione, 1966). For Fe_3Al, the electrolytic solution used was 20% perchloric acid, 80% methanol, and the polishing was performed at a temperature of -30 °C.

The thin foil TEM samples were annealed in-situ with a heating holder. To identify the morphologies of ordered domains, dark field images were obtained from the (100) and $(\frac{1}{2}\frac{1}{2}\frac{1}{2})$ superlattice diffractions in a <110> zone axis orientation. To maximize the intensities of dark field images from superlattice diffractions, and to set the diffraction condition at zero diffraction error ($\mathbf{s} \equiv \Delta\mathbf{k} - \mathbf{g} = 0$), we sought to image bend contours from the dark field diffractions. Even though the (100) and $(\bar{1}00)$ bend contours were invisible on the viewing screen, we knew they would be situated between the (200) and $(\bar{2}00)$ bend contours, which were prominent. Bend contours from (222)-type fundamental diffractions were used in the same way to locate the $(\frac{1}{2}\frac{1}{2}\frac{1}{2})$ bend contours. The dark field images presented in Chapter 4 were obtained with this technique.

Diffraction Image Contrast Simulations

In the early stages of ordering, the ordered domains are small, even compared to the thicknesses of the thin foils used in TEM. Our dark field images from superlattice diffractions therefore contain intensities from several overlapping domains, so image interpretation is not straightforward. We calculated the diffraction contrast in these images by computer simulation. (The source code for this calculation is included in Appendix B.) The simulated crystals contained 40×40×40 cells. Within this crystal, we nucleated the four variants of $D0_3$ domains at 300 random locations, and allowed them to grow to impingement. On the average, there were 7 overlapping domains in each column and the average diameter of the domains was about 6 times the lattice parameter. (We tried smaller simulated crystals, and their diffraction contrast was qualitatively similar.)

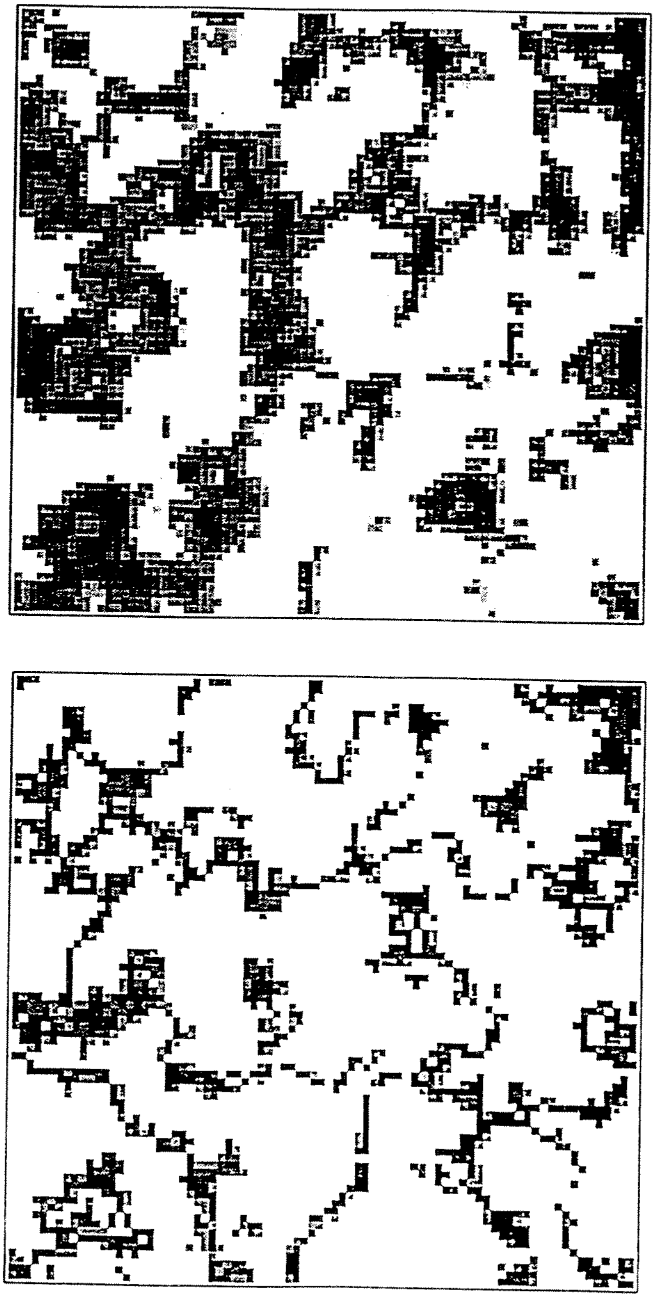

Figure 3.8 Simulated dark field image for $(\frac{1}{2}\,\frac{1}{2}\,\frac{1}{2})$ superlative diffraction (upper), and (100) superlative diffraction (lower).

Kinematical theory is unreliable for calculating the intensities of fundamental diffractions from foil specimens of several hundred Angstrom thicknesses. Nevertheless, kinematical theory is applicable for calculating diffraction contrast in dark field images of superlattice diffractions because of their long extinction distances (Marcinkowski and Brown 1962). With our simulated crystals, we summed the phases, $\exp(i\Delta\mathbf{k}\cdot\mathbf{r})$, of the diffracted wavelets from each unit length in each vertical column of the crystal. For the (100) diffraction, $\Delta\mathbf{k} = \frac{2\pi}{a}(100)$, and the phases of the four variants of the $D0_3$ structure differ by π or zero. For the $(\frac{1}{2}\frac{1}{2}\frac{1}{2})$ diffraction, $\Delta\mathbf{k} = \frac{2\pi}{a}(\frac{1}{2}\frac{1}{2}\frac{1}{2})$, and the phases of the four variants of the $D0_3$ structure differ by 0, $\pi/2$, π, or $3\pi/2$. With zero diffraction error ($\mathbf{s} \equiv \Delta\mathbf{k} - \mathbf{g} = 0$), each unit length of domain contributes +1 or −1 to the amplitude of the (100) diffraction, and +1, i, −1, or −i to the amplitude of the $(\frac{1}{2}\frac{1}{2}\frac{1}{2})$ diffraction. The intensity of the diffraction contrast from each vertical column was taken as the square of this sum. The simulated dark field image was obtained as the diffraction intensity from every column of the crystal, and was plotted as a two-dimensional gray scale image. Simulated dark field images for $(\frac{1}{2}\frac{1}{2}\frac{1}{2})$ and (100) diffractions are shown in Figure 3.8, and these images are similar to the experimental TEM images reported in Chapter 4. By comparing the morphological features in the diffraction contrast to the domain sizes in the computer-simulated alloy, we find that the diffraction contrast can be used as a good estimate of the domain size. We also note that in simulated images, the (100) dark field image has stronger diffraction contrast, and relatively sharper boundaries, than does the $(\frac{1}{2}\frac{1}{2}\frac{1}{2})$ image.

§ 3.5 Chemical Analysis

Several methods were used to measure the chemical compositions of my samples. The most frequently used method was energy-dispersive X-ray spectrometry (EDX). The energy-dispersive X-ray spectrometry was performed with an EDAX 9900 spectrometer mounted on the Philips EM430 TEM. One advantage of using EDX to do microchemical analysis is that both average composition from a relatively large area and detailed composition from very localized areas can be obtained from the same sample. In this way we can obtain the overall chemical composition of a sample, as well as its uniformity.

An EDX spectrum from a ball milled $(Fe_3Si)_{0.95}Nb_{0.05}$ alloy is presented in Figure 3.9. Because this sample was prepared with a tungsten-carbide vial and balls, the as-milled powder contains tungsten carbide particles from the vial and ball. X-ray diffraction showed strong tungsten carbide peaks. What concerned us, however, was if tungsten or carbon atoms diffused into the $(Fe_3Si)_{0.95}Nb0.05$ alloy. Because of the large heat of formation of tungsten carbide, we expect it will stay in isolated form. This was confirmed by EDX analysis. The spectrum shown in Figure 3.9 was obtained with a focused electron beam on one isolated $(Fe_3Si)_{0.95}Nb0.05$ particle. From this spectrum we found not only that the alloy had the right chemical composition, but also that there is no tungsten (or tungsten carbide) diffused into the particle, since no tungsten peak is observed in the EDX spectrum. (The Cu peak is from Cu in the sample holder.)

Chemical analysis was also performed with a JEOL Superprobe 733 electron microprobe operating at 15 kV with typically a 15x15 μm beam area and calibrated with elemental standards. Atomic absorption spectrometry was also performed outside Caltech by an independent testing laboratory. Finally, small composition errors were also measured from the hyperfine magnetic field distribution using the method described in Section 3.3.

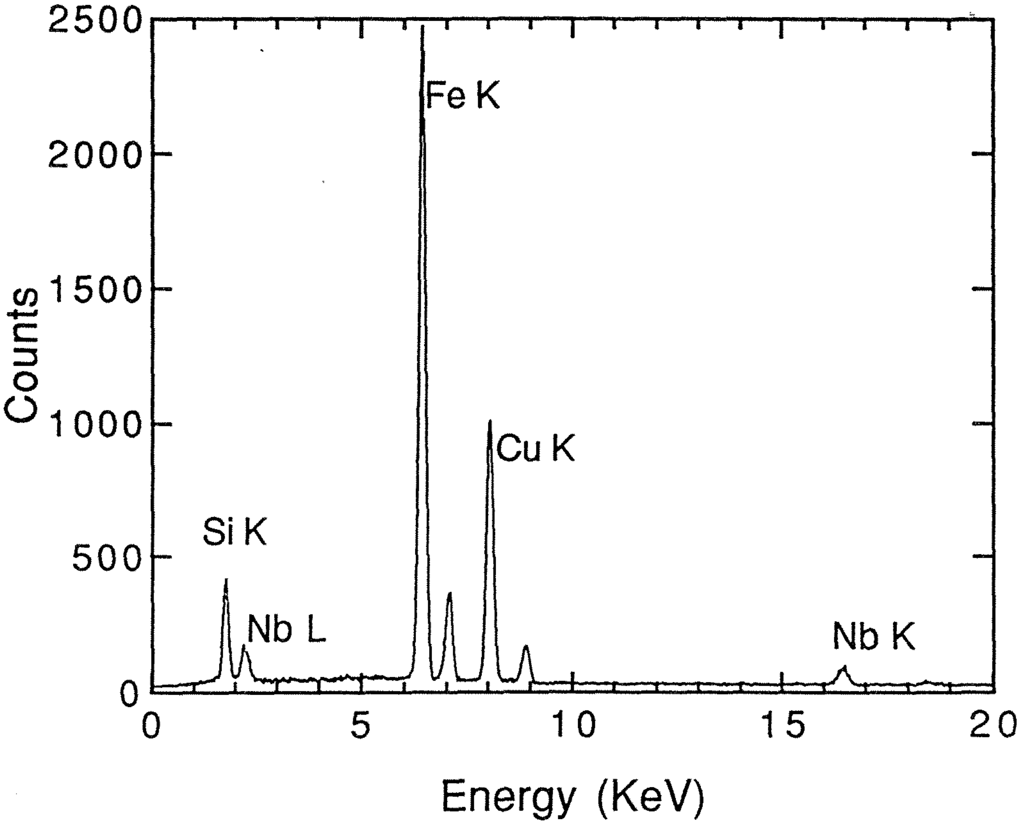

Figure 3.9 EDX spectrum from ball milled $(Fe_3Si)_{0.95}Nb_{0.05}$ alloy. The Cu peaks are from copper sample holder.

Other experimental techniques were used to characterize the structure and measure the properties of the materials in this thesis research work. These include differential scanning calorimetry (DSC) with a Perkin Elmer DSC-4 calorimeter, and magnetic property measurements with a vibration sample magnetometer at the National Institute of Standards and Technology. Extended electron energy-loss fine structure spectrometry studies of ordering of the same alloys was also performed extensively by a colleague at Caltech (Okamoto 1993).

References

BENJAMIN, J. S.: *Metall. Trans.*, **1**, 2943 (1970).

BENJAMIN, J. S.: *Sci. Amer.*, **234**, 40 (1976).

ECKERT, J.; HOLZER, J. C.; KRILL, C. E. and JOHNSON, W. L.: J. *Mater. Res.;* **7**, 1751 (1992).

FULTZ, B. and GAO, Z. Q.: *Nucl. Instr. and Methods in Phys. Res.*, **B 76**, 115 (1993).

FULTZ, B.; GAO, Z. Q.; HAMDEH, H. H. and OLIVER, S. A.: *Phys. Rev.*, **B**, (1994).

FULTZ, B.: "Chemical Systematics of Iron-57 Hyperfine Magnetic Field Distributions in Iron Alloys," in Mössbauer Spectroscopy Applied to Magnetism and Materials Science, G. J. Long and F. Grandjean, eds., (Plenum Press, New York, 1993) Chapter 1, p. 1.

FULTZ, B.; Le CAËR, G. and MATTEAZZI, P.: *J. Mater. Res.;* **4**, 1450 (1989).

HAMDEH, H. H.; OLIVER, S. A.; FULTZ, B. and GAO, Z. Q.: *J. Appl. Phys.,* **74**, 5117 (1993).

KLUG, H. P. and ALEXANDER, L. E.: X-ray Diffraction Procedures For Polycrystalline and Amorphous Materials, (John Wiley & Son, New York 1974).

KOCH, C. C.: *Nanostructured Materials*, **2**, 109 (1993).

KOCH, C. C.; CAVIN, O. B.; MCKAMEY, C. G. and SCARBROUGH, J. O.: *Appl. Phys. Lett.*, **43**, 1017 (1983).

LE CAËR, G. and DUBOIS, J. M.: *J. Phys.* **E 12**, 1083 (1979).

MARCINKOWSKI, M. J. and BROWN, N.: *J. Appl. Phys.*, **33**, 537 (1962).

OKAMOTO, J. K.: Ph.D. Thesis, California Institute of Technology, (1993).

ROTELLA, F. J.: *"User Manual for Rietveld Analysis of Time-of-Flight Neutron Powder Diffraction Data at IPNS,"* (1983).

SCHOONE, R. D. and FISHIONE, E. A., *Rev. Sci. Inst.*, **37**, 1351(1966).

SHINGU, P. H.; HUANG, B.; NISKITANI, S. R. and NASU, S.: *Suppl. to Trans JIM*, **29**, 3 (1988).

STEARNS, M. B.: *Phys. Rev.*, **129**, 1136 (1963).

STEARNS, M. B.: *Phys. Rev.*, **B 6**, 3326 (1972).

VASILEV, Y. P.; KAMARDIN, I. F.; SKATSKII, V. I.; CHERMOMORCHENKO, S. G. and SCHUPPE, G. N.: *Trudy. Stred. Gos. Univ. in u. i. Lenina*, **65**, 47 (1955).

WARREN, B. E., X-Ray Diffraction, (Addison-Wesley, Reading, Mass.1969), Chapter 12.

WARREN, B. E. and AVERBACH, B. L.: *J. Appl. Phys.*, **21**, 595 (1950).

WILSON, A. J. D.: X-ray Optics, (Methen, London 1949).

YERMAKOV, A. Y.; YURCHIKOV, Y. Y. and BARINOV, V. A.: *Phys. Met. Metall.*, **52**, 50 (1981).

Chapter 4 Kinetics of Ordering in Fe_3Al, Fe_3Si and Fe_3Ge

Using the methods described in last chapter, we can obtain both short range order (SRO) parameters and long range order (LRO) parameters from Mössbauer spectrometry data and x-ray diffraction data, respectively. By plotting the kinetic paths through the space spanned by these order parameters, we can study the intermediate microstructural changes during disorder → order transformations.

In this chapter I used kinetic paths as a tool to investigate the kinetics of disorder → order transformations in binary Fe_3Al, Fe_3Si and Fe_3Ge in Sections §4.1, §4.3 and §4.4, respectively. In Section §4.2 I present an observation of transient B32 order in Fe_3Al.

§4.1 Kinetic Paths for Binary Fe_3Al

The phase diagram for Fe_3Al is presented in Figure 4.1. Ordered structures are shown in Figure 1.3. In thermodynamic equilibrium, Fe - 25 at.% Al assumes the A2 (bcc) structure at high temperatures, and the B2 structure at temperatures below about 800°C. The B2 structure cannot be a ground state structure for the Fe_3Al stoichiometry, however, because it provides for only random occupancy of one of its two sublattices. Below 550°C, the $D0_3$ structure is the equilibrium state for Fe - 25 at.% Al. The B32 ordered structure does not appear anywhere in the Fe-Al phase diagram.

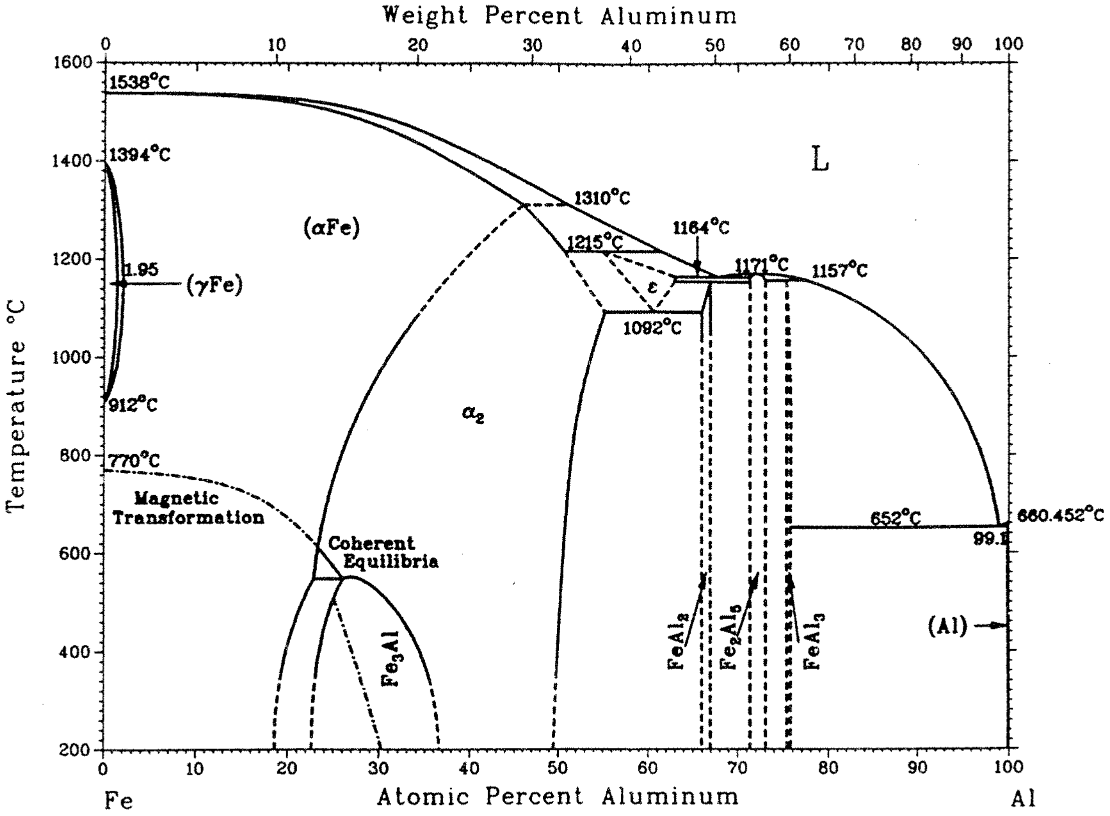

Figure 4.1 Thermodynamic equilibrium phase diagram for Fe-Al alloy. (α: A2. α2: B2. Fe_3Al: $D0_3$.) (From Binary Alloy Phase Diagrams, edited by Massalski *et al.*. 1990.)

There have been several previous studies of ordering kinetics in Fe_3Al (Swann, Duff and Fisher 1969; Okamoto and Beck 1971; Oki, Hasaka and Eguchi 1973 and 1974; Allen and Cahn 1975 and 1976; Park, Stephenson, Allen and Ludwig 1992). Most of these studies were concerned with ordering transformations that occurred near the critical temperatures of B2 or $D0_3$ ordering. The present work involved ordering in alloys that were severely undercooled.

The kinetic path for long range ordering in Fe_3Al was also studied previously by Anthony and Fultz (Anthony and Fultz 1989b). In their work, rapid solidified powders of Fe_3Al were annealed to develop LRO. As the samples were annealed at different temperature, the LRO parameters for $D0_3$ order and B2 order, as measured with the intensities of $(\frac{1}{2}\ \frac{1}{2}\ \frac{1}{2})$ and (100) superlattice diffractions respectively, developed at different rates. (Figure 4.2 shows the kinetic paths of LRO for Fe_3Al.) At lower temperatures the relative rate of B2 ordering is higher than at higher temperatures. The relative difference in rates of B2 and $D0_3$ ordering was interpreted with analytical kinetic theories, including the master equation method in the point (Bragg-Williams) approximation (Anthony and Fultz 1989a), and the path probability method in the pair (Bethe) approximation (Anthony and Fultz 1994). From these theoretical calculations and Monte Carlo simulations (Anthony and Fultz 1994), temperature dependencies of kinetic paths through B2 and D03 order parameters were obtained for various ratios of first-nearest-neighbor (1nn) interatomic interaction strengths to second-nearest-neighbor (2nn) interatomic interaction strengths .

In this thesis work, Mössbauer spectroscopy and X-ray diffractometry were used to further study the kinetic paths of SRO and LRO for Fe_3Al. Two typical Mössbauer spectra for Fe_3Al are presented in Figure 4.3. These spectra comprise a sum of overlapping ferromagnetic sextets. The distribution of ^{57}Fe hyperfine

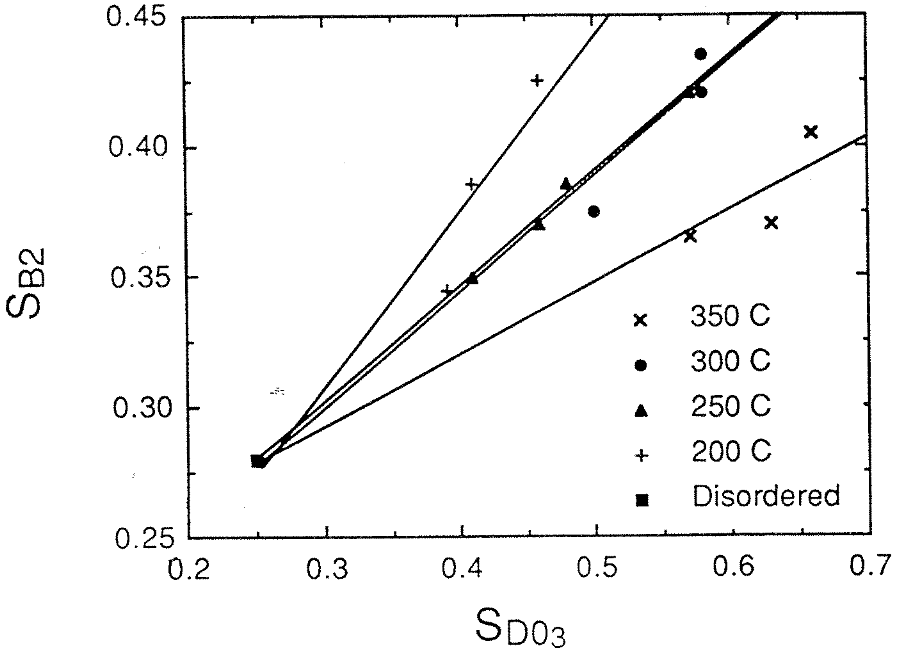

Figure 4.2 Kinetic paths of long range order (LRO) for Fe_3Al as measured by X-ray diffraction (From Anthony and Fultz 1989b). The definition of LRO parameters is slightly different, but nevertheless kinetic paths are different for samples annealed at different temperatures.

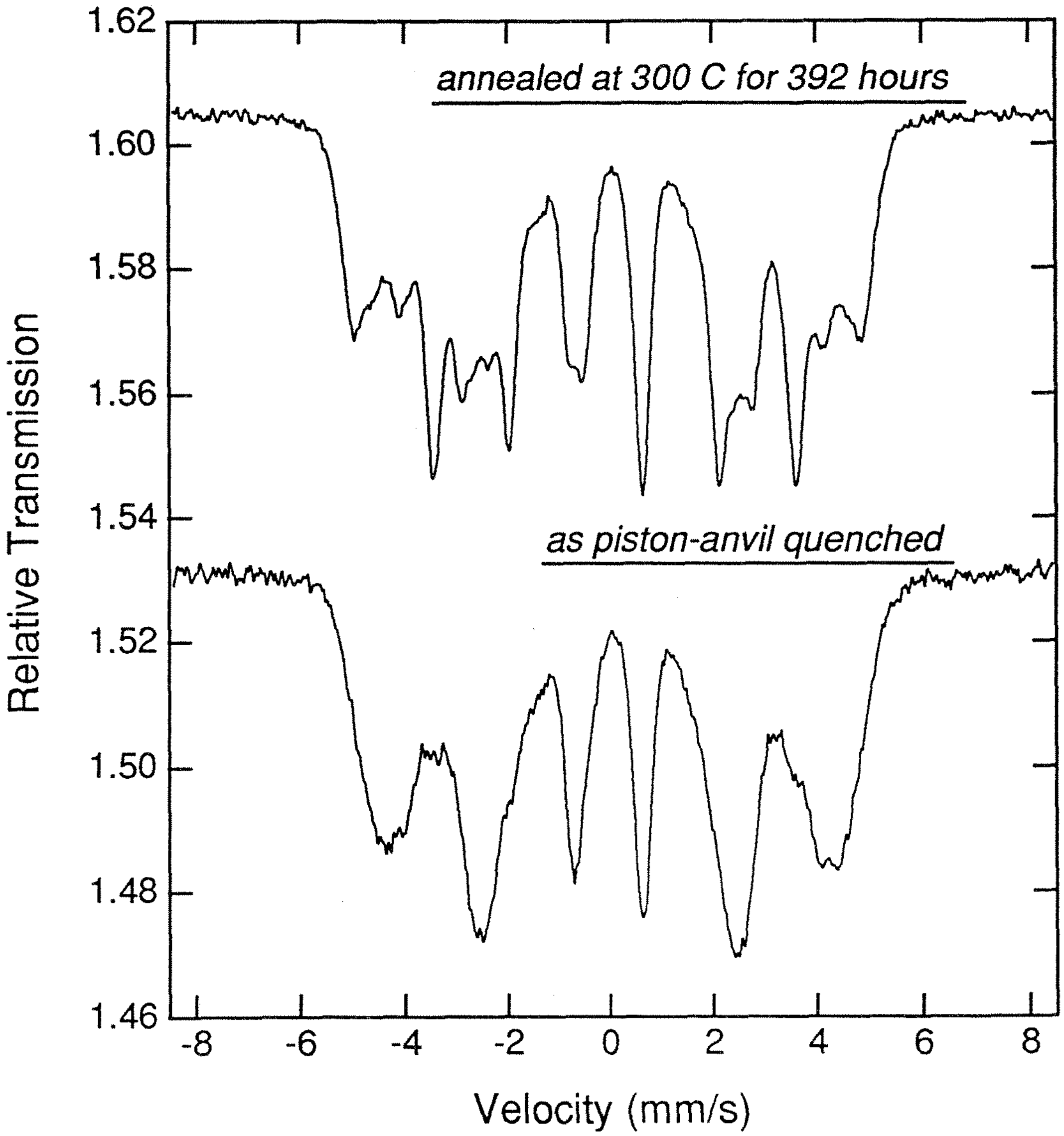

Figure 4.3 Mössbauer spectra of Fe_3Al as-quenched and after annealed at 300 °C for 392 hours.

magnetic fields (HMFs) can be obtained by processing these spectra using the method of Le Caër and Dubois (Le Caër and Dubois 1979). A set of HMF distributions from an annealing sequence is presented in Figure 4.4. Semi-quantitatively, these HMF distributions can be interpreted with a simple model in which the HMF at a particular ^{57}Fe atom is reduced in proportion to the number of Al atoms in its 1nn shell (Fultz, Gao and Hamdeh 1990; Fultz, Gao and Anthony 1991). The peaks in Figure 4.4 are labeled by the number of 1nn Al atoms around the ^{57}Fe atom. The intensities of these peaks correspond approximately to the probability of each 1nn environment.

Kinetic paths of short-range ordering for specimens of Fe_3Al annealed at 200°C and 300°C are presented in Figure 4.5. The axes of Figure 4.5 are the probabilities of the (0) 1nn and (4) 1nn Al environments. Here we show how the different kinetic paths at 200°C and 300°C can be related to the different ordered structures. To do so we employ the information of Figure 1-**3** on the probabilities of the different 1nn environments for the different ordered structures. Assuming that the growth of a region of ordered structure occurs at the expense of the disordered A2 structure, we can calculate some possible slopes and directions for kinetic paths. Starting at the disordered state in the lower left of Figure 4.5, the initial part of the kinetic path proceeds with a slope, k, given by:

$$k = \frac{\Delta P(0)}{\Delta P(4)}, \tag{4.1}$$

where $\Delta P(j)$ is the change in the probability of Fe atoms with j Al atoms in their 1nn shell, with respect to the probability in the disordered A2 structure:

$$\begin{aligned} \Delta P(j) = {} & f_{D03}[P_{D03}(j) - P_{A2}(j)] + f_{B2}[P_{B2}(j) - P_{A2}(j)] \\ & + f_{B32}[P_{B32}(j) - P_{A2}(j)], \end{aligned} \tag{4.2}$$

where f_{D03}, f_{B2}, and f_{B32} are the fractions of the three ordered structures that grow

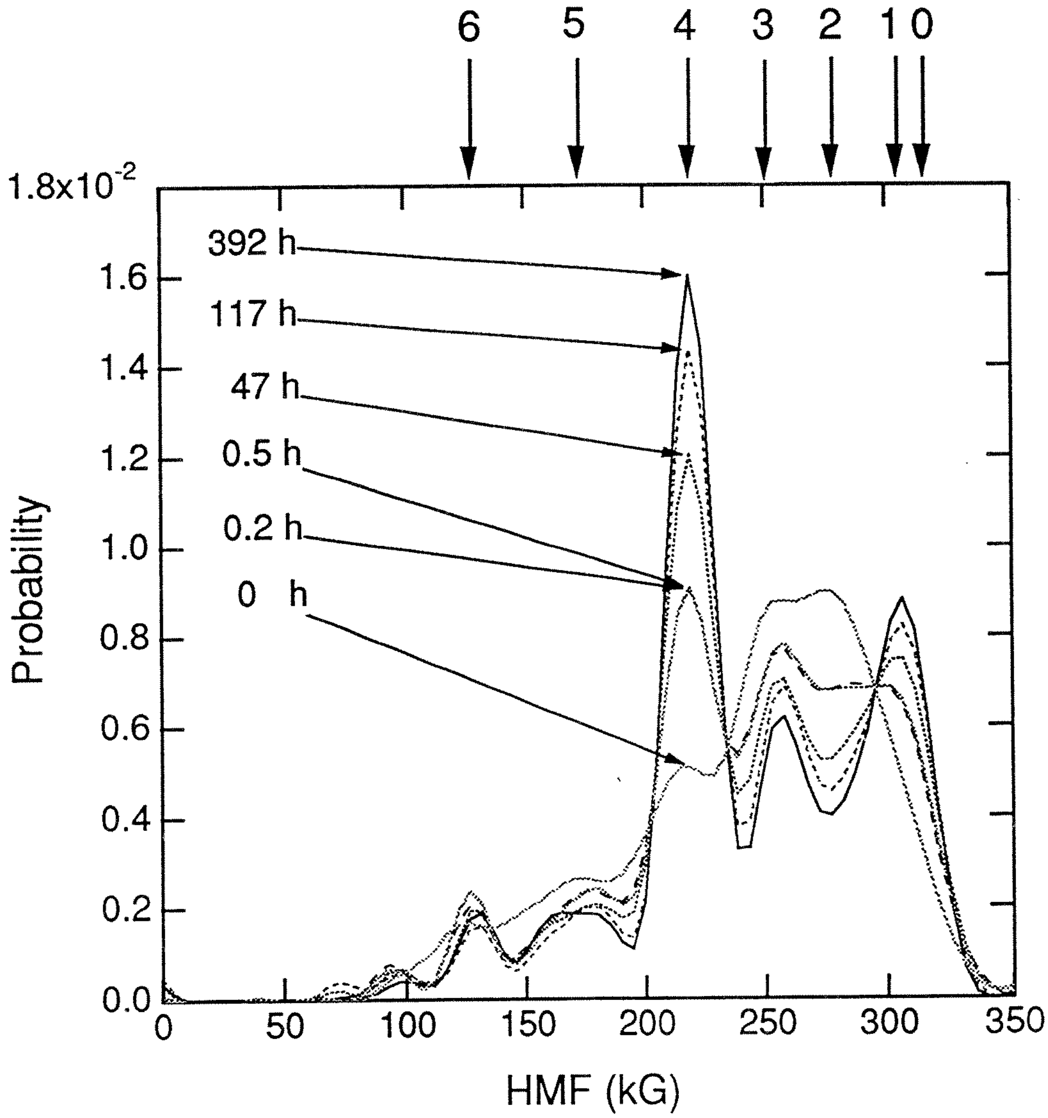

Figure 4.4 Hyperfine magnetic field distributions for the as-quenched Fe_3Al sample and Fe_3Al samples after annealing at 300 °C for various times. Number on top of the figure identify the resonances from ^{57}Fe atoms with different numbers of 1nn Al atoms.

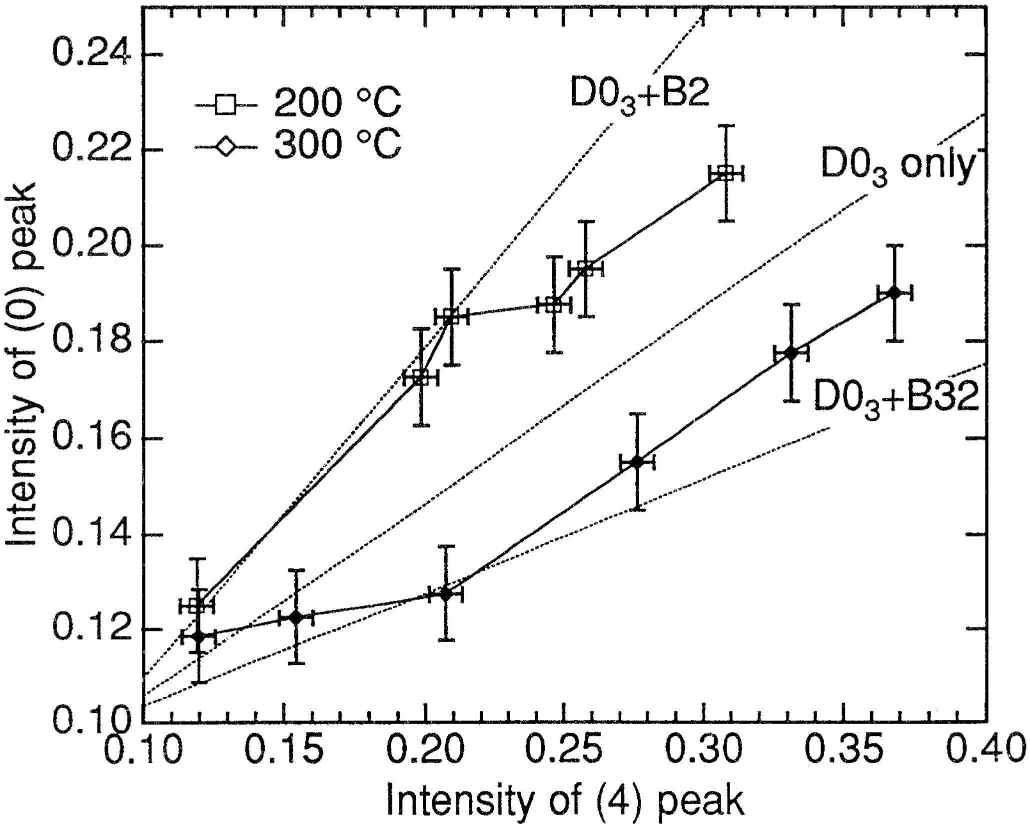

Figure 4.5 Experimentally derived kinetic paths of short range ordering (SRO) for Fe_3Al. The nearly-disordered initial state is on the lower left . The dotted lines were calculated by assuming the growth of D0$_3$ order only (center), 50% D0$_3$ order with 50% B2 order (top), and 25% D0$_3$ order with 75% B32 order (bottom).

from the disordered A2 structure, and

$$f_{D03} + f_{B2} + f_{B32} + f_{A2} = 1. \tag{4.3}$$

Here $P_{D03}(j)$, $P_{B2}(j)$, $P_{B32}(j)$, and $P_{A2}(j)$ are the probabilities of the (j) 1nn environments for the four possible ordering structures, which can be obtained from Figure 1.3. Because $P_{D03}(j)$, $P_{B2}(j)$, $P_{B32}(j)$, and $P_{A2}(j)$ are constants, the slope of the kinetic path depends only on the fractions of the structures (the f_i's).

We used different relative growth rates for $D0_3$, B3, and B32 order from the A2 structure in drawing the three dotted lines in Figure 4.5. The central line corresponds to the growth of $D0_3$ order only ($f_{D03} > 0$; $f_{B2} = f_{B32} = 0$). If there is also some growth of excess B2 order, $\Delta P(0)$ would be larger, so the slope, k, would be greater (compare $P_{B2}(0)$, $P_{B2}(4)$, $P_{D03}(0)$ and $P_{D03}(4)$ on Figure 1.3). On the other hand, the additional growth of B32 order would suppress the slope, k. The two additional dotted lines in Figure 4.5 correspond to the growth of 50% $D0_3$ order with 50% B2 order, and 25% $D0_3$ order with 75% B32 order. Comparing these lines with the experimental data, we see that the sample annealed at 300 °C shows a clear tendency to evolve some excess B32 order. The sample annealed at 200 °C may show a tendency to evolve excess B2 order while $D0_3$ order is developing. These results should not be considered rigorous because the ordered structures do not develop by simply replacing a region of A2 structure; the ordering process is more continuous. Nevertheless, these interpretations do show the qualitative trends in the local chemical environments.

It can be concluded that, for Fe_3Al, short range ordering also shows different kinetic paths when disordered samples are annealed at different temperatures. If the sample is annealed at lower temperature, there is a tendency to develop B2 order as well as $D0_3$ order. This is consistent with previous LRO kinetic paths studies (Anthony and Fultz 1989b). When the disordered sample is annealed at 300 °C, which is relative high temperature considering the critical temperature for $D0_3$ order is about 550 °C, the alloy tends to develop excess B32 order.

§4.2 Transient B32 Order in Binary Fe_3Al

Experimental Evidence and Interpretation

Since the Fe - Al phase diagram contains large regions of B2 and $D0_3$ order, it seems that both 1nn and 2nn interactions in Fe_3Al favor 1nn and 2nn Fe-Al pairs, as opposed to Fe-Fe and Al-Al pairs. The B32 structure, with its equal numbers of like and unlike 1nn pairs, would therefore not be expected in thermodynamic equilibrium, and the B32 structure is not a ground-state structure when 1nn interactions favor ordering (Richards and Cahn 1971; Allen and Cahn 1972). No B32 phase appears on the Fe - Al phase diagram (Figure 4.1). Recently there has been a report of observing B32 order in Fe - 20at. % Al (Schweika 1990), but the heat treatment of the sample was not well controlled.

From the kinetic path study of SRO in Fe_3Al (Section §4.1), we found that there is a tendency for developing transient B32 during the early stages of ordering during annealing at 300 °C. We obtained further evidence of this transient B32 structure by X-ray diffraction. Figure 4.6 presents the $(\frac{1}{2}\ \frac{1}{2}\ \frac{1}{2})$ and (100) x-ray superlattice diffraction peaks from the Fe_3Al sample annealed for increasing times at 300°C. (The HMF distributions for the same samples were shown in Figure 4.4.) The data from the piston-anvil quenched state were subtracted from those of the annealed states to correct for background irregularities of the PSD. In the first few

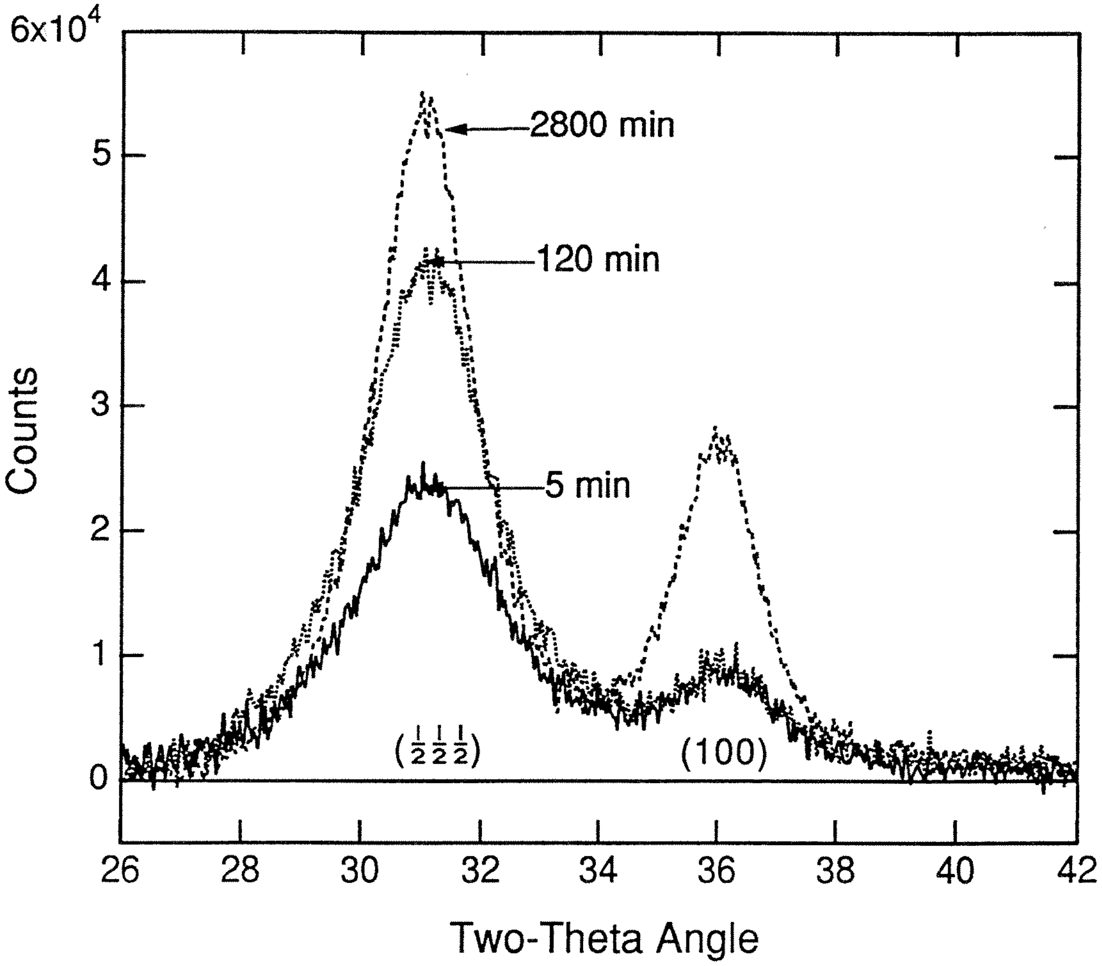

Figure 4.6 Growth of superlattice diffraction peaks in initially piston-anvil quenched Fe_3Al samples annealed at 300 °C for various times.

minutes of annealing, the $(\frac{1}{2}\frac{1}{2}\frac{1}{2})$ and (100) diffraction peaks increase together, and in approximately the 2:1 ratio expected for $D0_3$ order. The big surprise occurs between 5 minutes and 120 minutes. During this time the $(\frac{1}{2}\frac{1}{2}\frac{1}{2})$ peak nearly doubles in intensity while the (100) peak intensity remains virtually constant. (This is not an effect of texture; we verified that the fundamental peaks maintained the same ratio of intensities.) Table 3.2 in Chapter 3 shows that this independent growth of the $(\frac{1}{2}\frac{1}{2}\frac{1}{2})$ peak is characteristic of the growth of B32 order. With further annealing time, however, the (100) peak grows again and the $(\frac{1}{2}\frac{1}{2}\frac{1}{2})$ and (100) diffraction peaks eventually attain the 2:1 intensity ratio characteristic of $D0_3$ order. This is seen in the data obtained after 2800 minutes of annealing.

Since the fundamental diffraction peaks are sharp, we attribute the breadth of these superlattice diffraction peaks to a distribution of small domain sizes. For these three annealing times, a simple Scherrer line broadening analysis gives the domain sizes presented in Table 4.1.

The domain size is further confirmed with transmission electron microscopy. Figure 4.7 shows the dark field images for Fe_3Al from both $(\frac{1}{2}\frac{1}{2}\frac{1}{2})$ and (100) superlattice diffractions. By comparing the morphological features in the diffraction contrast with the domain sizes in the computer-simulated alloy (Section §3.4), we find that the domain sizes range from 30 to 50 Å. These domain sizes are consistent with those from superlattice peak broadening in x-ray diffraction patterns. It is interesting that the features in the diffraction contrast from the $(\frac{1}{2}\frac{1}{2}\frac{1}{2})$ and (100) diffraction are so similar in size. This supports the model microstructure with independent nucleation of $D0_3$ domains without prior formation of B2 order. If the $D0_3$ domains were to nucleate within B2 domains, we would expect the B2 domains to be larger. We also note that in both simulated and experimental images, the (100)

Table 4.1. Domain sizes from superlattice diffraction peak broadening as a function of annealing time.

Annealing time (min.)	$(\frac{1}{2}\frac{1}{2}\frac{1}{2})$ domain size (Å)	(100) domain size (Å)
5	27	45
120	31	48
2800	31	51

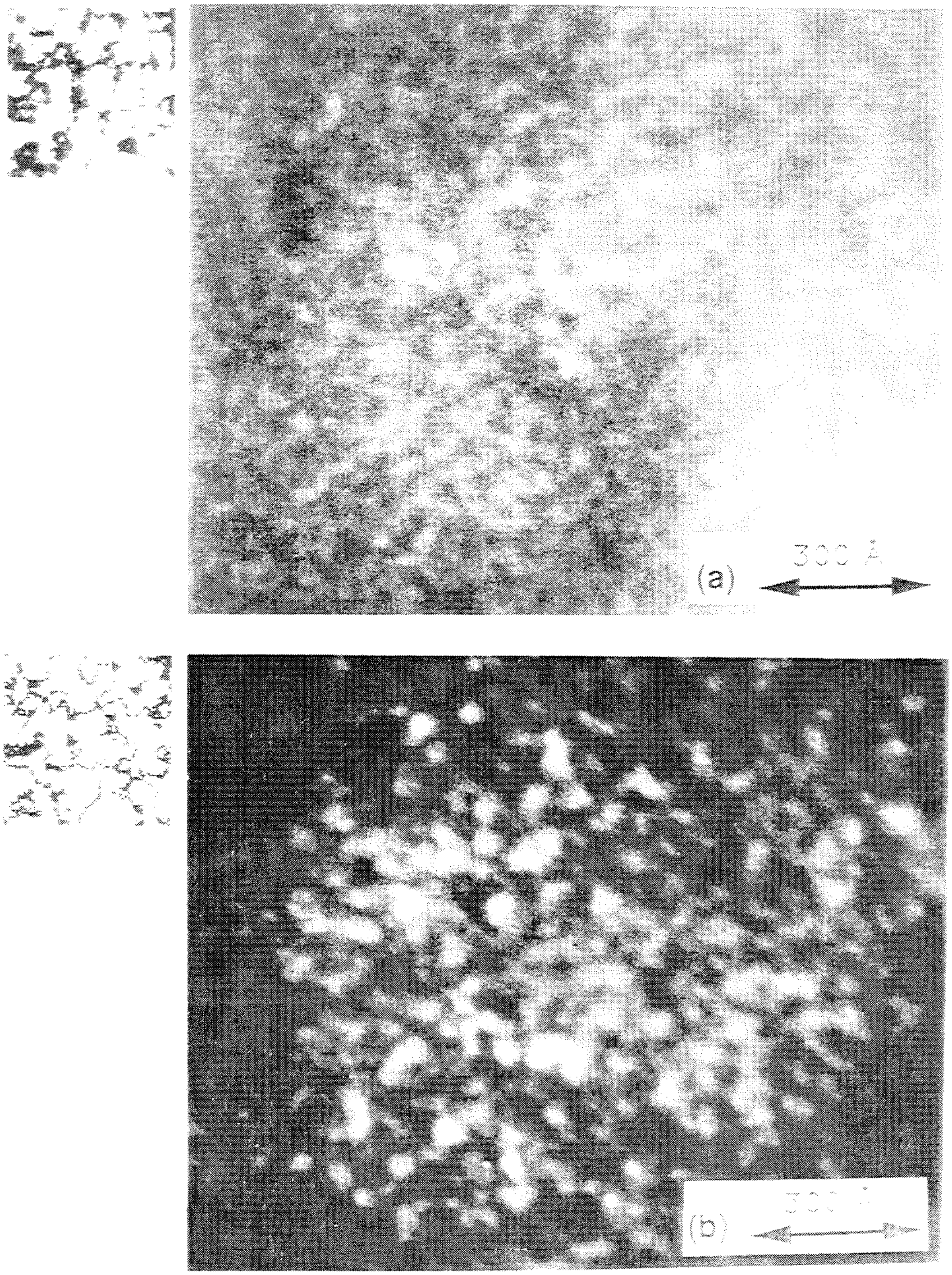

Figure 4.7Dark-field micrographs from (a) $(\frac{1}{2}\ \frac{1}{2}\ \frac{1}{2})$ and (b) (100) superlattice diffractions. The specimen was a foil of piston-anvil-quenched Fe_3Al that was annealed *in situ* at 300 °C for 1 hour with a heating holder in the TEM. Simulated images with approximately the same scale are in the upper left-hand corners.

dark field image has stronger diffraction contrast and relatively sharper boundaries than does the $(\frac{1}{2}\frac{1}{2}\frac{1}{2})$ image.

As compared with Figure 1.3, the HMF distribution from the as-quenched sample (see Figure 4.4) is approximately a binomial distribution, consistent with a nearly random solid solution. During the first ten minutes of annealing at 300°C, there is a rapid growth of the (0) 1nn Al peak and the (4) 1nn Al peak as all other peaks decrease in intensity. This is consistent with the growth of $D0_3$ order from disordered material. The HMF distribution remains almost unchanged from about 10 minutes to 100 minutes. After 100 minutes the (0) 1nn Al peak and the (4) 1nn Al peak grow further as all other peaks decrease in intensity. Because of the similarity of the HMF distribution for the B32 structure and the A2 structure (see Figure 1.3), we expect that from 10 to 100 minutes there may be the development of B32 order from the A2 structure. This is consistent with the x-ray diffractometry evidence.

Summarizing all the experimental evidence of this section and Section §4.1, we believe we have observed a transient formation of B32 order during the A2 → D03 transformation at 300°C. The salient feature of the x-ray data is the independent growth of the $(\frac{1}{2}\ \frac{1}{2}\ \frac{1}{2})$ diffraction peak, without growth of the (100) peak, during annealing at 300°C for times between 5 and 120 minutes. During this time interval, the ^{57}Fe HMF distribution undergoes little change, as expected if there is an A2 → B32 transformation. The kinetic path at 300°C (Figure 4.5) shows a clear tendency to form some B32 order. We propose two possible explanations for this B32 structure, but both lead to essentially the same conclusion. The simplest explanation is that there are regions in the material where the B32 structure forms transiently. From the large superlattice peak broadening and the small features of Figure 4.7, it is clear that these regions must be small, in the range of 30-50 Å. This is an inconvenient spatial scale for experimental characterization, and we cannot yet isolate these regions in our experimental TEM images, for example.

We suggest a second explanation for the transient B32 order. It may originate from boundaries between extremely small $D0_3$ domains that form as densely-nucleated $D0_3$ domains grow to impingement. When the domain size is extremely small, many of the atoms in the crystal are actually sitting on the antiphase domain boundaries (APDB). If two adjacent $D0_3$ domains have an $a(\frac{1}{2}\frac{1}{2}\frac{1}{2})$ fault vector, the antiphase domain boundary will have a local B32 structure. (Statistically, half of these boundaries will appear locally as pure Fe, depending on the plane of the boundary, but such Fe-rich regions are required for homogeneous B32 order if the composition is 25 at.% Al.) The APDB's with the $a(\frac{1}{2}\frac{1}{2}\frac{1}{2})$ fault vector contribute to the excess $(\frac{1}{2}\frac{1}{2}\frac{1}{2})$ diffraction intensity. Another type of APDB with an a(100) fault vector is also expected between adjacent $D0_3$ domains (Marcinkowski and Brown 1962). This APDB has a local B2 structure and contributes to the (100) diffraction intensity. (Again, half of these boundaries will appear locally as pure Fe, but such Fe-rich regions are required for homogeneous B2 order if the composition is 25 at.% Al.) If all four variants of $D0_3$ domains nucleate independently and with equal probability, the $a(\frac{1}{2}\frac{1}{2}\frac{1}{2})$ fault vector will be present in the ratio of 2:1 with respect to the a(100) fault vector. The 2:1 abundance of these two types of boundaries will preserve the 2:1 intensity ratio of the $D0_3$ superlattice diffraction. (This is consistent with the fact that APDB's do not detract from the integrated intensity of superlattice diffractions (Warren 1969).) So to complete our second explanation for the B32-like diffraction pattern, we must assume a preference for APDB's with the $a(\frac{1}{2}\frac{1}{2}\frac{1}{2})$ fault vector. What could be interpreted as B32 order may in fact originate from the formation of more APDB's with an $a(\frac{1}{2}\frac{1}{2}\frac{1}{2})$ fault vector. Nevertheless, the second explanation of a preference for APDB's with the $a(\frac{1}{2}\frac{1}{2}\frac{1}{2})$ fault vector is similar to the first explanation that there are local regions with B32 order; both explanations involve a preference for local B32-like order.

This tendency for B32 ordering is transient, and disappears with further annealing. After annealing for more than 2 hours, the intensities of the $(\frac{1}{2}\,\frac{1}{2}\,\frac{1}{2})$ and (100) diffraction peaks approach the 2:1 ratio characteristic of $D0_3$ order. The HMF distribution also evolves towards that of $D0_3$ order. Using the first explanation, we propose that the local regions of B32 order disappear. Using the second explanation, we propose a reduced preference for APDB's with the $a(\frac{1}{2}\,\frac{1}{2}\,\frac{1}{2})$ fault vector as the domains grow.

Initial Conditions

It was found that the ordering kinetics was sensitive to the initial state of the samples. As a liquid droplet of Fe_3Al is quenched to room temperature, it passes through the temperature region of 800°C to 550°C where the equilibrium state is B2 order. If the cooling rate is insufficient, the quenched sample may contain some incipient B2 order. The cooling rate of our piston-anvil quenching seems just adequate for obtaining a disordered solid solution (see argument in Section §3.1). For a number of quenches the copper surfaces of the ultra-rapid quenching apparatus were improperly prepared, leading to an insufficient cooling rate for suppressing B2 order. Weak (100) superlattice diffractions were obtained in their X-ray diffraction patterns. The kinetics of ordering in these samples were strikingly different from those quenched more rapidly. With some initial B2 order, there was no transient formation of B32 order, and the samples showed a strong tendency to develop excess B2 order.

Transient B32 order has been found in analytical calculations (Anthony and Fultz 1989a). Figure 4.6 shows the evolution of B2, D03 and B32 order parameters

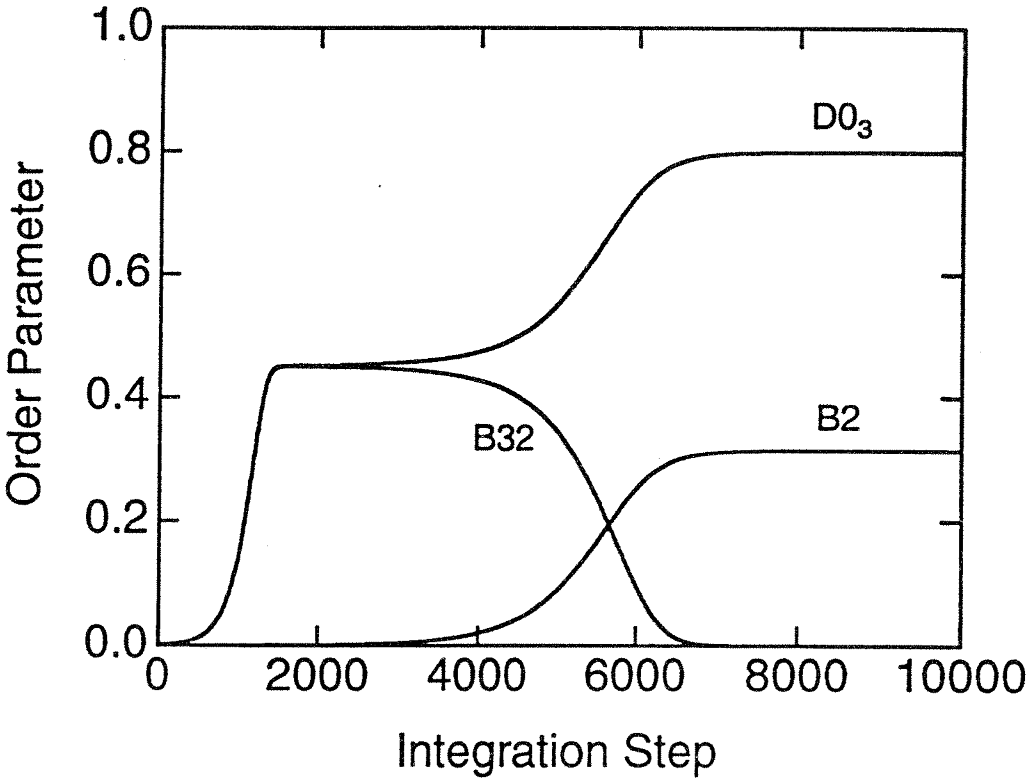

Figure 4.8 Evolution of B2, D03 and B32 order parameters with the kinetic master equation method ($V_{AA}{}^1 = V_{AA}{}^2 = 1.60$). (From Anthony and Fultz 1989a).

by calculations with kinetic Master Equation (in the point approximation with a four-sublattice model). With strong 2nn interactions, the B32 ordered structure appeared in the early stages of ordering.

The free energy calculated for the alloy may give us some hints as to the appearance of B32 order structure (Anthony 1993). Figure 4.9 shows the surface plot of the free energy as a function of i and k, the solute occupancies on two adjacent sublattices in the four-sublattice model. Figure 4.10 shows the contour plot of the free energy as a function of i and k for the same system. The initial disordered state corresponds to the point (i, k) = (0.25, 0.25) in Figures 4.9 and 4.10. At early stages of ordering, the kinetic path took the alloy from its initial disordered state to the neighborhood of (i, k) ≈ (0.5, 0.5). This seems reasonable, since that is the direction of steepest descent in free energy. The point near (i, k) ≈ (0.5, 0.5) corresponds to the transient B32 state, and it is a saddle point in the free energy surface. The system eventually leaves the neighborhood of the saddle point and evolves in the direction to the global minimum at (i, k) = (1, 0), or equivalently, (0, 1). This corresponds to the disappearance of the transient B32 order and the development of the equilibrium $D0_3$ order, as observed in Figure 4.8.

Some features of the differential equations used to obtain the results of Figure 4.8 are closely analogous to the experimental observation that no excess B32 order evolved in alloys improperly quenched so that they contained some incipient B2 order. As solutions to differential equations, the results shown in Figure 4.8 were strongly sensitive to the initial conditions of the alloy [Fultz and Anthony, private communication 1994]. At the disordered state of the alloy (with equal occupancies on the four sublattices, i.e., i = 0.25, j = 0.25, k = 0.25, l = 0.25) the rates of change of the sublattice occupancies are precisely balanced. Some initial imbalance is required

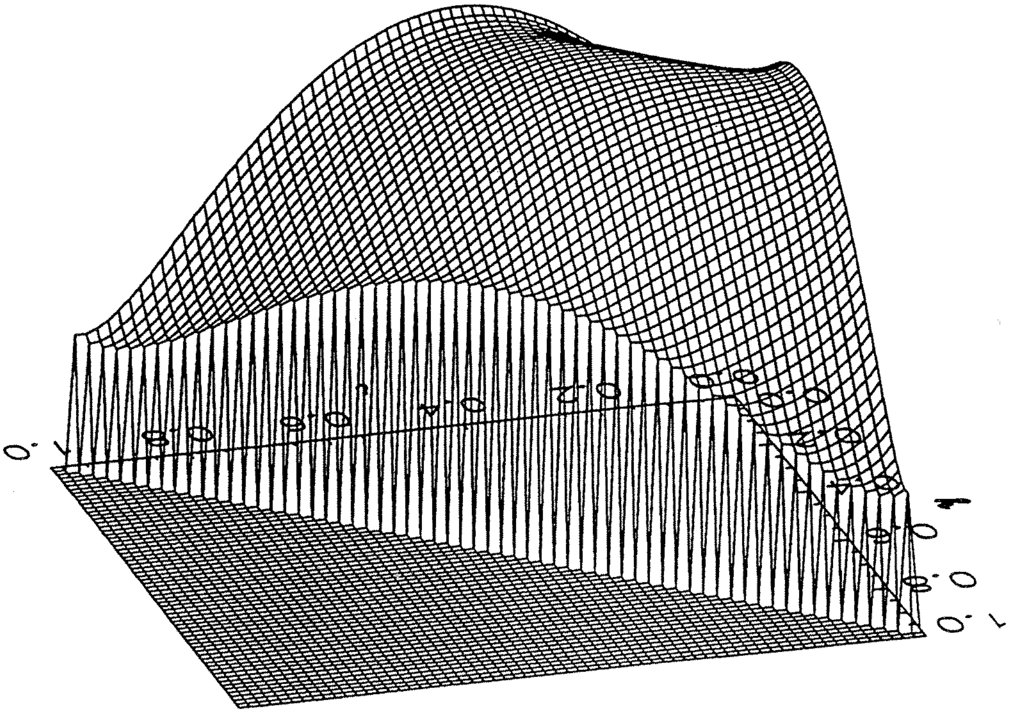

Figure 4.9 Surface plot of the free energy as a function of i and k for the system of Figure 4.8. (From Anthony 1993).

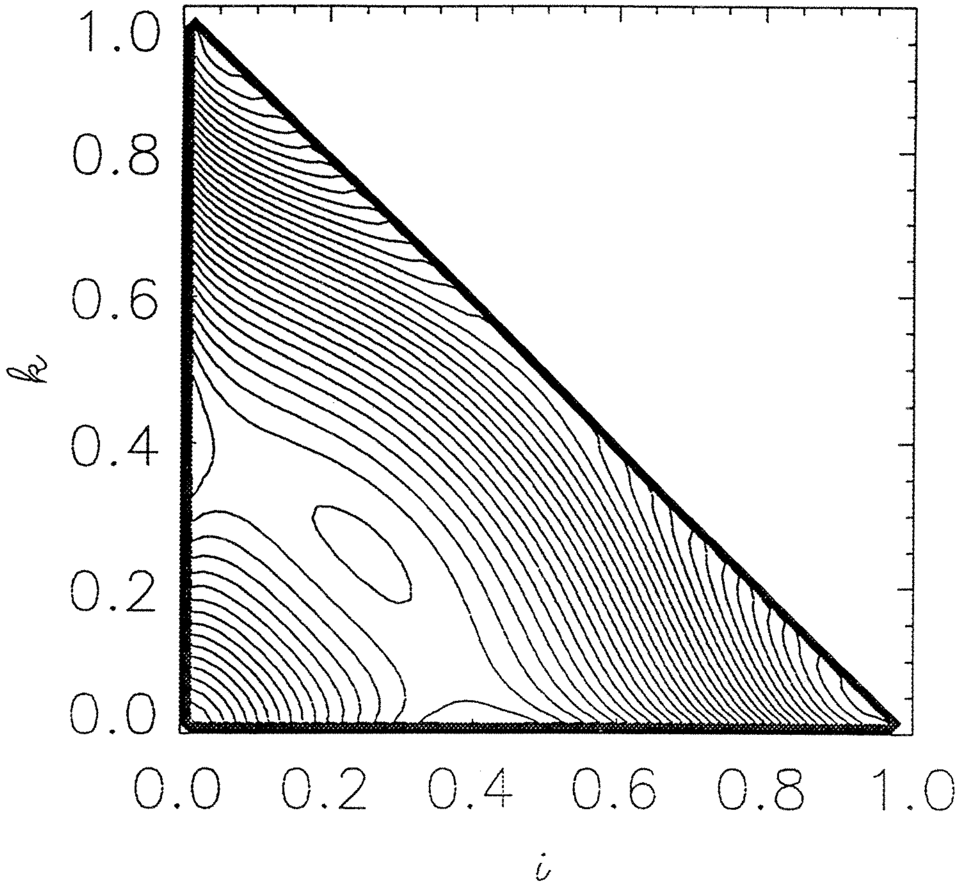

Figure 4.10 Contour plot of the free energy as a function of i and k for the system of Figure 4.8. (From Anthony 1993).

to start the kinetics. The results presented in Figure 4.8 were obtained with i = 0.25+ε, j = 0.25-ε, k = 0.25+ε, l = 0.25-ε, which is a slight bias towards B32 order (this can be seen with Figure 1.1 and the assignment of i, j, k, l to the sublattices α, β, γ, δ). This slight bias evolves into a strong transient B32 state, as shown in Figure 4.8. On the other hand, for an initial bias towards B2 order (such as i = 0.25+ε, j = 0.25+ε, k = 0.25-ε, l = 0.25-ε), there is no formation of transient B32 order. This observation from kinetic rate equations seems consistent with the free energy surface presented in Figure 4.10. Starting with a B2 bias towards higher i and lower k, the contours of the free energy function suggest a more horizontal kinetic path that leads more directly into the lower right corner corresponding to $D0_3$ order. When there is a positive occupancy bias for the β-sublattice as well, this kinetic path would exhibit excess B2 order.

§4.3 Kinetic Paths for Binary Fe_3Si

The phase diagram for Fe-Si is presented in Figure 4.11. The most significant difference between the Fe-Si phase diagram and the Fe-Al phase diagram is the Fe - 25 at.% Si alloy has a much higher critical temperature of ordering. Actually, for Fe_3Si the state of $D0_3$ order is thermodynamically stable up to the melting point. This implies that the interatomic interactions favoring order in Fe_3Si are much stronger tendency than in Fe_3Al. Because of the difficulty of disordering Fe_3Si, very little work has been done to study the early stage kinetics of disorder → order transformations.

As described in the previous chapter, using ball-milling we have successfully prepared disordered bcc Fe_3Si. Mössbauer spectra from as-milled and annealed Fe_3Si

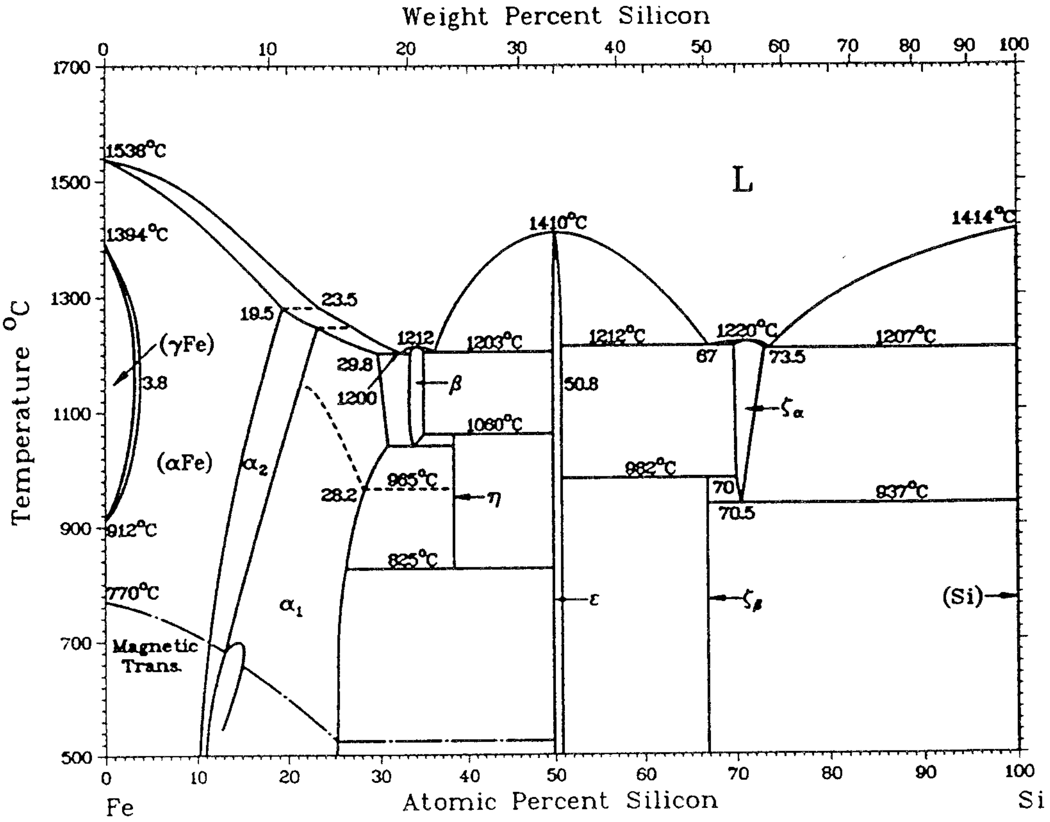

Figure 4.11 Thermodynamic equilibrium phase diagram for Fe-Si.

(α: A2. α1: $D0_3$. α2: B2. β: *h*P8. η: $D8_8$. ε: B20.)

(From Binary Alloy Phase Diagrams, edited by Massalski *et al.* 1990.)

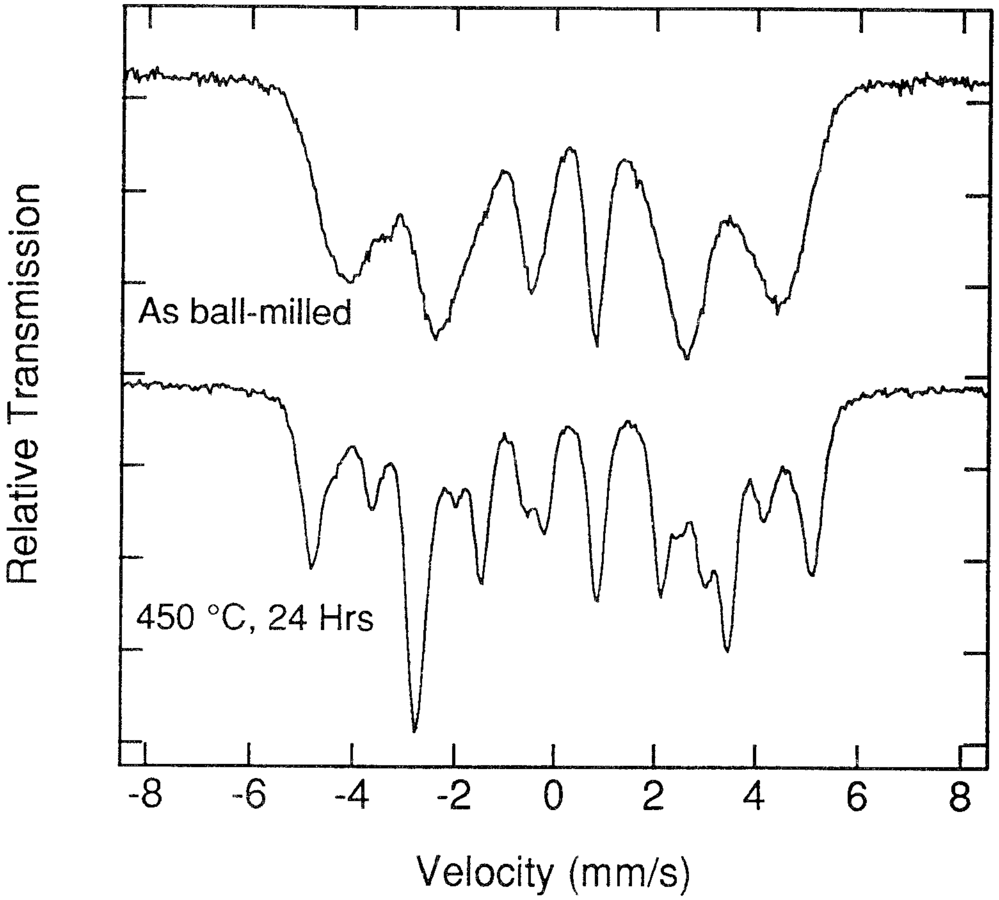

Figure 4.12 Mössbauer spectra from Fe_3Si as ball-milled and after annealing for 24 hours at 450 °C.

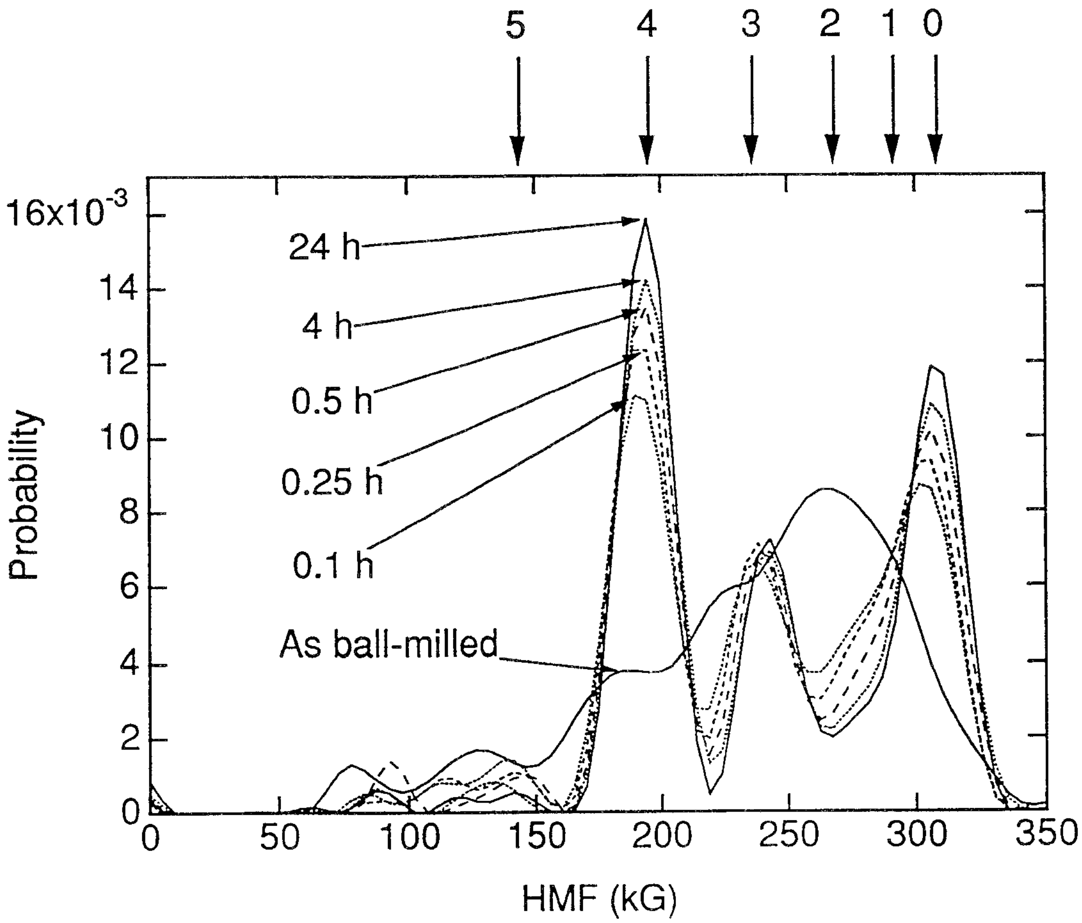

Figure 4.13 Hyperfine magnetic field distributions for Fe_3Si alloys as ball-milled, and after annealing at 450 °C for various times.

samples are presented in Figure 4.12. A series of HMF distributions extracted from Mössbauer spectra are presented in Figure 4.13. Using the method described in Section §3.3 (of Chapter 3), we can obtain the short range order parameters p(0) and p(4) from the HMF distribution peaks at approximately 190 kG and 310 kG, respectively.

Kinetic paths of short-range ordering through p(0) versus p(4) are presented in Figure 4.14 for Fe_3Si annealed at two different temperatures. The data show that the kinetic path does not depend on temperature. Furthermore, at both temperatures the kinetic paths follow the same straight line.

It is interesting to compare the present results on ordering kinetics of Fe_3Si to previous results on Fe_3Al reported in Sections §4.1 and §4.2 (Anthony and Fultz 1989a and 1989b, Fultz, Gao and Hamdeh 1990, Fultz, Gao and Anthony 1991, Fultz and Gao 1993, Gao and Fultz 1993). Both Fe_3Al and Fe_3Si have similar phase diagrams with equilibrium $D0_3$ order at low temperatures, and as solutes in bcc Fe, Al and Si atoms have many chemical similarities, being neighbors in the periodic table. For ordering in Fe_3Al, at lower annealing temperatures there is a tendency to develop excess B2 order as $D0_3$ order evolves (Anthony and Fultz 1989b; Fultz, Gao and Hamdeh 1990; Fultz, Anthony and Gao 1991). At intermediate annealing temperatures (around 300 °C), however, a transient excess of B32-type of order develops as described in Section §4.2 (Gao and Fultz 1993). These different microstructural evolutions cause clear changes in the kinetic paths of Fe_3Al with annealing temperature; typical results are presented as dotted lines in Figure 4.14. On the other hand, the kinetic paths of ordering in Fe_3Si are the same at both 350 °C and 450 °C. Furthermore, these data for Fe_3Si lie on a line that is quite straight, and close to that expected for the growth of pure $D0_3$ order without excess B2 or B32 order.

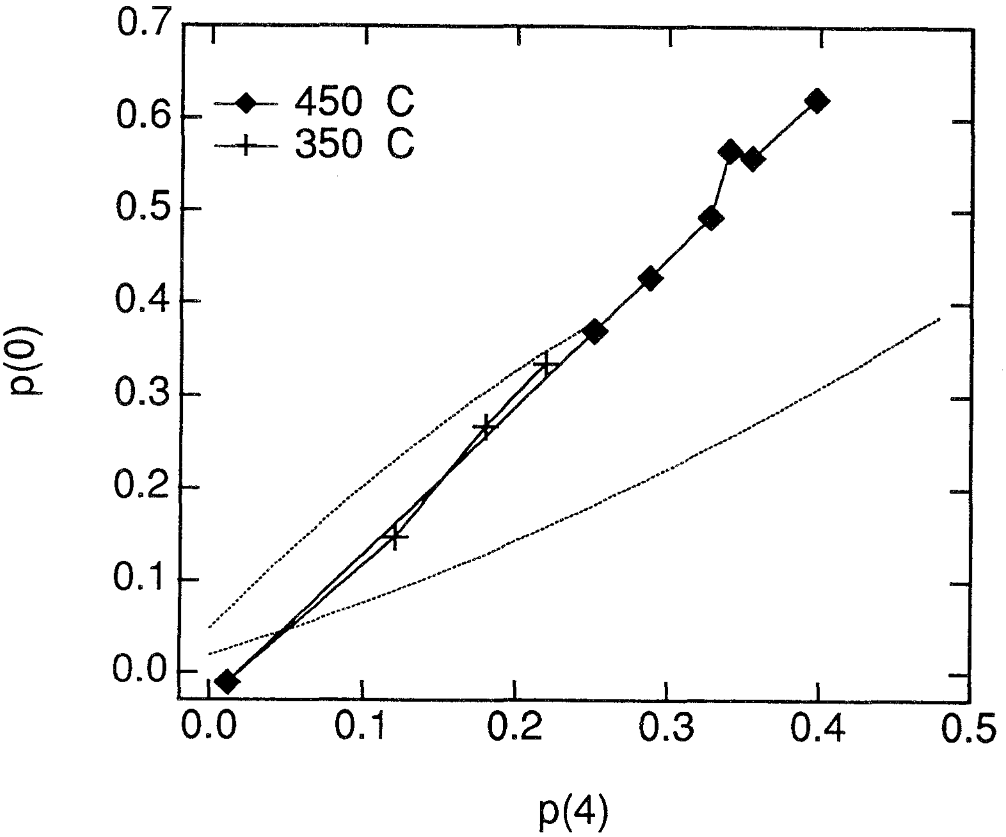

Figure 4.14 Kinetics of short range ordering in Fe_3Si (points), and Fe_3Al (dotted lines from Gao and Fultz 1993).

In studies of ordering in Fe_3Al (Fultz, Gao and Hamdeh 1990), the SRO was found to evolve with two time scales: a quick relaxation rate at the very beginning of ordering, and a slower relaxation rate that coincided with the growth of LRO. The early relaxation of SRO without LRO is consistent with homogeneous ordering, which has been studied by analytical kinetic theory and Monte Carlo simulations (Fultz 1990; Fultz 1991). If the ordering is heterogeneous, however, and occurs by nucleation and growth, then the SRO and LRO are not independent. Measured values of both the SRO and the LRO will depend on the fraction of ordered volume. All SRO parameters will be directly proportional to the amount of transformed volume, and hence proportional to each other. This is consistent with the straightness of the kinetic path in Figure 4.14. The superlattice diffraction intensity, $I^{Ex}_{\left(\frac{1}{2}\frac{1}{2}\frac{1}{2}\right)}$, will be proportional to the amount of transformed volume, but the LRO parameter is proportional to the square root of this intensity (as shown in Equation 3.1 of Chapter 3). Since our SRO parameter, p(4), and LRO parameter, L, are normalized to the range from 0 to 1, a nucleation and growth transformation will produce the parabolic kinetic path:

$$p(4) = L^2. \qquad (4.4)$$

As shown in Figure 4.15, the kinetic path for LRO versus SRO follows well the dotted parabolic curve of Equation 4.4. We therefore believe that the disorder → order transformation in Fe_3Si occurs by a heterogeneous, nucleation and growth process. Despite the thermodynamic similarities of the $D0_3$ order in Fe_3Al and Fe_3Si, their kinetic mechanisms of ordering are quite different. The difference could be because of the stronger chemical interactions for ordering in Fe_3Si than in Fe_3Al. It could also be related to the methods of preparing disordered Fe_3Al and Fe_3Si alloys. The quenched Fe_3Al samples have crystallites with dimemsion of a few microns, but

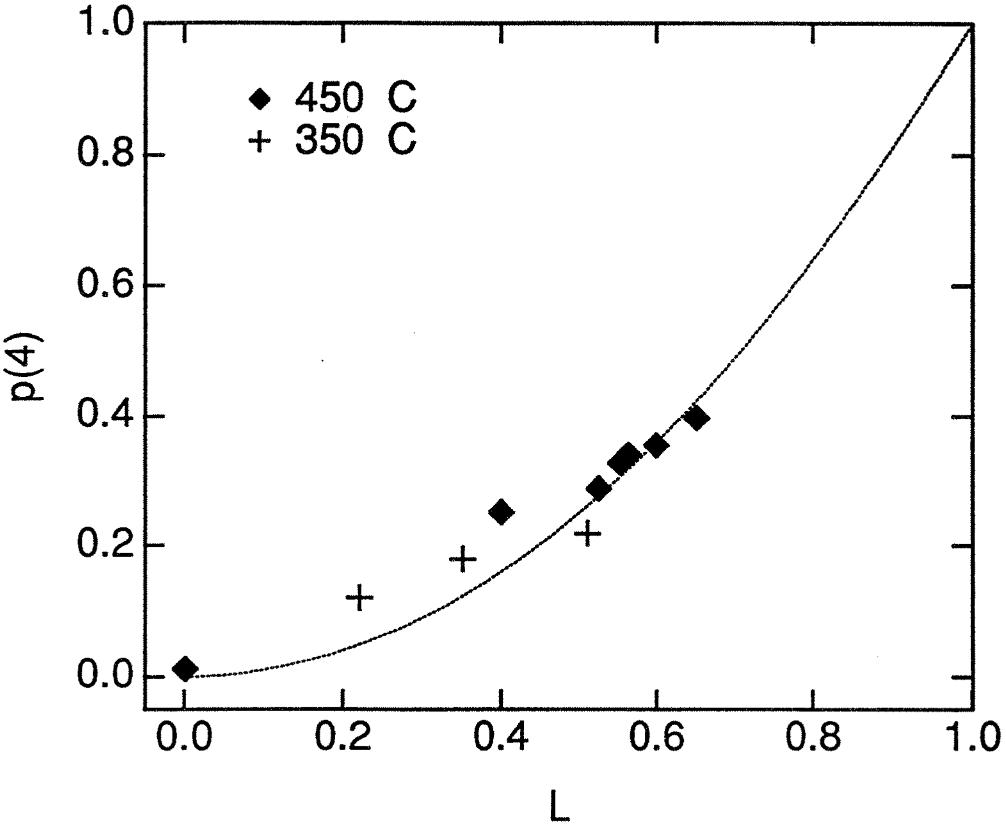

Figure 4.15 Kinetic paths of LRO vs. SRO for Fe_3Si annealed at 350 °C and 450 °C. The dotted line shows the calculated kinetic path for ordering by nucleation and growth (Equation 4.4).

the Fe_3Si samples prepared by ball-milling have crystallites of 10 nm. I do not know the reason for the difference in ordering mechanisms of Fe_3Si and Fe_3Al.

§4.4 Kinetic Paths for Fe_3Ge

Figure 4.16 shows the phase diagram for Fe-Ge. At low temperatures (up to 400 °C), the equilibrium state for Fe - 25 at.% Ge composition is a two phase mixture, while at higher temperatures it assumes an ordered closed-packed structure (fcc at temperatures below 700 °C, and hcp at temperatures above 700 °C). The large region of $D0_3$ order at low Ge compositions (up to about 20 at.% Ge), and the high critical temperature for the $D0_3$ ordered structure (up to the melting point), imply that there is a strong tendency of ordering for this alloy. Most of the previous studies on Fe_3Ge are on microstructure and magnetic properties of fcc Fe_3Ge alloys quenched from above 400 °C (Drijver, Sinnema and van de Woude 1976).

As reported previously, alloys with thermodynamic tendencies to chemically separate, for example Fe-Cu, have been synthesized as supersaturated crystalline solid solutions by ball milling (Eckert, Holzer and Johnson 1992). We hoped to use ball milling to prepare single-phase bcc Fe_3Ge at room temperature, even though this is a point in the two-phase region of the phase diagram. After 24 hours of ball milling we obtained Fe - 25 at.% Ge alloys as single phase bcc supersaturated solid solutions. The X-ray diffraction pattern for as-milled Fe - 25 at.% Ge sample is presented in Figure 4.17. An X-ray diffraction pattern from a sample annealed at 350 °C for 4 hours is also presented in Figure 4.17, and there is still no phase separation observed. (The small peaks that are seen in the X-ray diffraction pattern from the annealed sample are superlattice diffractions from the $D0_3$ ordered structure.)

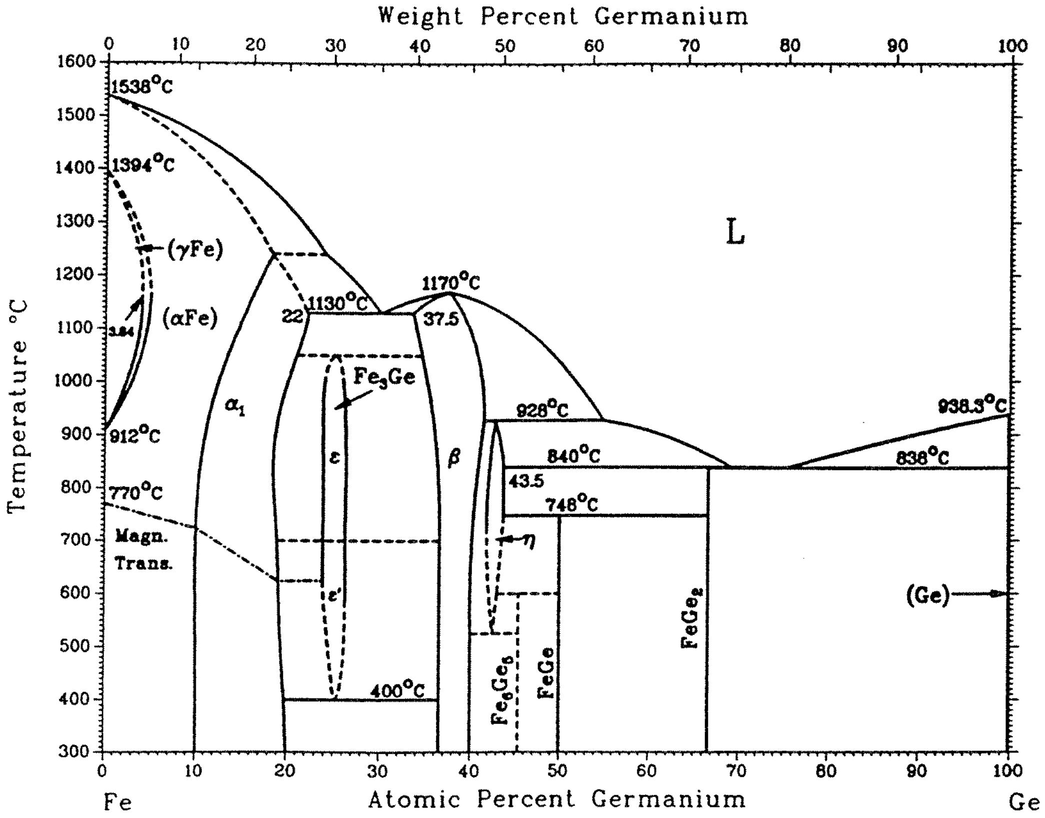

Figure 4.16 Thermodynamic equilibrium phase diagram for Fe-Ge.

(α: A2. α1: $D0_3$. ε: $D0_{19}$. ε': $L1_2$ β: $B8_1$. η: $D8_2$.)

(From Binary Alloy Phase Diagrams, edited by Massalski *et al.* 1990.)

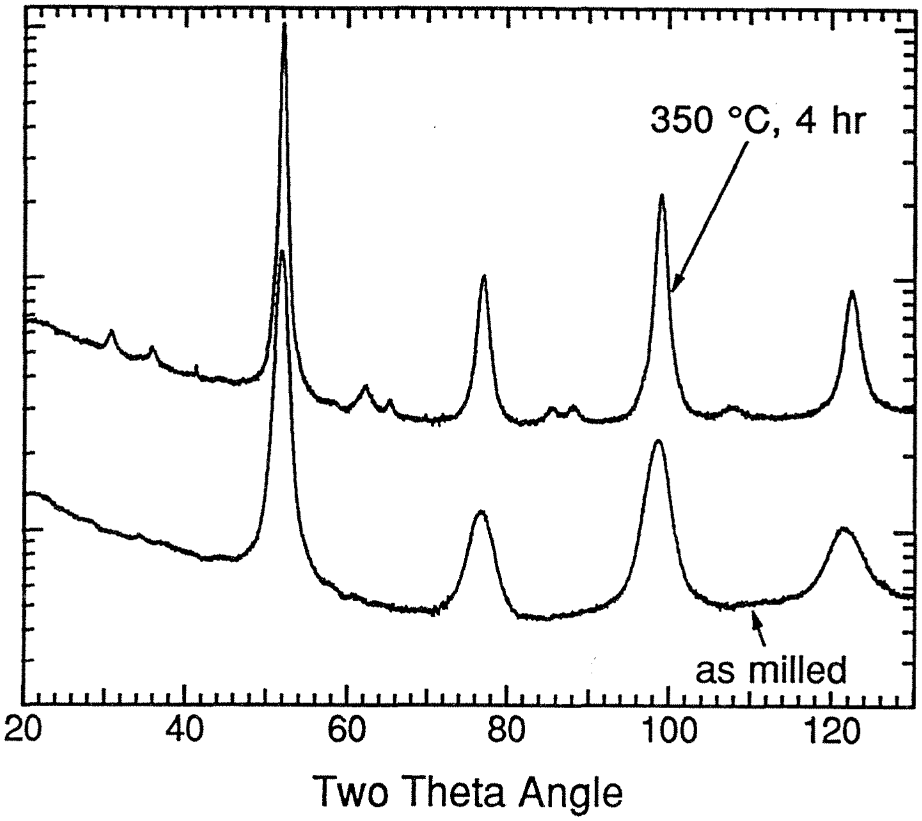

Figure 4.17 X-ray diffraction pattern for Fe_3Ge as ball-milled, and after annealing at 350 °C for 4 hours.

Two typical Mössbauer spectra are presented in Figure 4.18. The HMF distributions extracted from the Mössbauer spectra are shown in Figures 4.19 to 4.21 for three different annealing temperatures: 250 °C, 300 °C and 350 °C. At all these three temperatures, $D0_3$ order developed.

Using the method described in Section §3.3, we can obtain SRO parameters, p(0) and p(4). The kinetic paths of short range ordering are presented in Figure 4.22 for all three annealing temperatures. Just as was the case for Fe_3Si, there is no clear temperature dependence of the kinetic paths for Fe_3Ge. Figure 4.22 shows that the kinetic paths of SRO in Fe_3Ge follow accurately the same straight line at three temperatures. As argued in Section §4.3 for Fe_3Si, I believe this shows the $D0_3$ structure evolves in Fe_3Ge by nucleation and growth from the disordered A2 structure.

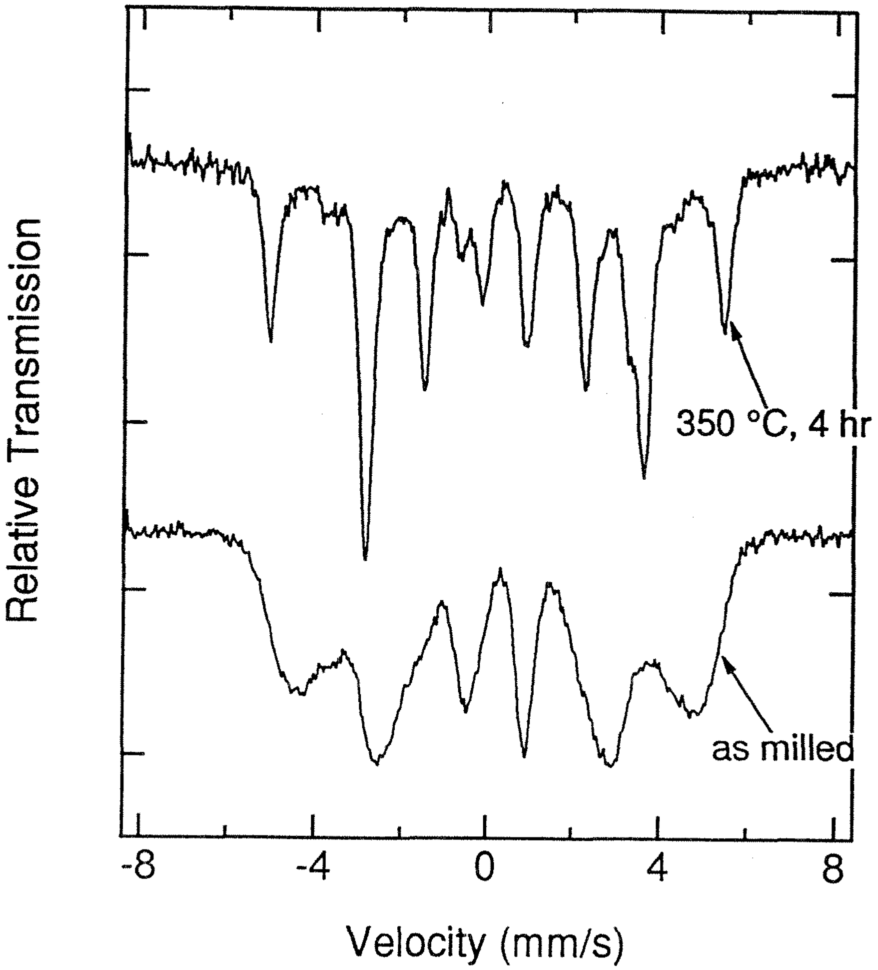

Figure 4.18 Mössbauer spectra for Fe_3Ge as ball-milled, and after annealing at 350 °C for 4 hours.

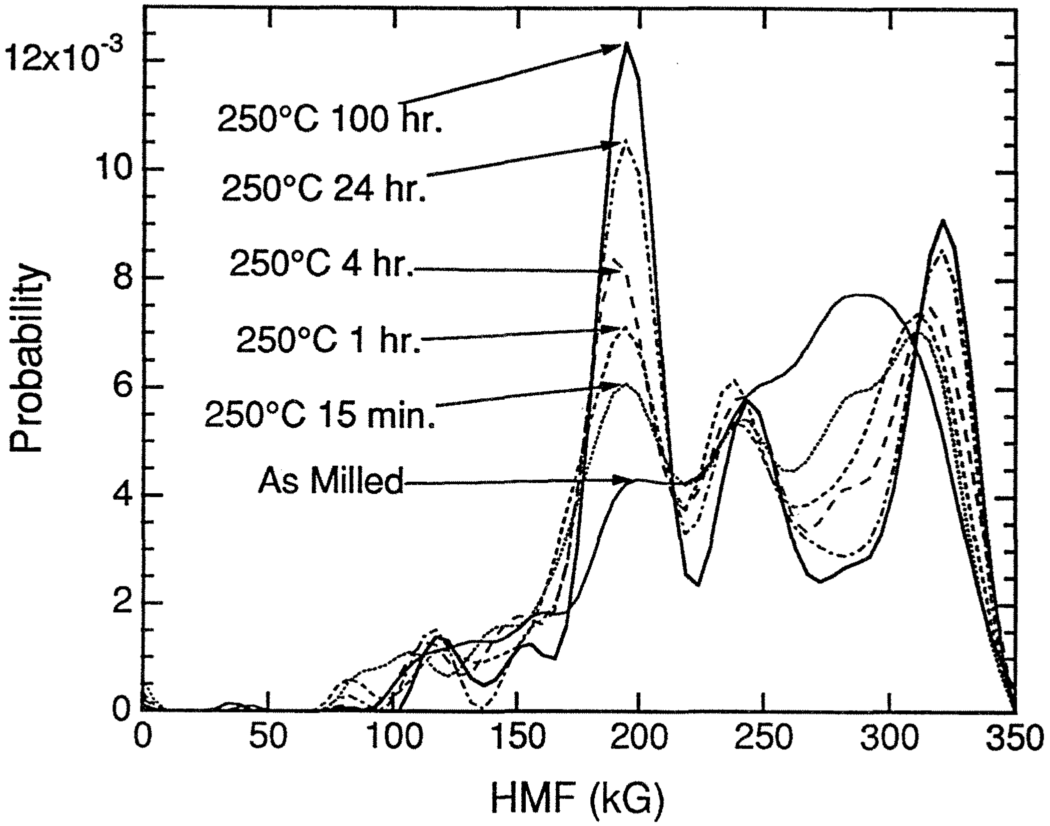

Figure 4.19 Hyperfine magnetic field distribution for Fe_3Ge alloy as ball-milled, and after annealing at 250 °C for various times.

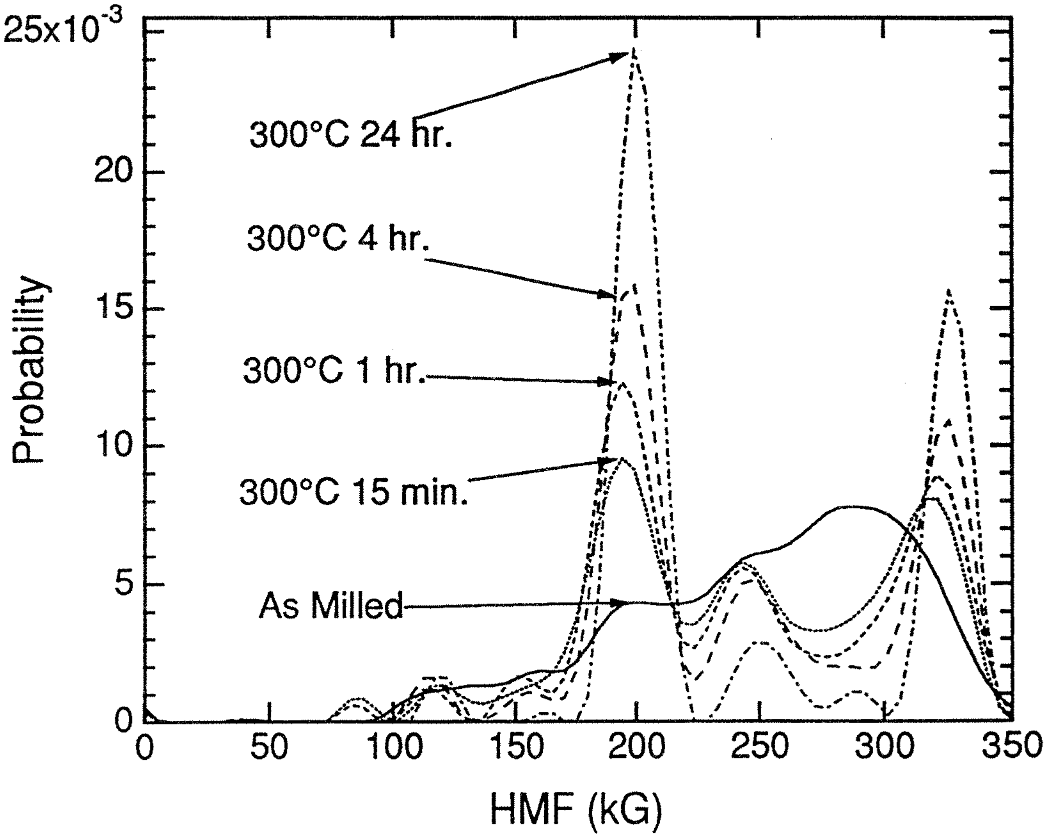

Figure 4.20 Hyperfine magnetic field distribution for Fe_3Ge alloy as ball-milled, and after annealing at 300 °C for various times.

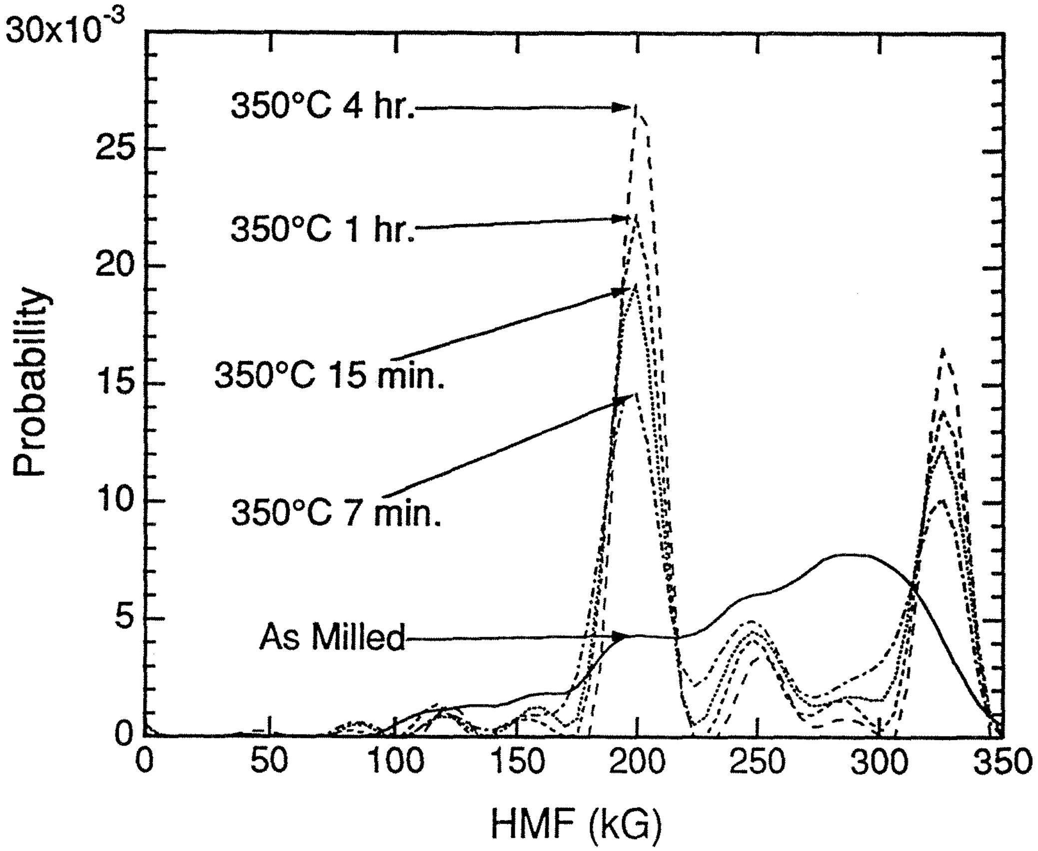

Figure 4.21 Hyperfine magnetic field distribution for Fe_3Ge alloy as ball-milled, and after annealing at 350 °C for various times.

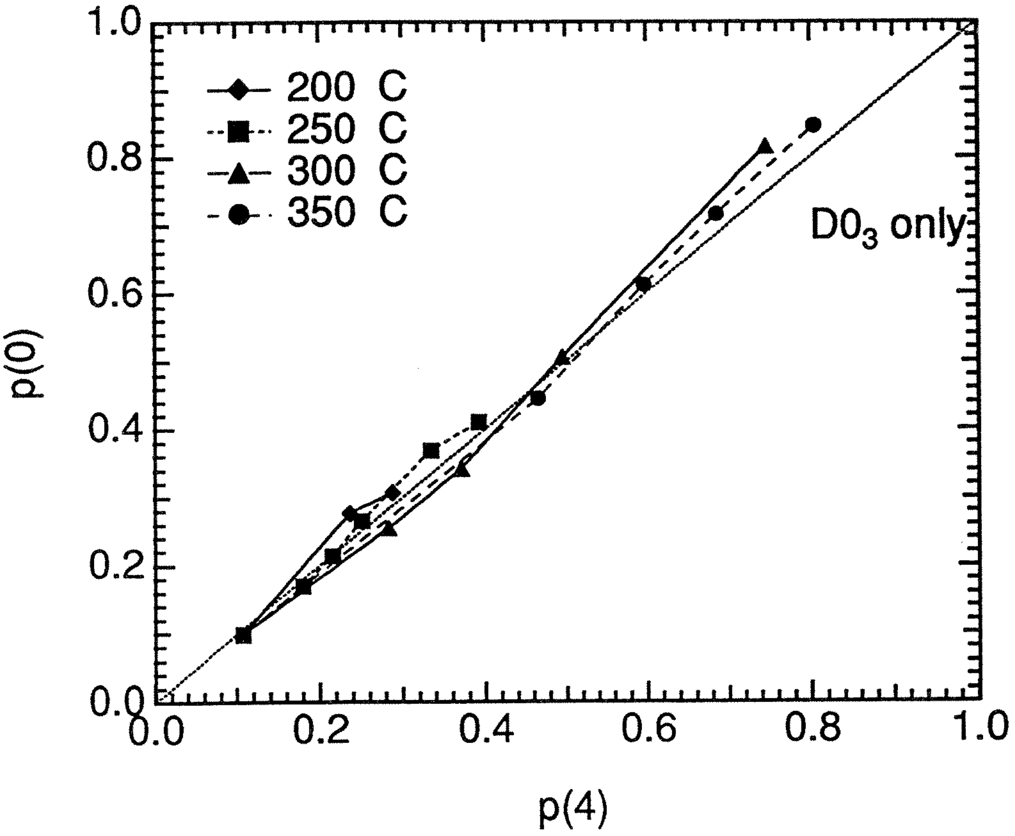

Figure 4.22 Kinetic paths of short range ordering in Fe_3Ge. The dotted line was calculated by assuming the growth of D0$_3$ order only.

References

ALLEN, S. M., and CAHN, J. W., *Acta Metall.* **20**, 423 (1972).

ANTHONY, L.: Ph.D. Thesis, California Institute of Technology, (1993).

ANTHONY, L. and FULTZ, B.: *J. Mater. Res.* **4**, 1132 (1989a). *ibid.*, **4**, 1140 (1989b).

ANTHONY, L. and FULTZ, B.: *Mater. Res. Soc. Symp. Proc.* **186**, 181 (1991).

ANTHONY, L. and FULTZ, B.: *J. Mater. Res.*, **9**, 348 (1994).

DRIJVER, J. W.; SINNEMA, S. G. and VAN DE WOUDE, F.: *J. Phys.*, **F 6**, 2165 (1976).

ECKERT, J.; HOLZER, J. C. and JOHNSON, W. L.: J. *Mater. Res.;* **7**, 1751 (1992).

FULTZ, B.; GAO, Z. Q. and HAMDEH, H. H.: *Hyperfine Interact.* **54**, 799 (1990).

FULTZ, B., *J. Mater. Res.*, **5**, 1419 (1990).

FULTZ, B., *Phys. Rev.*, **B 44**, 9805 (1991).

FULTZ, B.; GAO, Z. Q. and ANTHONY, L.: *Mater. Res. Soc. Symp. Proc.* **186**, 187 (1991).

FULTZ, B. and GAO, Z. Q.,: *Nucl. Instr. and Methods, Phys. Res.*, **B 76**, 115 (1993).

GAO, Z. Q. and FULTZ, B., *Phil. Mag.*, **B 67**, 787 (1993).

LE CAËR, G. and DUBOIS, J. M.: *J. Phys.* **E 12**, 1083 (1979).

MARCINKOWSKI, M. J. and BROWN, N.: *J. Appl. Phys.*, **33**, 537 (1962).

OKAMOTO, H. and BECK, P. A.: *Metall. Trans.* **2**, 569 (1971).

OKI, K.; HASAKA, M. and EGUCHI, T.: *Japan J. Appl. Phys.* **12**, 1522 (1973).

OKI, K.; HASAKA, M. and EGUCHI, T.: Trans. *JIM* **15**, 143 (1974).

PARK, B.; STEPHENSON, G. B.; ALLEN, S. M. and LUDWIG, K. F.: *Phys. Rev. Lett.* **68**, 1742 (1992).

RICHARDS, M. J., and CAHN, J. W., *Acta Metall.* **19**, 1263 (1971).

ROTELLA, F. J., 1983, "User *Manual for Rietveld Analysis of Time-of-Flight Neutron Powder Diffraction Data at IPNS".*

SCHWEIKA, W.: Materials Research Society Symposium Proceedings, Vol. 166, (Pittsburgh, Pennsylvania: Materials Research Society, 1990), p. 249.

SWANN, P. R.; DUFF, W. R. and FISHER, R. M.: *Trans. AIME* **245**, 851 (1969).

WARREN, B. E.: X-Ray Diffraction, (Addison-Wesley, Reading, Mass., 1969), Chapter 12.

Chapter 5 Inter-Dependence of Grain Growth, Nb Segregation and Chemical Ordering in Fe_3Si-Nb Nanocrystalline Materials

In this chapter I will first briefly introduce some features of nanocrystalline materials. To emphasize the importance of keeping the grain size small, in the second section I will discuss the effect of grain size on the magnetic soft magnetic properties of nanocrystalline materials. Then in Sections §5.3 to §5.5 I will discuss our studies on the thermal stability of Fe_3Si and $(Fe_3Si)_{0.95}Nb_{0.05}$ alloy. The results on the inter-dependency of chemical ordering, chemical decomposition and grain growth processes in the nanocrystalline Fe_3Si-Nb alloy will be summarized in the final section.

§5.1 Introduction to Nanocrystalline Materials

Nanocrystalline materials are polycrystalline materials with grain size on the order of nanometers (typically < 100 nm). As depicted schematically in Figure 5.1, because of the small grain size a large fraction of the atoms in nanocrystalline materials are located at incoherent interfaces between crystalline grains of different orientations.

Unique properties of nanocrystalline materials can be obtained from two features of their microstructures: their small grain size or their large percentage of

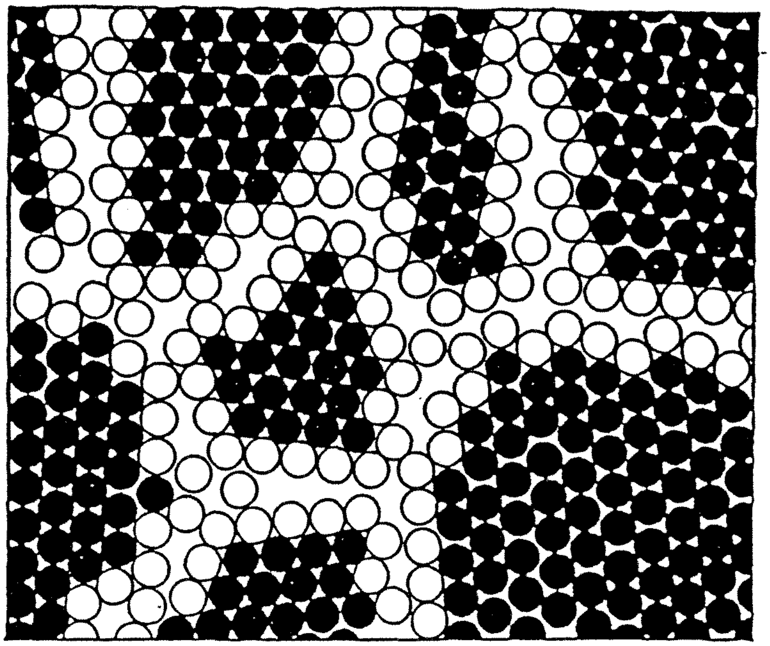

Figure 5.1 Schematic of atomic structure of a two-dimensional nanocrystalline material. The atoms in the center of crystallites are indicated in black, and the atoms in boundaries are represented by open circles. (From Gleiter 1989).

atoms at grain boundaries. One famous example is the effect of grain size on mechanical flow strength, σ, which at large grain size is commonly described with the Hall-Petch relation: $\sigma \propto d^{-1/2}$ (Lasalmonie and Strudel 1986), where d is the grain size. Most models used to interpret this phenomenological relationship are based on dislocation theory. The grain boundaries may either act as obstacles to dislocation slip (strengthening affect) or provide a positive contribution to the deformation of the material (softening effect). As the grain size falls to a few nanometers, the nanocrystalline materials may be free of dislocations (Trudeau and Schulz 1991), so the deformation behavior may not be controlled by dislocation movement. Perhaps a diffusion controlled deformation mechanism, related to the large density of grain boundaries, predominates at small grain size. Such a change in mechanism can provide improved mechanical properties such as ductility for ceramic nanocrystalline materials (Siegel 1991).

The small grain dimensions can control properties of nanocrystalline materials, and a good example is found in superparamagnetic phenomenon (Jorra, Franz, Peisl, Wallner, Petry, Birringer, Gleiter and Haubold 1989). As reported recently, the superior soft magnetic properties of Fe-Si based magnetic materials (Yoshizawa, Oguma and Yamauchi 1988) are also attributed to the small crystallite size, as described in Section §5.2.

Synthesis of Nanocrystalline Materials

Nanocrystalline materials first attracted international attention when they were prepared by using the gas condensation method (Gleiter 1989). Since then, many methods were developed to synthesis nanocrystalline materials. Besides the gas condensation method, the most frequently used methods include mechanical attrition or ball milling (Koch 1993), crystallization of amorphous alloys (Yashizawa, Oguma and Yamauchi 1988), sol-gel reactions, laser ablation, electric field methods, physical vapor deposition and wet chemistry precipitation.

Thermal Stability of Nanocrystalline Materials

All polycrystalline materials, especially nanocrystalline materials with grain sizes below 100 nm, tend to undergo grain growth to reduce the excess energy associated with grain boundaries. Polycrystals of either pure elements or alloys will undergo grain growth, but alloys may have additional types of instabilities. Alloys with thermodynamic tendencies to chemically decompose have been synthesized by high energy ball milling as supersaturated crystalline solid solutions, for example Cr-Fe (Kuwano, Ouyang and Fultz 1992), Fe-Cu (Eckert, Holzer and Johnson 1992), Ni-Mo (Trudeau and Schultz 1991) and Zr-Al (Fecht, Han, Fu and Johnson 1990). These alloys are unstable against chemical segregation. Alternatively, alloys with thermodynamic tendencies to develop chemical order have been prepared as disordered solid solutions by the gas condensation method or high energy ball milling, for example Ni_3Al (Haubold, Bohn, Birringer and Gleiter 1992; Jang and Koch 1990), Au-Cu (Kaito and Shiojiri 1982), FeV (Fultz, Le Caër and Matteazzi 1989), SiRu and AlRu (Hellstern, Fecht and Johnson 1989). These alloys are unstable against chemical ordering. [During mechanical attrition, alloys with larger enthalpies of ordering tend to become amorphous after they are chemically disordered, as found in early work with Co-Y (Yermakov, Yurchinko and Barinov 1981) and Ni-Nb (Koch, Cavin, McKamey and Scarborough 1983), and more recently with the gas condensation method, for example with Ni-Ti (Averback, Hahn, Höfler and Logas 1990) and TiAl (Chang, Höfler, Altstetter and Averback 1991).]

There have been a number of observations on the stability of nanophase materials against grain growth (Gleiter 1989; Hahn, Logas and Averback 1990;

Siegel, Ramasamy, Hahn, Li, Lu and Gronsky 1988; Eastman and Siegel 1989; Eckert, Holzer and Johnson 1993) but a better understanding of the thermodynamic and kinetic aspects of stability is needed. It is important to ask if the thermodynamic instability against grain growth could be linked to an instability against chemical ordering, or an instability against chemical decomposition. If so, control of the state of chemical order or chemical segregation may be useful for controlling the stability against grain growth. Weissmüller (Weissmüller 1993; Weissmüller 1994), following Johnson (Johnson, private commun.), has suggested that in nanophase alloys with strongly positive heats of mixing (decomposing alloys) it may be possible for chemical segregation to grain boundaries to stabilize the alloy against grain growth. In this picture, grain growth would eliminate grain boundaries, forcing re-solution of the segregant, which is energetically unfavorable.

In nanophase alloys with strongly negative heats of mixing (ordering alloys), an initial state of chemical disorder may help stabilize nanoscale grains for thermodynamic reasons. Alloys with grain sizes of 4 nm have a high fraction of atoms inside and near grain boundaries [40 % for fcc alloys, 50-60% for bcc alloys (Kuwano, Ouyang and Fultz 1992)]. Perhaps these grain boundary atoms can be more favorably situated when the adjacent crystals are disordered chemically — the atoms at grain boundaries would have more freedom to satisfy their chemical preferences for short range order (SRO) if the grains around them did not have long range order (LRO). Only a little experimental evidence is available to test this thermodynamic idea. Grain boundaries in ordered Ni_3Al are chemically disordered (Baker and Schulson 1989; Schulson and Baker 1991). For disordered nanophase Ni_3Al, it has been observed that grain growth and ordering occur at about the same annealing temperature (Harris, Pearson, Garland and Fultz 1991; Bohn, Haubold, Birringer and Gleiter 1991), and it has also been observed that under pressure the temperatures for ordering and grain growth both increased by about the same amounts (Haubold, Bohn, Birringer and Gleiter 1992). A thermodynamic inter-dependence of ordering and grain growth is consistent with these results, although it is not proved. An alternative kinetic explanation is possible. Grain growth and ordering could be independent processes that occur together only because they both depend on diffusivity. It seems doubtful, however, that grain growth and ordering would then exhibit the same pressure and temperature dependence because ordering depends on bulk diffusion, and grain growth should depend more on grain boundary diffusion.

§5.2 Effect of Grain Size on Soft Magnetic Properties

Recently it has been reported (Yoshizawa, Oguma and Yamauchi 1988) that a nanocrystalline Fe-Si-B-Cu-Nb alloy, prepared by partial crystallization of an amorphous alloy, exhibits low magnetic anisotropy while maintaining a high saturation flux density. The alloy, known as “Finemet," is prepared first by a rapid quench to an amorphous state, followed by an annealing to precipitate nanocrystallites of Fe-Si. Boron enhances the glass-forming ability, the copper promotes the formation of bcc crystallites from the amorphous phase, and the niobium suppresses crystal grain growth (Yoshizawa and Yamauchi 1991; Hampel, Pundt and Hesse 1992).

Before starting to discuss how to stabilize the grain size of nanocrystalline materials, I first reiterate the importance of stabilizing a fine grain size by discussing the grain size dependence of soft magnetic properties in Fe-Si. Such a dependency is correlated closely with the counterplay of local magneto-crystalline anisotropy energy and the ferromagnetic exchange interaction (Herzer 1991).

Within large grains, the magnetizations follow the local easy magnetic directions, and the magnetization process is determined by the magneto-crystalline anisotropy, K_1, of the crystallites. If the grain size is very small, however, the ferromagnetic exchange interaction increasingly forces the magnetic moments to align parallel, thus impeding the magnetization from following the easy directions of each individual grain. As a result, the effective anisotropy is an average over several grains. The dividing line between these two cases is given by the ferromagnetic exchange length

$$L_{ex}{}^0 = (A / K_1)^{1/2}, \tag{5.1}$$

where A denotes the exchange stiffness. (The ferromagnetic exchange length is a basic parameter in domain wall theory representing a characteristic minimum scale over which the magnetization can vary appreciably (Chen 1986).)

Random Anisotropy Model

The degree to which the magneto-crystalline anisotropy is averaged out can be estimated quantitatively with a random anisotropy model. This model was originally proposed by Alben *et al.* (Alben, Becker and Chi 1978) for amorphous ferromagnets. Figure 5.2 shows schematically the idea of this model.

For an assembly of ferromagnetically coupled grains of size D ($D < L_{ex}$) with randomly oriented magneto-crystalline anisotropies K_1, the average anisotropy, $<K>$, is:

$$\langle K \rangle = \frac{K_1}{\sqrt{N}} = \frac{K_1}{(L_{ex} / D)^{3/2}}, \tag{5.2}$$

where N is the number of crystallites within the distance of L_{ex}. With L_{ex} = (A /

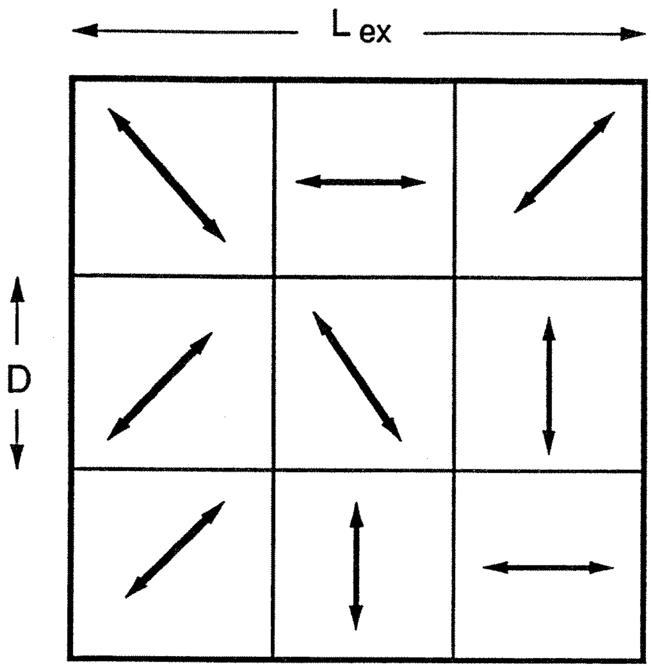

$$N=\left(\frac{L_{ex}}{D}\right)^3$$

Figure 5.2 Schematic of the random anisotropy model. The arrows indicate the randomly fluctuating magneto-crystalline anisotropies. (From Herzer 1991).

$<K>)^{1/2}$, Equation (5.2) becomes:

$$\langle K\rangle = \frac{K_1^4 D^6}{A^3}. \tag{5.3}$$

The coercivity is closely correlated to the average anisotropy $<K>$ by:

$$H_C = p_C \frac{\langle K\rangle}{M_S} \approx p_C \frac{K_1^4 D^6}{M_S A^3}, \tag{5.4}$$

where M_S is the saturation magnetization and p_C is a dimensionless pre-factor close to unity (Herzer 1990). From Equation (5.4), we find that as D gets smaller, so does H_C, and the material gets magnetically "*softer.*"

For binary Fe_3Si, $K_1 \approx 6$ kJ m^{-3} (Gengnagel and Wagner 1961) and $A \approx 10^{-11}$ J m^{-1} (Hüller 1986), so the exchange correlation length can be estimated as $L_{ex} \approx 40$ nm. Figure 5.3 shows a theoretical estimate of the average anisotropy $<K>$ for randomly oriented bcc Fe_3Si as a function of grain size, D.

Structure and Magnetic Properties of Nanocrystalline Fe-Ge Thin Films

Here I discuss some results from a study on sputtered thin films of $Fe_{0.79}Ge_{0.21}$ (Hamdeh, Oliver, Fultz and Gao 1993). These results give support to the random anisotropy model.

The $Fe_{0.79}Ge_{0.21}$ thin film samples were prepared by ion beam sputtering to a thickness about 280 nm. The as-prepared films were bcc disordered polycrystals, as confirmed by X-ray diffractometry. The films were then annealed at progressively higher temperature for 15 minutes. Figure 5.4 shows the changes of grain size and mean-square strain obtained from widths of the X-ray diffraction peaks versus annealing temperatures. The magnetic properties, coercivity and saturation

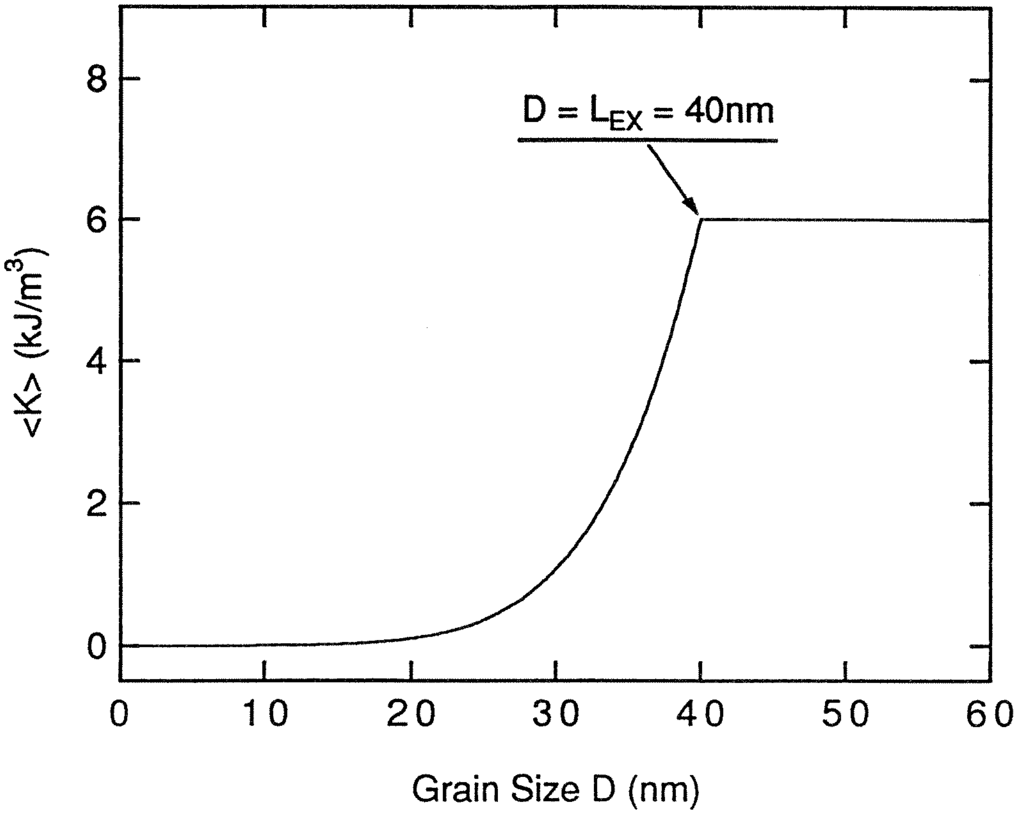

Figure 5.3 Theoretical estimate of the average anisotropy, <K>, for Fe_3Si as a function of grain size D. (Recalculated after Herzer 1991).

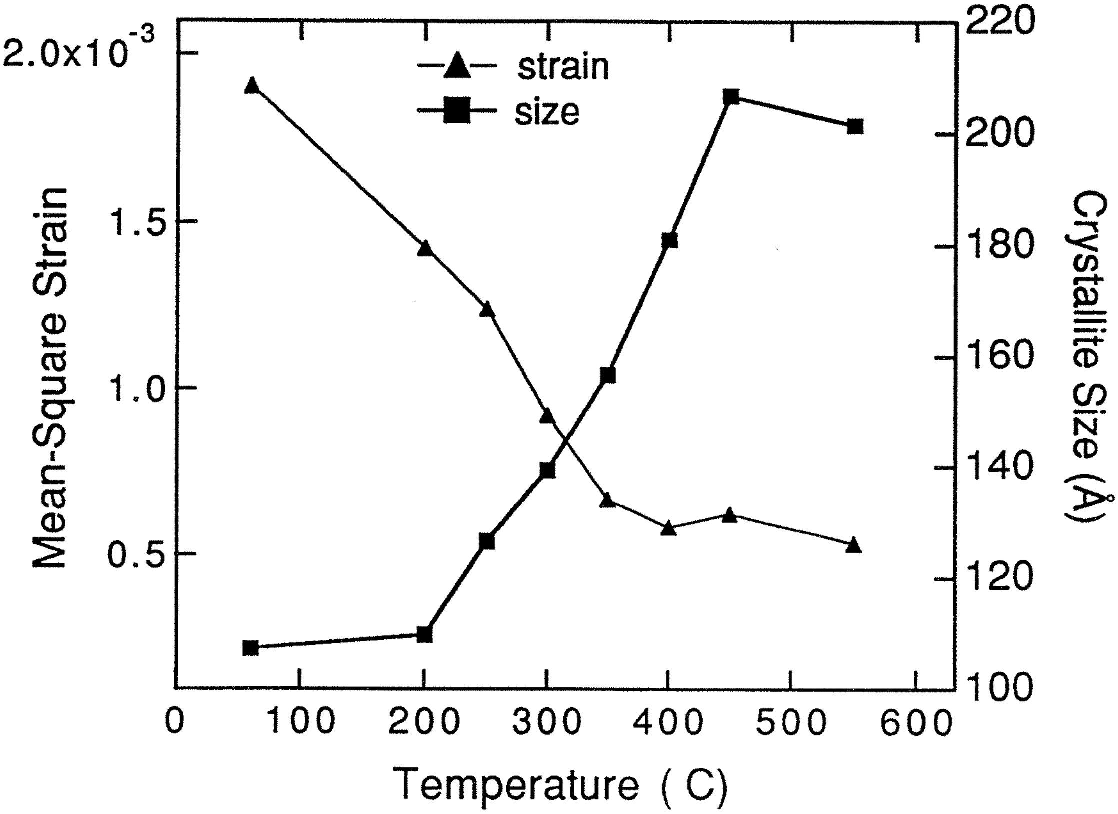

Figure 5.4 Mean-square strain and grain size for Fe_3Ge thin film versus annealing temperature, obtained from widths of the X-ray diffraction peaks.

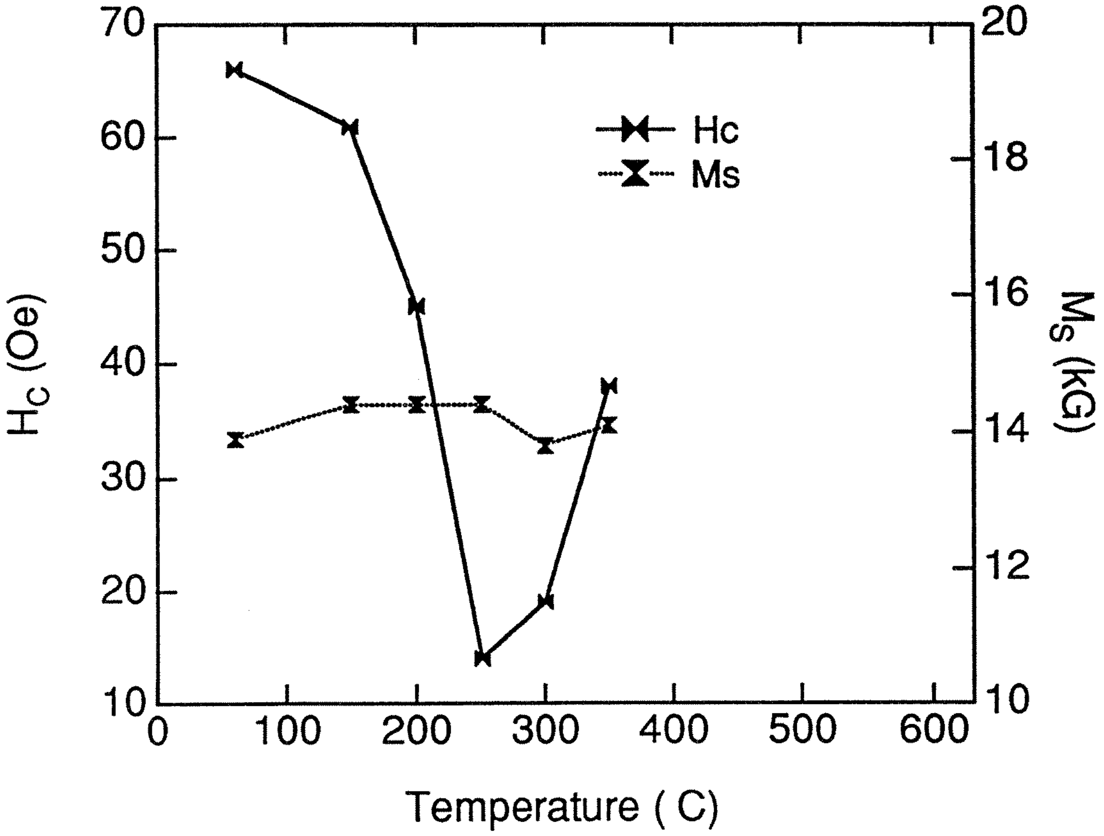

Figure 5.5 Coercivity (H_C) and saturation magnetization (M_S) for Fe_3Ge thin films versus annealing temperature.

magnetization of the films are presented in Figure 5.5. While the saturation magnetization does not change significantly, the coercivity drops rapidly after annealing at low temperatures, corresponding to a rapid decrease in mean-square strain. It is reasonable that as the internal strains in the material are relieved, the coercivity decreases. At annealing temperatures higher than 250 °C, the coercivity reverses its course and increases rapidly. This increase can be attributed to the significant increase in grain size that, upon above certain level, has a dominant effect on the soft magnetic properties. Since I did not find K_1 and A data to estimate the exchange correlation length L_{ex} for Fe-Ge, I expect it to be about same as Fe_3Si. As the average grain size grows to about 15 nm, roughly one third to a half of the L_{ex}, the coercivity starts to increase rapidly.

Using mechanical alloying, nanocrystalline Fe-Si based alloys can be synthesized directly from elemental powders (Escorial, Adeva, Cristina, Martin, Carmona, Cebollada, Martin, Leonato and Gonzalez 1991; Li, Birringer, Johnson and Shull 1993), obviating the need for boron and copper as in the Finemet. As for Fe-Ge alloys, the stability of Fe-Si alloys against grain growth is generally not sufficient to withstand annealings for stress relaxation, which may be needed for good magnetic properties (Kuhrt and Schultz 1992). In my thesis research work the effects of niobium on the stability against grain growth and ordering of nanophase Fe-Si prepared by mechanical attrition were studied.

§5.3 Grain Growth in $(Fe_3Si)_{.95}Nb_{.05}$ Prepared by Ball Milling

Figure 5.6 presents bright field and dark field TEM micrographs and diffraction patterns from the $(Fe_3Si)_{.95}Nb_{.05}$ alloy after 48 hours ball-milling

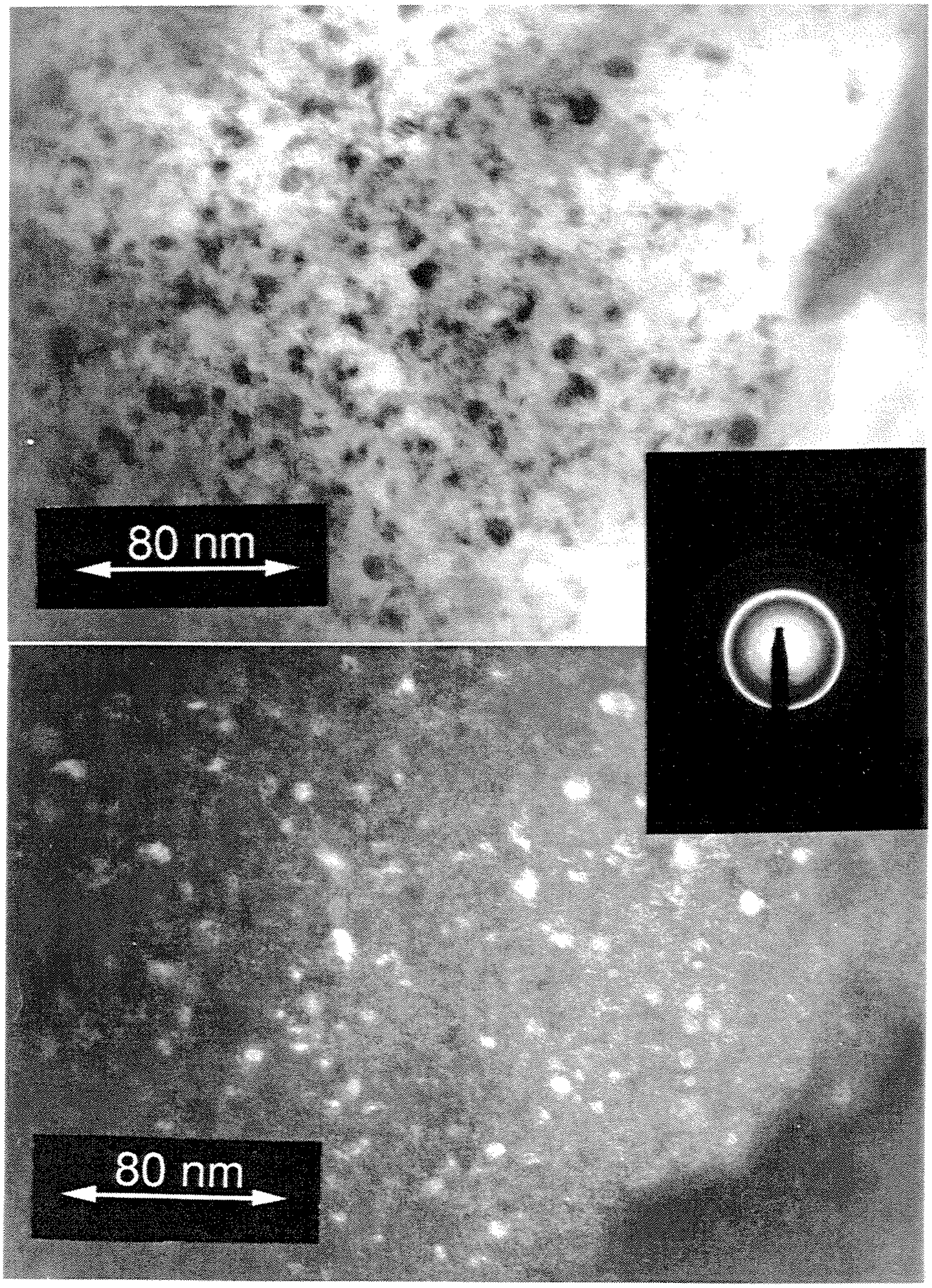

Figure 5.6 TEM bright field image, dark field image and diffraction pattern from an $(Fe_3Si)_{0.95}Nb_{0.05}$ after annealed at 450 °C for 24 hours.

followed by 24 hours of annealing at 450 °C. The grains seen in the dark-field image are mostly less than 10 nm, and a modest size distribution is evident.

X-ray diffractometry was our routine tool to determine the grain size. Our goal was not precise grain size measurements, but rather a comparison of grain growth of the ternary $(Fe_3Si)_{.95}Nb_{.05}$ alloy and the binary Fe_3Si alloy. After background determination, a Lorentzian function was fit to each diffraction peak. Using the width of the Lorentzian function, a simple Scherrer line broadening analysis was performed on the (110), (211), and (222) diffraction peaks to determine the grain size. There was not a large difference in the grain sizes from these three different peaks, indicating that strain broadening was not severe, but the (200) diffraction was noticeably broader and always gave a smaller grain size. Figure 5.7 shows the grain growth determined from the (110) diffraction peak after annealing at 450 °C for different times. For the ternary $(Fe_3Si)_{.95}Nb_{.05}$ alloy the grains grew slightly and stabilized at about 10 nm, approximately consistent with the TEM observations. For the binary Fe_3Si alloy without niobium, the grain size doubled quickly to about 20 nm after the same annealing time of about an hour.

§5.4 Mössbauer Data Analysis

Mössbauer Data Analysis for SRO — HMF

Representative Mössbauer spectra are presented in Figure 5.8. These spectra were analyzed by the method of Le Caër and Dubois (Le Caër and Dubois 1979) as a sum of overlapping ferromagnetic sextets (see Section §3.3). A set of HMF distributions from an annealing sequence is presented in Figure 5.9. The most prominent features in this sequence of HMF distributions are the two growing peaks

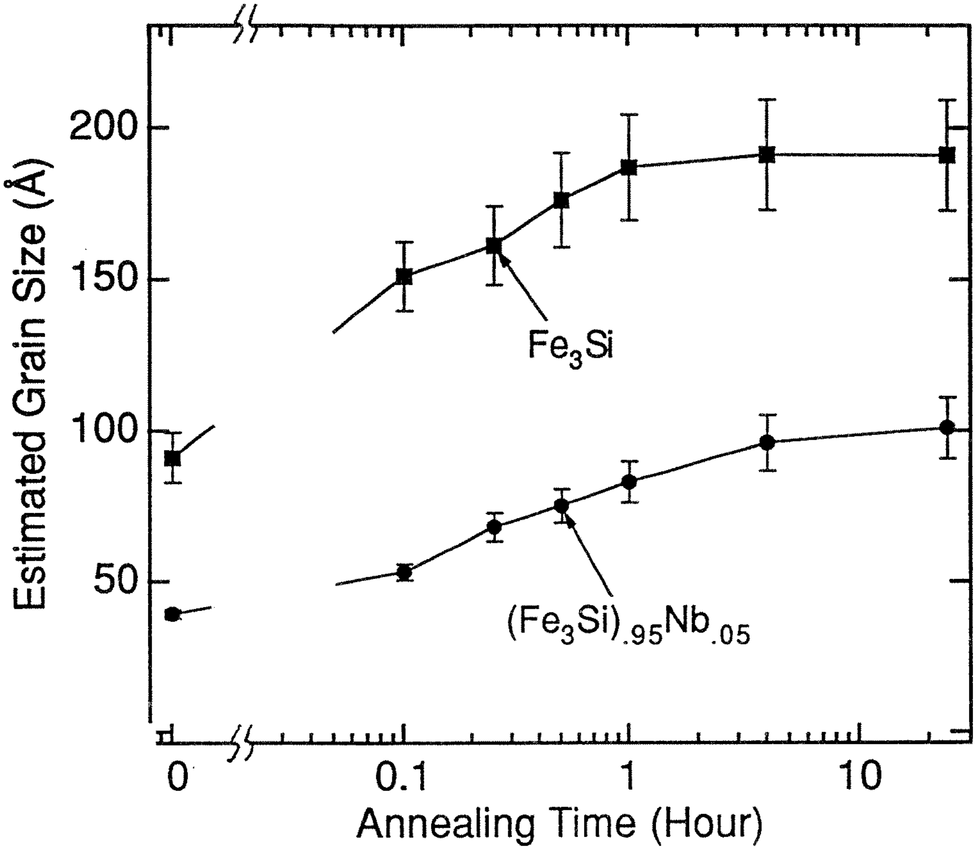

Figure 5.7 Grain growth of $(Fe_3Si)_{0.95}Nb_{0.05}$ and Fe_3Si at 450 °C.

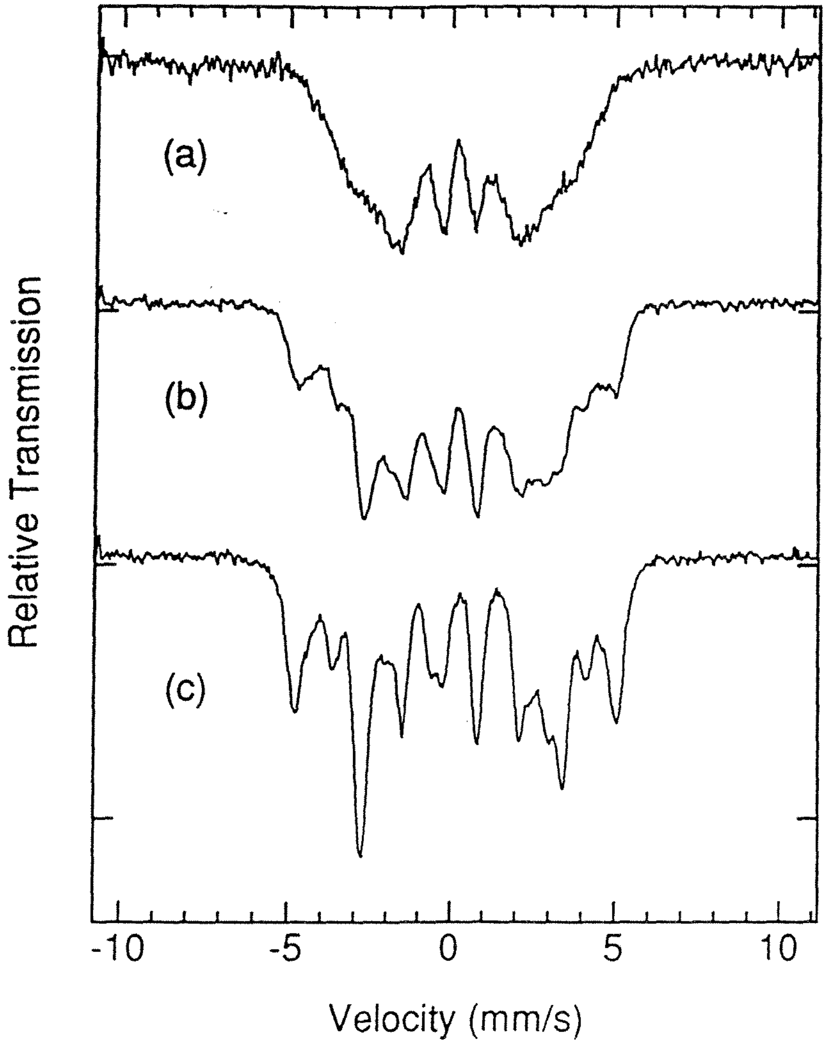

Figure 5.8 Typical Mössbauer spectra of $(Fe_3Si)_{0.95}Nb_{0.05}$ (a) as ball-milled; (b) annealed at 450 °C for 15 minutes; (c) annealed at 450 °C for 4 hours.

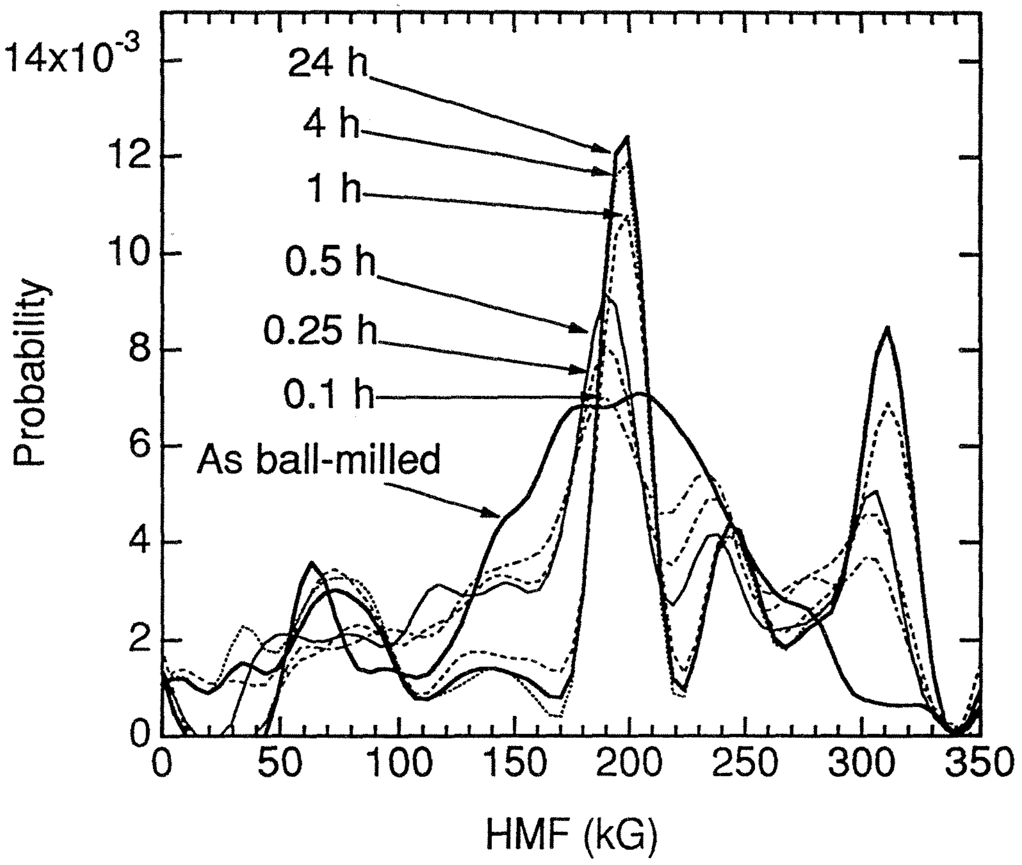

Figure 5.9 Hyperfine magnetic field distributions for $(Fe_3Si)_{0.95}Nb_{0.05}$ alloys as ball-milled, and after annealing at 450 °C for various times.

at about 197 kG and 313 kG. As discussed in chapter 4, these two peaks originate from the two different sites for iron atoms in the D0$_3$-ordered structure. The peak at 313 kG is from iron atoms with zero (0) silicon atoms as first-nearest neighbors, and the peak at 197 kG is from iron atoms with four (4) silicon atoms as first-nearest neighbors. The growth of these two peaks indicates the formation of D0$_3$ order, and order parameters can be determined from their intensities (Equation 3.7). The development of SRO for both Fe$_3$Si and (Fe$_3$Si)$_{.95}$Nb$_{.05}$ is presented in Figure 5.10. The D0$_3$ order has started to develop after the first 30 minutes of annealing. In the binary Fe$_3$Si alloy the initial growth of these two peaks is at precisely 197 kG and 313 kG. In the ternary (Fe$_3$Si)$_{.95}$Nb$_{.05}$ alloy annealed for 30 minutes or less, however, initially these two peaks are shifted downwards by about 10 kG (Figure 5.9). As discussed below, this shift is caused by the niobium atoms, which reduce the ^{57}Fe HMF when they are in the first or second nearest neighbor shells of an ^{57}Fe atom.

The $(\frac{1}{2}\frac{1}{2}\frac{1}{2})$ superlattice diffraction peak is characteristic of the D0$_3$-ordered structure. We used the square-root of the $(\frac{1}{2}\frac{1}{2}\frac{1}{2})$ diffraction peak intensity, normalized by the (110) diffraction peak intensity, as an LRO parameter, as described in Section §3.2. Semi-quantitatively, the development of LRO for Fe$_3$Si with and without the niobium ternary component is also presented in Figure 5.10. For both LRO and SRO, the evolution of order in the ternary (Fe$_3$Si)$_{.95}$Nb$_{.05}$ alloy lags behind that of the binary Fe$_3$Si alloy during the first hour or so of annealing.

Mössbauer Data Analysis for Nb—HMF

To the best of our knowledge, the local ^{57}Fe HMF and IS perturbations caused by Nb neighbors in bcc Fe or Fe-Si alloys have never been measured. Based on the systematics of solutes in bcc iron alloys, described in Section §2.3, a Nb

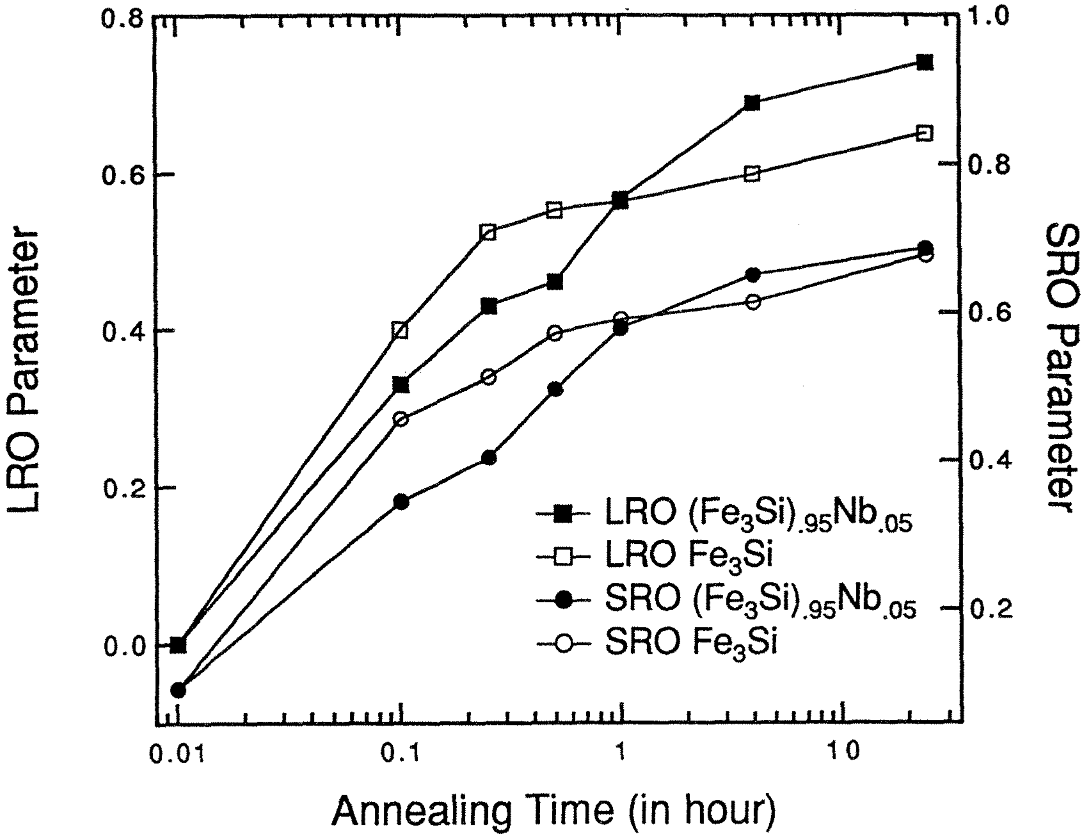

Figure 5.10 Ordering kinetics for $(Fe_3Si)_{0.95}Nb_{0.05}$ and Fe_3Si at 450 °C.

concentration of 5% in bcc Fe-Nb would be expected to reduce the average HMF by about 15 kG (Fultz 1993). In the as-milled $(Fe_3Si)_{.95}Nb_{.05}$ alloy, the peaks in the ^{57}Fe HMF distribution are at lower HMF's than in the binary Fe_3Si alloy, as expected when Nb atoms are near ^{57}Fe atoms. After further annealing, the peaks shift up to the normal peak positions for $D0_3$-ordered Fe_3Si. This is a second piece of evidence (along with the isomer shift-HMF correlation described below) consistent with a loss of Nb atom neighbors around ^{57}Fe atoms.

Meanwhile the intensities in the HMF distributions from 0 to 100 kG increase strongly after 1 hour of annealing, and tend to move towards lower HMF's. The components with low HMF must originate from regions where the Fe atoms have many nonmagnetic neighbors, i.e., Fe atoms in regions that are Nb-rich or Nb-Si-rich.

We conclude that during annealing at 450 °C, the Nb atoms leave the regions of $D0_3$-ordered Fe_3Si and form Nb-rich regions containing some Fe. No distinct contribution to the x-ray diffraction patterns could be attributed to such Nb-rich regions. This could be because these Nb-rich regions are clusters within the bcc crystallites, but we believe it is more likely that Nb atoms have segregated to grain boundaries, since grain growth is impeded strongly in the Nb-containing alloy.

Mössbauer Data Analysis for Nb — Isomer Shift-HMF Correlation

The as-milled alloys of Fe_3Si and $(Fe_3Si)_{.95}Nb_{.05}$ had clear differences in their isomer shifts (IS), with the ternary alloy having essentially the same IS for all chemical environments. This is seen as a better inversion-symmetry in the ternary alloy spectrum than for the binary alloy spectrum (see Figure 5.11). The IS versus HMF for the same alloys are presented in Figure 5.12. Large changes in the IS for the

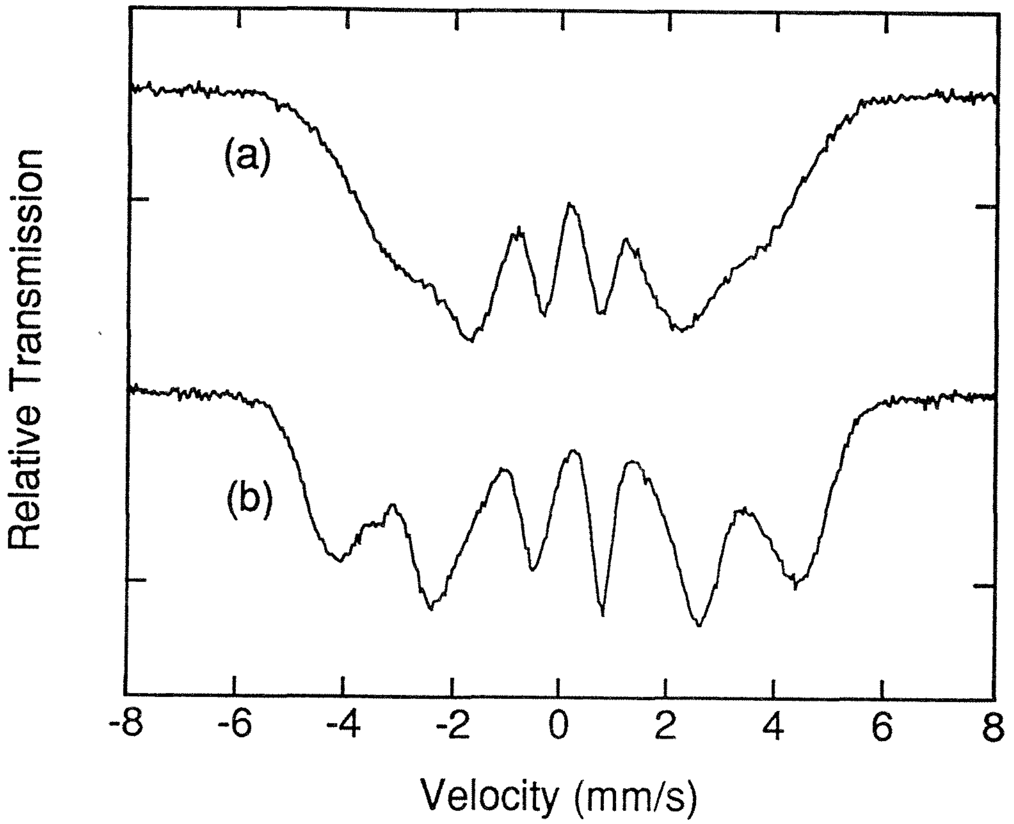

Figure 5.11 Comparison of Mössbauer spectra from as ball-milled alloys of (a) $(Fe_3Si)_{0.95}Nb_{0.05}$ and (b) Fe_3Si.

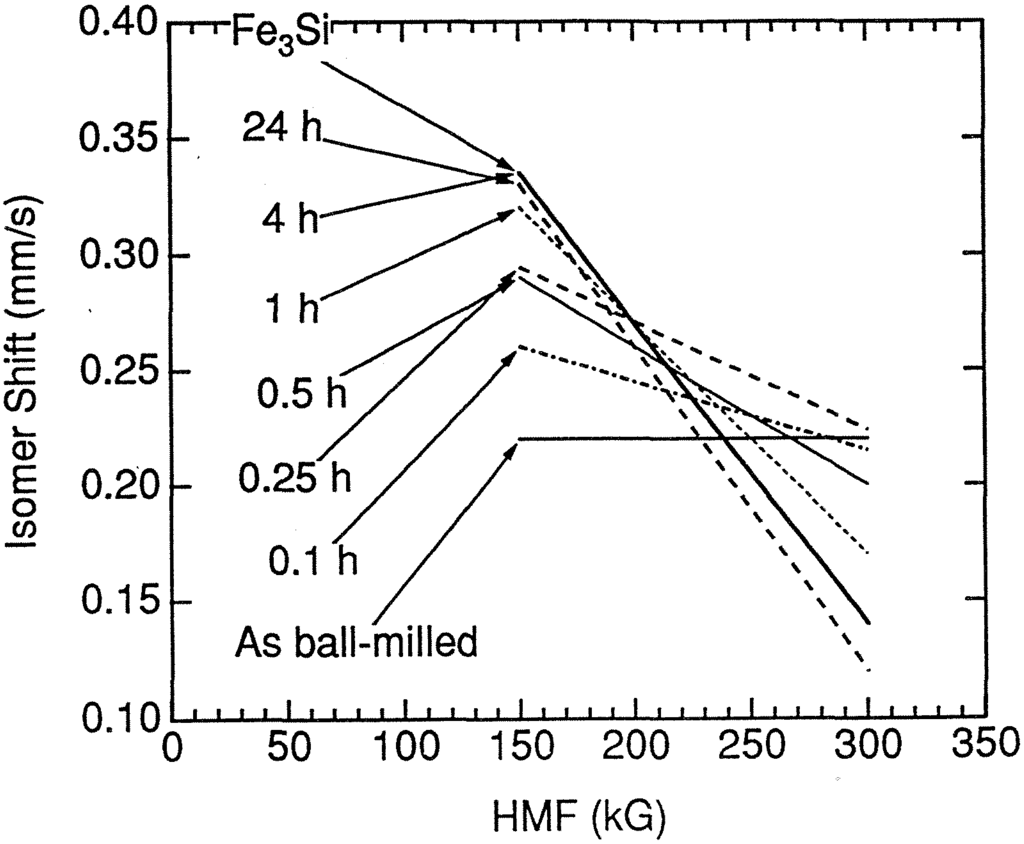

Figure 5.12 Isomer shift versus hyperfine magnetic field for the same alloys as in Figure 5.9.

ternary alloy $(Fe_3Si)_{.95}Nb_{.05}$ occur during the first hour of annealing at 450 °C, coinciding with the 10 kG upwards shift of the main peaks in the HMF distribution. On the other hand, the IS for the binary alloy of Fe_3Si did not change during annealing, and this relationship between IS and HMF for the binary alloy is also indicated in Figure 5.12. Notice that after 4 hours of annealing, the IS for the ternary alloy of $(Fe_3Si)_{.95}Nb_{.05}$ became identical to the IS of the binary alloy of Fe_3Si. We attribute this change in IS of the ternary alloy to a depletion of Nb atoms as nearest neighbors of ^{57}Fe atoms.

Local isomer shifts at ^{57}Fe nuclei in Fe alloys are related to the chemical properties of the neighboring solute atoms. Local isomer shifts caused by Nb have not been measured, but we expect them to be about –0.04 mm/s per nearest-neighbor Nb atom, based on calculations by Akai et al. (Akai, Blügel, Zeller and Dederichs 1986). If all the Nb atoms in $(Fe_3Si)_{.95}Nb_{.05}$ went from being in solid solution in the as-milled material to fully segregated after annealing, we would expect a change in average IS of +0.016 mm/s. The observed difference in IS for as-milled samples match this number quite well; the average IS for as-milled Fe_3Si is 0.237 mm/s, and that for $(Fe_3Si)_{.95}Nb_{.05}$ is 0.220 mm/s. The sign and magnitude of the local isomer shifts associated with Nb in the $(Fe_3Si)_{.95}Nb_{.05}$ alloy will probably be affected by Nb-Si chemical interactions in ways that confuse quantitative interpretations, however. [The electro-negativity difference between Nb and Si is much greater than between Nb and Fe (*Table of Periodic Properties of the Elements*, Sargent-Welch Scientific Company, 1980), and the heat of formation of a Nb-Si alloy is more negative than Nb-Fe or Fe-Si (Miedema, de Chatel and de Boer 1980).] We can, nevertheless, use the IS-HMF correlation of Figure 5.12 as an indicator of when Nb is present in the alloy, and when it is not. The IS-HMF correlation changed rapidly during the first hour of annealing at 450 °C, and became identical to that of the binary

Fe_3Si alloy after 4 hours of annealing. The IS-HMF correlation in the annealed alloy shows that Nb leaves the ordered Fe-Si domains, consistent with our interpretation of the changes in the HMF distribution. We therefore use the slope, A, of the linear relation between IS and HMF: IS = A * HMF + B, as a convenient indicator of Nb segregation.

§5.5 Discussion of Microstructural Evolution in Nanophase $(Fe_3Si)_{.95}Nb_{.05}$

Figures 5.13, 5.14 and 5.15 show the development of grain growth, Nb segregation, and short range ordering (SRO), respectively, for $(Fe_3Si)_{.95}Nb_{.05}$ annealed at various temperatures. For Nb segregation and SRO the evolution is similar: very small or no development at low temperatures for shorter times, and gradual development at higher temperatures. On the other hand, the grains started to grow after short annealings at the low temperature of 350 °C. By comparing the shifts in time scale for the data obtained at different temperatures, we estimated activation energies for these processes. For Nb segregation and SRO, the activation energies are both about 2.7 eV. For grain growth, the activation energy is about 1.5 eV. This difference in activation energies is consistent with the observation that at lower temperatures there is grain growth, although little SRO and Nb segregation occurs.

For normal curvature-driven grain growth, we expect a relation between grain size and time approximately as $d \propto t^{1/3}$. In Figure 5.13, such relations are drawn as dotted lines. For our samples annealed at 400 °C and 450 °C, grain growth followed approximately this $t^{1/3}$ relationship for times up to a few hours. This time scale coincides with the times required for Nb segregation and $D0_3$ chemical ordering.

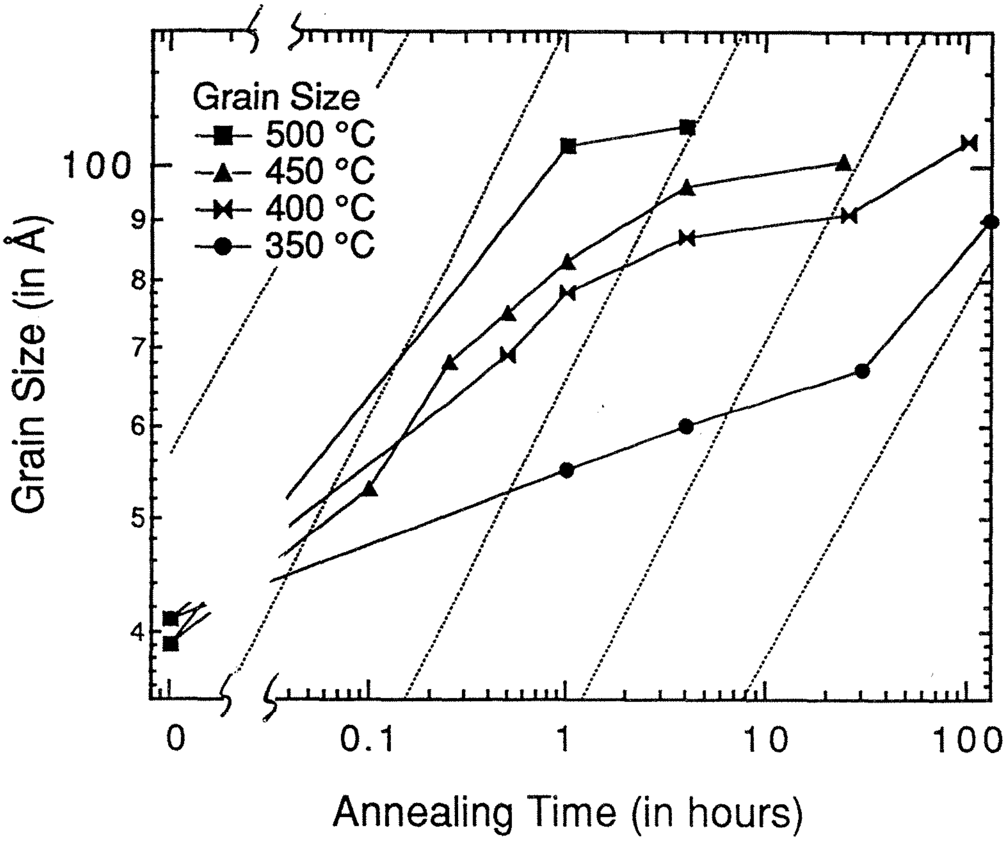

Figure 5.13 Grain growth of $(Fe_3Si)_{0.95}Nb_{0.05}$ at various temperatures. The dotted lines show the relation $d \propto t^{1/3}$.

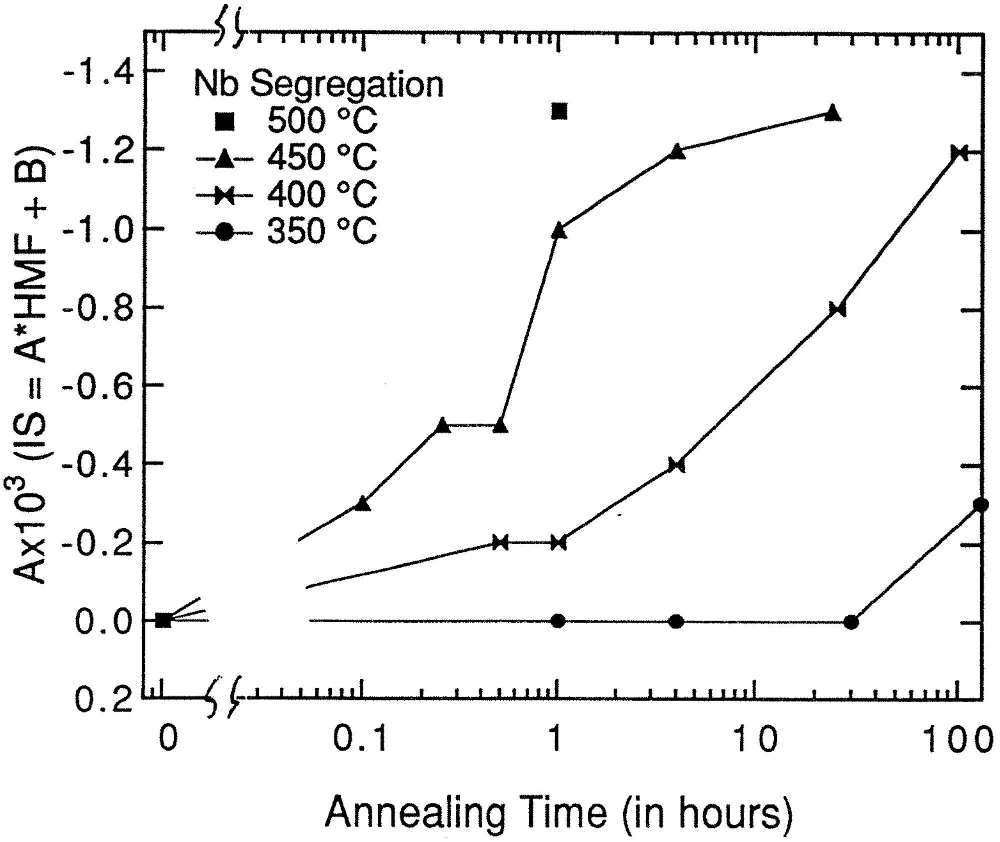

Figure 5.14 Nb segregation in $(Fe_3Si)_{0.95}Nb_{0.05}$ at various temperatures, obtained as the slope, A, in the linear relation between isomer shift and hyperfine magnetic field.

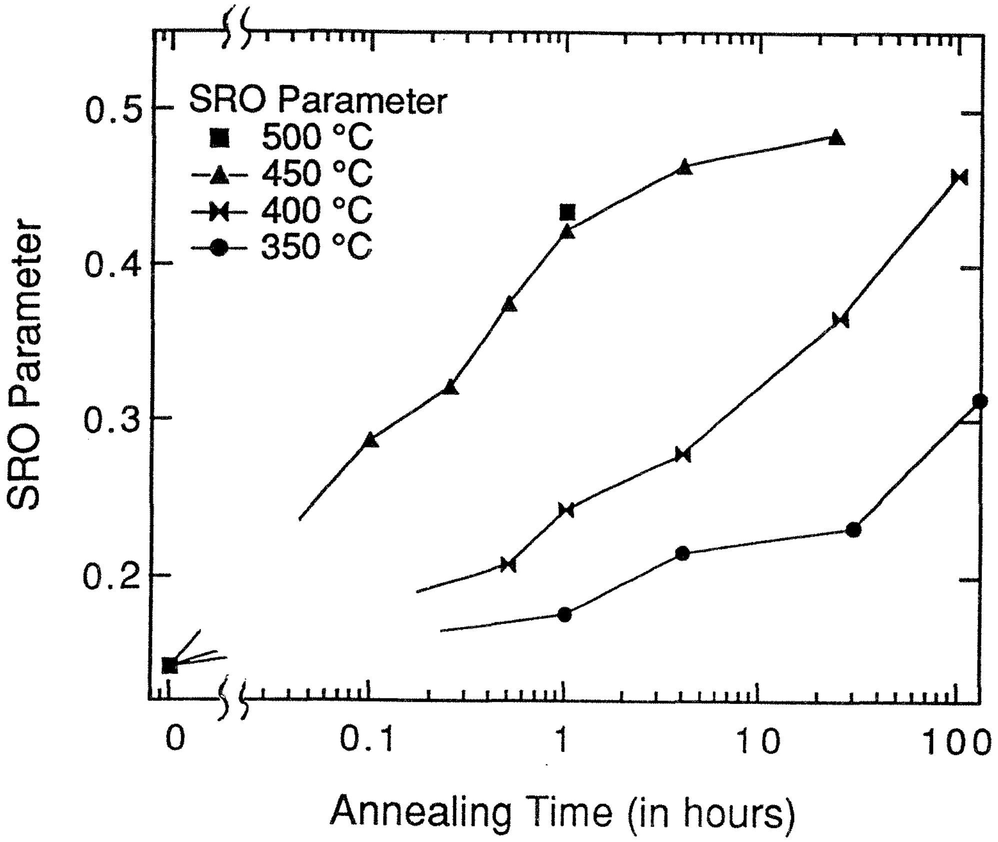

Figure 5.15 The evolution of short range order (SRO) for $(Fe_3Si)_{0.95}Nb_{0.05}$ annealed at various temperatures for various times.

This coincidence suggests that Nb segregation impedes grain growth for $(Fe_3Si)_{.95}Nb_{.05}$ nanocrystalline alloys, or perhaps the development of $D0_3$ chemical order could also be involved in the suppression of grain growth.

To help illustrate the interplay between the processes of grain growth, Nb segregation, and short range ordering, we prepared parametric plots of the three data sets of Figures 5.13 to 5.15. Two of these parametric plots are presented in Figures 5.16 and 5.17. Figure 5.16 presents Nb segregation versus grain size, and Figure 5.17 presents Nb segregation versus SRO.[*] The plots of Nb segregation versus grain size (Figure 5.16) are the more temperature-dependent. The data of Figure 5.16 are as expected when there is a lower activation energy for grain growth than for Nb segregation; higher temperatures will promote relatively more Nb segregation than grain growth. Grain growth at low temperature occurs without so much Nb segregation.

The data on Nb segregation versus SRO (Figure 5.17), are less temperature dependent, and these plots seem to fall on a common curve for all annealing temperatures. This temperature independence suggests that the processes of Nb segregation and short range ordering are closely inter-related. Certainly both Nb segregation and short range ordering require atomic diffusion, but the two processes involve different time and length scales. For Nb segregation, the Nb atoms must move over a dimension characteristic of the grain size, but for chemical ordering the Si and Fe atoms need to move only over distances of a unit cell or so. We therefore suggest that the inter-relationship between Nb segregation and SRO may be

---

[*] If grain growth is correlated to Nb segregation, and if Nb segregation is correlated to short range order, then grain growth must be correlated to short range order.

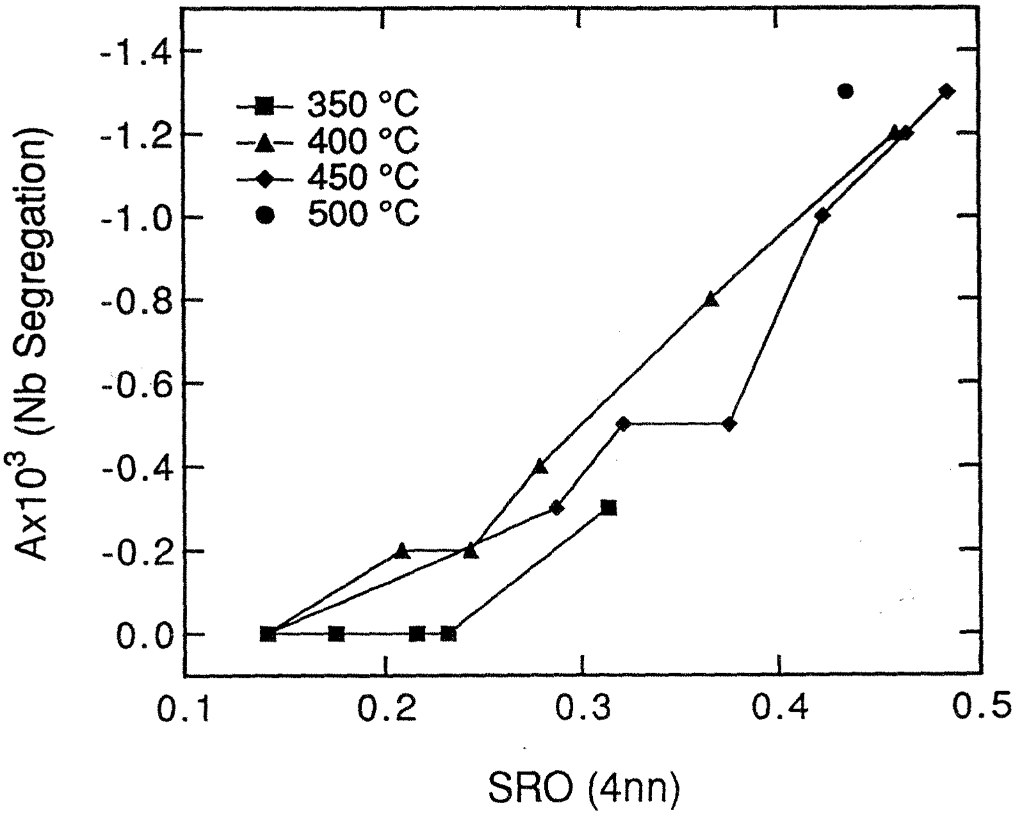

Figure 5.16 Nb segregation versus SRO for $(Fe_3Si)_{0.95}Nb_{0.05}$.

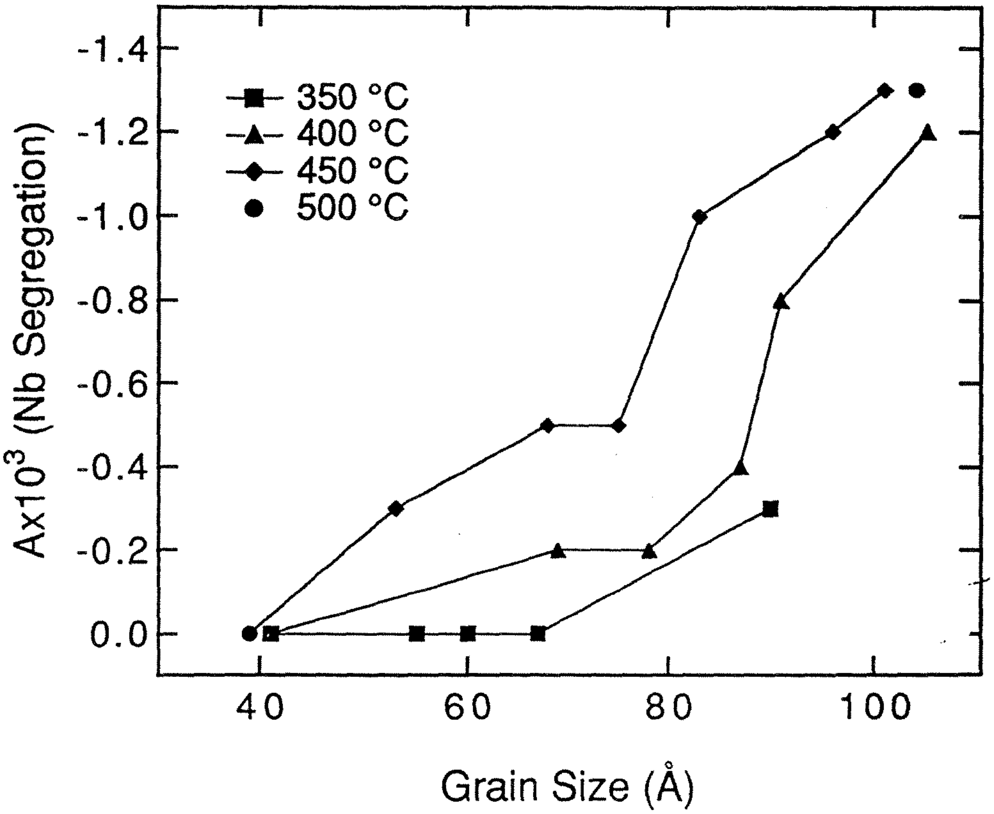

Figure 5.17 Nb segregation versus grain growth for $(Fe_3Si)_{0.95}Nb_{0.05}$.

thermodynamic and not kinetic. It may be that D0$_3$ ordering is not thermodynamically favorable when there is a significant Nb concentration in the crystal. After the Nb has segregated, however, the alloy becomes essentially pure Fe_3Si, as indicated by the Mössbauer spectrometry results. The D0$_3$ chemical order then develops in the Nb-free Fe_3Si.

The chemical segregation of niobium atoms may occur by either the formation of clusters within the Fe-Si grains, or by grain boundary segregation. Our microstructural information is presently insufficient to distinguish between these two possibilities. Nevertheless, we believe it is more likely that the niobium segregates to the grain boundaries, because this provides a mechanism for the niobium to impede grain growth in the ternary $(Fe_3Si)_{.95}Nb_{.05}$ alloy. A formation of niobium clusters within the Fe-Si grains could not explain the large difference in grain growth kinetics for the binary and ternary alloys.

§5.6 Conclusion --- Inter-dependence of Grain Growth, Nb Segregation and Chemical Ordering

We measured three microstructural changes during the annealing of ball-milled $(Fe_3Si)_{.95}Nb_{.05}$: grain growth, Nb segregation, and the development of D0$_3$ order. Both the HMF and the IS-HMF correlation showed that upon annealing, domains of D0$_3$-ordered Fe_3Si formed and Nb atoms were expelled from these domains. Niobium-rich regions containing Fe in weakly magnetic environments were detected.

The ternary $(Fe_3Si)_{.95}Nb_{.05}$ nanocrystalline alloy is more stable against grain growth than is the binary Fe_3Si alloy. Initial grain growth for $(Fe_3Si)_{.95}Nb_{.05}$ alloys follows the expected behavior of curvature-driven grain growth until significant Nb segregation has occurred. This evidence suggests that the Nb atoms segregate to the grain boundaries in the material, thereby suppressing grain growth. It is, however, observed that the development of $D0_3$ chemical order occurs over this same time scale, and it is possible that the development of chemical order could also be involved in the suppression of grain growth. As mentioned in Section §5.1 chemically disordered domains may allow for a reduced grain boundary enthalpy. As the grains grow larger, the grain boundary enthalpy becomes less important, and it is more favorable for order to develop. This seems to be the qualitative trend of our data (see Figure 5.10). The presence of niobium retards both grain growth and ordering kinetics, but the state of order for a given grain size is smaller for the binary alloy than the ternary alloy. The strong correlation between Nb segregation and SRO presented in Figure 5.16 suggests a thermodynamic explanation. We propose that, when Nb is present in Fe-Si, there is a smaller enthalpy reduction upon ordering.

The activation energies for ordering (2.7 eV) and Nb segregation (2.7 eV) are greater than for grain growth (1.5 eV). Such a difference in activation energy has a practical implication for annealings that are required for strain relief in soft magnetic materials. I suggest that annealings of this $(Fe_3Si)_{.95}Nb_{.05}$ are best performed at higher temperatures for shorter times to promote quicker Nb segregation that stabilizes the small grain size.

References

AKAI, H.; BLÜGEL, S.; ZELLER, R. and DEDERICHS, P. H.: *Phys. Rev. Lett.*, **56**, 2407 (1986).

ALBEN, R.; BECKER, J. J. and CHI, M. C.: *J. Appl. Phys.;* **49**, 1653 (1978).

AVERBACK, R. S.; HAHN, H.; HOFLER, H. J. and LOGAS, J. C.: *Appl. Phys. Lett.;* **57**, 1745 (1990).

BAKER, I. and SCHULSON, E. M.: *Scripta Metall.;* **23**, 345 (1989).

BOHN, R.; HAUBOLD, T.; BIRRINGER, R. and GLEITER, H.: *Scripta Metall.;* **25**, 811 (1991).

CHANG, H.; HÖFLER, H. J.; ALTSTETTER, C. J. and AVERBACK, R. S.: *Scripta Metall.;* **25**, 1161 (1991).

CHEN, C.: Magnetism and Metallurgy of Soft Magnetic Materials, (Dover Publications, New York, 1986), p. 82.

EASTMAN, J. and SIEGEL, R. W.: *Research and Development,* Jan.; 56 (1989).

ECKERT, J.; HOLZER, J. C. and JOHNSON, W. L.: *J. Appl. Phys.;* **73**, 131 (1993).

ECKERT, J.; HOLZER, J. C. and JOHNSON, W. L.: J. *Mater. Res.;* **7**, 1751 (1992).

ESCORIAL, A. C.; ADEVA, P.; CRISTINA, M. C.; MARTIN, A.; CARMONA, F.; CEBOLLADA, F.; MARTIN, V. E.; LEONATO, M. and GONZALEZ, J. M.: *Mat. Sci. and Eng.;* **A134**, 1394 (1991).

FECHT, H. J.; HAN, G.; FU, Z. and JOHNSON, W. L.: *J. Appl. Phys.;* **67**, 1744 (1990).

FULTZ, B.: "Chemical Systematics of Iron-57 Hyperfine Magnetic Field Distributions in Iron Alloys," in Mössbauer Spectroscopy Applied to Magnetism and Materials Science, G. J. Long and F. Grandjean, eds.; (Plenum Press, New York, 1993) Chapter 1, p. 1.

FULTZ, B.; Le CAËR, G. and MATTEAZZI, P.: *J. Mater. Res.;* **4**, 1450 (1989).

GAO, Z. Q. and FULTZ, B.: *Phil. Mag.*, **67**, 787 (1993).

GENGNAGEL, H. and WAGNER, H.: *Z. Angew. Physik*, **8**, 174 (1961).

GLEITER, H.: *Progress in Materials Science,* **33**, 223 (1989).

HAHN, H.; LOGAS, J. and AVERBACK, R. S.: *J. Mater. Res.;* **5**, 609 (1990).

HAMPEL, G.; PUNDT, A. and HESSE, J.: *J. Phys.: Condens. Matter*, **4**, 3195 (1992).

HARRIS, S. R.; PEARSON, D. H.; GARLAND, C. M. and FULTZ, B.: *J. Mater. Res.;* **6**, 2019 (1991).

HAUBOLD, T.; BOHN, R.; BIRRINGER, R. and GLEITER, H.: *Mater. Sci. Eng.;* **A153**, 679 (1992).

HAUBOLD, T.; BOHN, R.; BIRRINGER, R. and GLEITER, H.: *Mater. Sci. Eng.;* **A153**, 679 (1992).

HELLSTERN, E.; FECHT, H. J. and JOHNSON, W. L.: *J. Mater. Res.;* **4**, 1292 (1989).

HERZER, G.: *IEEE Trans. Magn.;* **26**, 1397 (1990).

HERZER, G.: *Mat. Sci. & Eng.;* **A133**, 1 (1991).

HÜLLER, K.: *J. Magn. Magn. Mater.;* **61**, 347 (1986).

JANG J. S. C. and KOCH, C. C.: *J. Mater. Res.;* **5 (3)**, 498 (1990).

JOHNSON, W. L.: private commun.

JORRA, E.; FRANZ, H.; PEISL, J.; WALLNER, G.; PETRY, W.; BIRRINGER, R.; GLEITER, H. and HAUBOLD, T.: *Phil. Mag.;* **B 60**, 159 (1989)

KAITO C. and SHIOJIRI, M.: *Jpn. J. Appl. Phys.;* **21**, L421 (1982).

KOCH, C. C.: *Nanostructured Materials*, **2**, 109 (1993).

KOCH, C. C.; CAVIN, O. B.; MCKAMEY, C. G. and SCARBOROUGH, J. O.: *Appl. Phys. Lett.;* **43**, 1017 (1983).

KUHRT, Ch. and SCHULTZ, L.: *J. Appl. Phys.;* **71**, 1896 (1992).

KUWANO, H.; OUYANG, H. and FULTZ, B.: *Nanostructured Materials*, **1**, 143 (1992).

LASALMONIE, A. and STRUDEL, J. L.: *J. Mater. Sci.;* **21**, 1837 (1986).

LE CAËR, G. and DUBOIS, J. M.: J. Phys. E 12, 1083 (1979).

LI, M.; BIRRINGER, R.: JOHNSON, W. J. and SHULL, R. D.: *Nanostructured Materials*, **3**, 407 (1993).

MIEDEMA, A. R.; DE CHATEL, P. F. and DE BOER, F. R.: *Physica*, **100B**, 1 (1980).

SCHULSON, E. M. and BAKER, I.: *Scripta Metall.;* **25**, 1253 (1991).

SIEGEL, R. W.: *Annu. Rev. Mater. Sci.;* **21**, 559 (1991).

SIEGEL, R. W.; RAMASAMY, S.; HAHN, H.; LI, Z.; LU, T.; and GRONSKY, R.: *J. Mater. Res.;* **3**, 1367 (1988).

STEARNS, M. B.: *Phys. Rev.*, **129**, 1136 (1963).

TRUDEAU, M. L. and SCHULZ, R.: *Mater. Sci. Eng.;* **A134**, 1361 (1991).

WEISSMÜLLER, J.: *J. Mater. Res.;* **9**, 4 (1994).

WEISSMÜLLER, J.: *Nanostructured Materials;* **3**, 261 (1993).

YERMAKOV, A. Y.; YURCHINKO, Y. Y. and BARINOV, V. A.: *Phys. Met. Metall.;* **52**, 50 (1981).

YOSHIZAWA, Y. and YAMAUCHI, K.: *Mat. Sci. and Eng.;* **A133**, 176 (1991).

YOSHIZAWA, Y.; OGUMA, S. and YAMAUCHI, K.: *J. Appl. Phys.;* **64**, 6044 (1988).

Chapter 6 Summary and Perspective

Mössbauer spectrometry is sensitive to chemical environments local to the ^{57}Fe atom, and it is relatively insensitive to other types of disorder such as internal strains, atomic size differences, dislocations, and grain boundaries (so long as the grain size is around 10 nm or larger). These other types of disorder are troublesome for detailed interpretations of diffraction experiments, so Mössbauer spectrometry can sometimes have an advantage in measuring chemical order in rapidly quenched or ball milled materials. For many alloys, however, the details in the Mössbauer spectra are not easily interpreted quantitatively in terms of specific chemical environments; this is especially true for magnetic solute atoms. For Fe-Al, Fe-Si and Fe-Ge, however, the local chemical environments are seen with great detail even for concentrated alloys. Not just the average first neighbor environment can be determined, but the whole distribution of 1nn solute environments around the ^{57}Fe atoms can be measured. This high level of detail made possible the present study of kinetics of short range ordering in materials with a high degree of disorder.

The kinetics studies of disorder to order transformations show that the kinetic paths for Fe_3Al are temperature dependent. At lower annealing temperatures (well below the critical temperature of $D0_3$ order) there is a tendency for evolving B2 order along with $D0_3$ order. When the disordered as-quenched samples are annealed at higher temperatures, for example 300 °C, a transient B32 order was observed. The temperature dependencies of the kinetic paths are qualitatively consistent with the results of analytical studies of the kinetics of ordering as well as results of Monte Carlo simulations (Anthony and Fultz 1994), where activated state rate theory was used to model the atom movements.

Nevertheless, although transient B32 order was also observed in the analytical calculations and Monte Carlo simulations, its formation always required a very strong 2nn interatomic interaction, normally at least as strong as the 1nn interaction. No transient B32 order has yet been reported for weaker 2nn interactions. For Fe_3Al such a strong 2nn interaction seems improbable, being inconsistent with the phase diagram. Perhaps a more complex mechanism controls the diffusion process during disorder to order transformations than is assumed in activated state rate theory.

Another interesting observation in our experimental work on Fe_3Al is the sensitivity of its kinetic path to its initial state. Only if a sample is initially a nearly random solid solution is the transient B32 order observed. Because the cooling rate of the piston-anvil quenching is quite close to the critical cooling rate to get a disordered Fe_3Al alloy, it is quite common to obtain "bad" as-quenched samples with traces of B2 order. Upon annealing these samples will develop $D0_3$ order rapidly and the B32 transient state is not observed.

It is interesting to look at the locations of the B32 ordered state and the disordered state on an approximate analytical free energy surface (Figure 4.9). Both states are at points where $\frac{dF}{d\eta} = 0$. (η is an order parameter.) Because of the relatively flat free energy surface, the lack of a driving force may keep the alloy in these macrostates for a long time while it samples many possible microstates. The relatively long lasting nature of the macrostates at saddle points in analytical theory brought an interesting perspective to kinetics studies of highly nonequilibrium materials, and the macrostate at a saddle point is termed a *pseudostable state* (Kikuchi, Mohri and Fultz 1992, Fultz 1993).

The temperature independence of the kinetic paths for ball milled Fe_3Si and Fe_3Ge alloys was at first a little unexpected, since these alloys have similarities in their phase diagrams to Fe-Al. The temperature independence of the kinetic paths for Fe_3Si and Fe_3Ge may be because these alloys have stronger interatomic interactions (or larger enthalpies during their ordering transformation). This is evidenced by their much higher critical temperatures. How the stronger interactions affect kinetic paths is still unclear, however.

The temperature independence of the kinetic paths for Fe_3Si and Fe_3Ge may also come from their different microstructures from that of Fe_3Al. Since the disordered Fe_3Al alloy was prepared by rapid quenching, its initial state consists of large grains with little chemical order. As the chemical order starts evolving upon annealing, there is no grain growth and the disorder to order transformations normally happen within the same grain. On the other hand, for Fe_3Si and Fe_3Ge, the disordered states cannot be reached by rapid quenching and thus the ball milling method was used. Their initial microstructures have very small grain sizes (about 10 nm), and upon annealing both ordering and grain growth happen simultaneously. The processes of ordering and grain growth may not be independent. Obviously, during grain growth, as a new atom moves to a growing grain, it is very likely to settle in a position with short range order since this is energetically preferable.

On the other hand, grain growth process may also be influenced by the ordering process. Since an atom in an ordered environment has a lower chemical potential, it is more difficult to make it move, which may be required for grain growth. The ordered structure usually has a lower diffusion coefficient, and thus a slower diffusion process for grain growth.

It is important to study the inter-dependency of ordering and grain growth. This inter-dependency is not only relevant to ordering kinetics, but is also relevant to grain growth in nanocrystalline materials.

The final experiment in this thesis research was a more complicated problem that included a process of chemical segregation. The kinetic study of the grain growth, chemical ordering and chemical segregation processes in $(Fe_3Si)_{0.95}Nb_{0.05}$ nanocrystalline alloy showed a clear inter-dependency. The Nb segregation is closely correlated with ordering. There may be practical significance to this. The evidence is strong that the Nb atoms segregate to grain boundaries and suppress the grain growth. Perhaps we should seek an annealing temperature that maximizes the ordering , thus Nb segregation, and thereby impedes the grain growth. Because of the higher activation energy for Nb segregation than for grain growth (2.7 eV vs. 1.5 eV), annealing the sample at a relatively higher temperature, instead of at a lower temperature, can promote Nb segregation and ordering more than grain growth. This could be used to synthesize nanocrystalline materials with grain size stabilized at a smaller level (because of a fast segregation to the grain boundaries) and, at the same time, with less internal strain and fewer defects. I would like to try this approach for making nanocrystalline Fe-Si-Ge-Nb alloys with soft magnetic properties.

References

ANTHONY, L. and FULTZ, B.: *J. Mater. Res.*, **9**, 348 (1994).

FULTZ, B.: *Phil. Mag.*, **B 67**, 253 (1993).

KIKUCHI, R; MOHRI, T. and FULTZ, B.: *Mat. Res. Soc. Symp. Proc.*, **205**, 387 (1992).

Appendix A. Intensity Correction for X-ray Diffraction Patterns Obtained with a Position Sensitive Detector

Developments in computers and microelectronics have made possible a new kind of detector for X-ray powder diffraction. Its emerging changed the face of X-ray diffractometer. This Curved Position Sensitive Detector (CPSD) is changing qualitatively the way X-ray powder diffraction is performed in materials science. The main characteristic of this detector is its ability to detect the diffracted X-rays simultaneously over a large angular range of 2θ angle. Figure A.1 present a schematic illustration of the geometrical arrangement of a X-ray diffraction system with a curved position sensitive detector.

In this thesis research, an X-ray diffractometer equipped with an INEL CPS-120 CPSD was used extensively to study the early stages of ordering and the structure of nanocrystalline materials. (Figure A.1 schematically depicts the INEL CPS-120 diffractometer system.) At the early stages of ordering the superlattice diffraction intensities are very weak. A conventional X-ray diffractometer requires an extremely long counting time to get superlattice diffractions with adequate statistics. Because of the simultaneity of the position sensitive detector, however, a high quality X-ray diffraction pattern over a large 2θ range can be obtained within hours. While the CPSD enormously improves the efficiency of data collecting, it does cause some problems that do not occur in a system with a conventional detector.

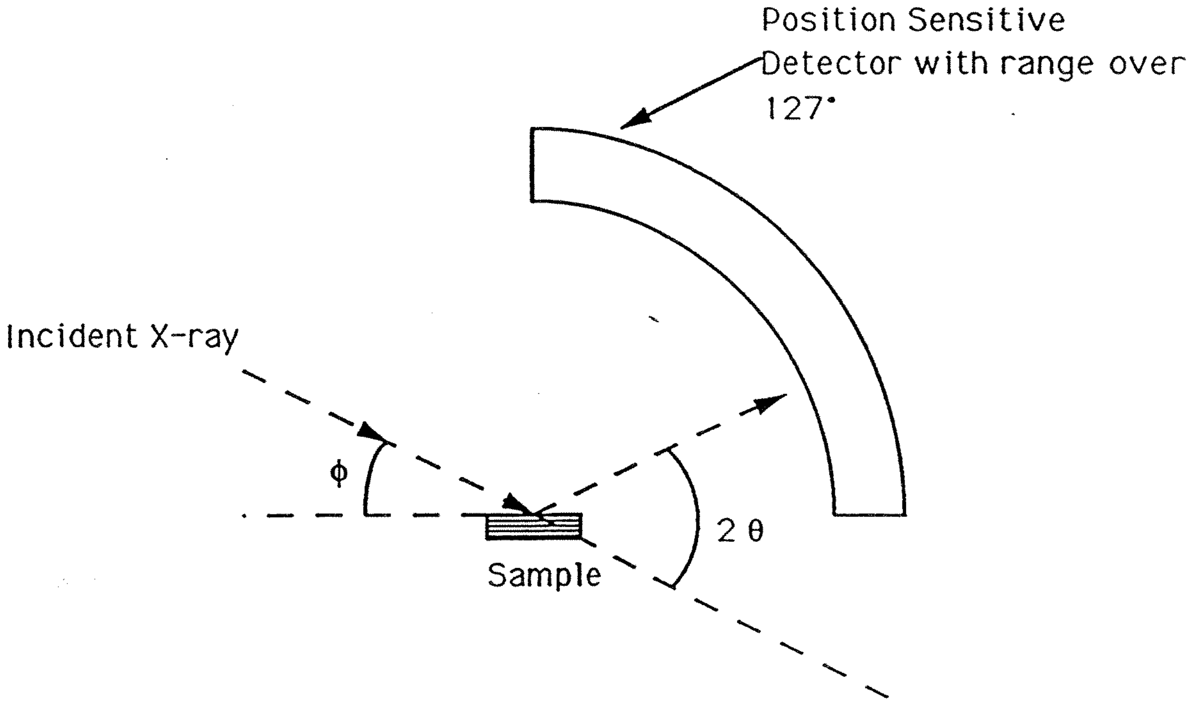

Figure A.1 Schematic of INEL CPS-120 X-ray diffractometer.

The CPSD is operated with fixed incident angle, ϕ. For different Bragg angles, 2θ, Figure A.2 shows that there must be differences in out going angle, ξ. Consequently, $\Delta\mathbf{k}$, which is the difference between the outgoing wave vector and the incident wave vector, varies in orientation for each Bragg peak. The $\Delta\mathbf{k}$ is not normal to the specimen as is the case for a Bragg-Brentano powder diffractometer. This variation in $\Delta\mathbf{k}$ should not be an issue for isotropic materials, however.

There is a more important issue involving the CPSD diffractometer geometry, however. In this appendix I will analyze the dependence of the diffraction intensity from a flat sample on the incident angle of the X-ray beam, accounting for the special absorption condition of the CPSD. The X-ray diffraction data in this note were obtained with an INEL CPS-120 powder diffractometer system with Co Kα radiation. The experimental data were from Fe_2O_3 powder.

The Effect of Absorption

Because the position sensitive detector has a fixed angle of incidence, the absorption corrections for a flat sample differ from those for a conventional Bragg-Brentano diffractometer. As presented in Figure A.2, the volume irradiated in an element of dz thickness at a depth z is $(A/\sin\phi)dz$, where A is the area of the incident beam. The incident intensity at the depth of z is $I_0\exp(-\mu z/\sin\phi)$, which is attenuated by absorption along the path of length $z/\sin\phi$, and for the case of position sensitive detector this part of the absorption is a constant. The most interesting issue for a position sensitive detector is the absorption that occurs as the diffraction beam leaves the sample. The attenuation factor of this part is $\exp(-\mu z/\sin\xi)$, which depends on the direction of the outgoing beam. Denote b as the fraction of the incident beam that is diffracted. For a sample of thickness t, the intensity of the diffracted beam emerging from the sample is:

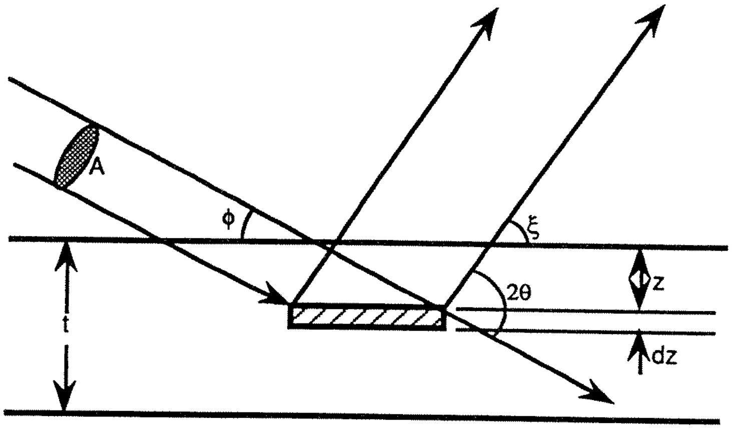

Figure A.2 Schematic drawing of X-ray diffracted from a flat sample.

$$I_D = I_0 b\,\Delta V\ , \tag{A.1}$$

$$I_D = I_0 b \int_0^t \frac{A}{\sin\phi} \exp\left[-\mu z\left(\frac{1}{\sin\phi} + \frac{1}{\sin\xi}\right)\right] dz. \tag{A.2}$$

We assume here that the sample is thick enough so that we can let t → ∞, then we can get a simple result:

$$I_D = \frac{I_0 A}{\mu}\left(\frac{\sin\xi}{\sin\phi + \sin\xi}\right), \tag{A.3}$$

where $\xi = 2\theta - \phi$.

For the conventional X-ray diffraction method, $\phi = \xi = \theta$, so the angle term cancels and leaves the absorption effect independent from the diffraction direction.

$$I_D^{\text{Bragg}} = \frac{I_0 A}{2\mu}, \tag{A.4}$$

but for the X-ray diffraction with a position sensitive detector, this effect depends on the glancing angle, ϕ, and the diffraction angle, 2θ:

$$I_D^{PSD} = \frac{I_0 A}{\mu}\left(\frac{\sin(2\theta - \phi)}{\sin\phi + \sin(2\theta - \phi)}\right). \tag{A.5}$$

We can eliminate the angle dependency of the absorption effect by dividing the experimental data, obtained with CPSD diffractometer, with this absorption correction factor, $F(\theta, \phi)$:

$$F(\theta,\phi) = \left(\frac{\sin(2\theta - \phi)}{\sin\phi + \sin(2\theta - \phi)}\right). \tag{A.6}$$

The absorption correction factors for several glancing angles are plotted in Figure A.3 as examples.

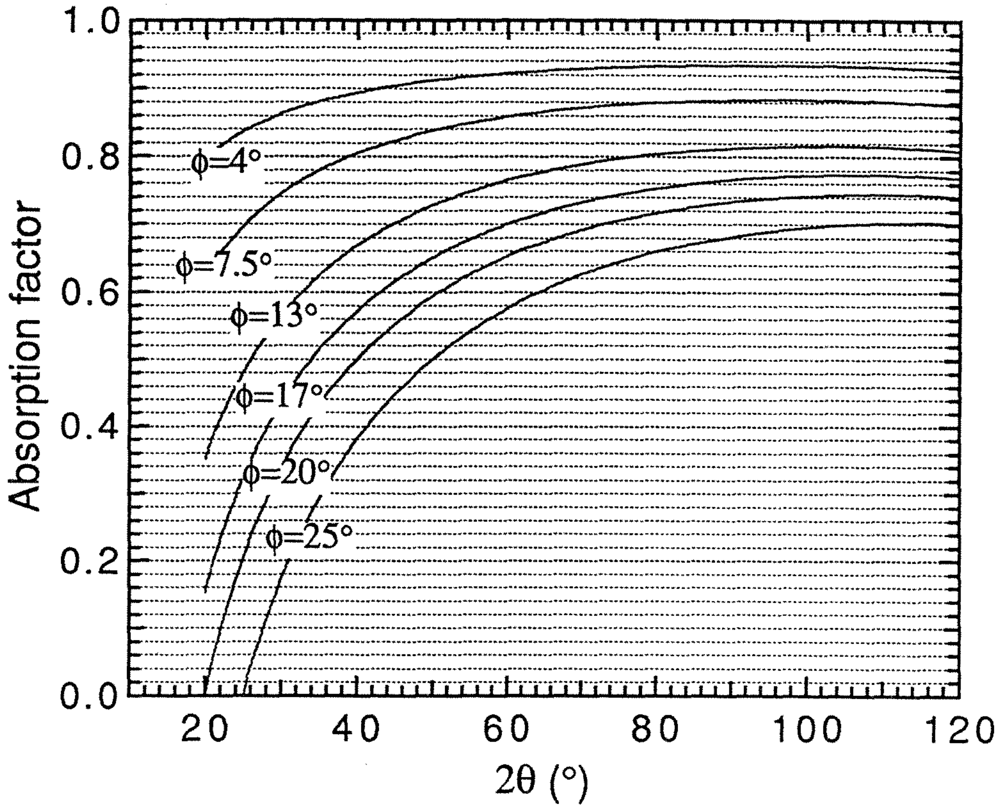

Figure A.3 Absorption correction factor $F(\theta, \phi)$ for various glancing angles.

Table 1 gives an example of this correction. X-ray diffraction patterns were obtained at two different incident angles from ferric oxide (Fe_2O_3) powder. Diffraction intensities were obtained by integrating each of the diffraction peaks and then normalizing to the strongest one. The data after correction were obtained by dividing the data before correction with their corresponding absorption correction factor and then normalizing to the strongest peak again. A very good agreement is obtained, as it is shown in Table A.1.

This intensity correction method is used in all of our X-ray diffraction work with the CPSD system, provided that quantitative intensity measurements are needed. With this correction we can change the incident angle to a desirable one according to the experimental needs, and still can compare the results to other data. We can also compare our data from the CPSD diffractometer to data from conventional system mores precisely.

Table A.1. Relative diffraction intensities from our Fe_2O_3 sample, before and after correction.

	Before Correction		After Correction	
2θ angle	$\phi = 13°$	$\phi = 24°$	$\phi = 13°$	$\phi = 24°$
28.1°	25	13	30	31
38.8°	100	100	100	100
41.8°	70	72	67	65
48.1°	35	40	32	31
58.5°	43	60	37	40
64.1°	59	85	50	53
68.4°	12	19	11	12
86.5°	17	27	14	15

References

JEANMART, P. and BOUVAIST, J.: "The Curved Position Sensitive Detector (CPS 120-INEL): Description and Applications to Materials," comes with INEL 3000 manual.

SCHWARTZ, L. H. and COHEN, J. B.: in Diffraction from Materials, (Springer-Verlag, New York 1987).

Appendix B. Source Code for Diffraction Image Contrast Calculation

In this appendix, I include the source code for the diffraction image contrast calculation used in Chapter 3.

B.1 Makefile

```
# Makefile for imagsimu and related programs
#

CCOMPL = cc
#CFLAGC = -O0 -g
#CFLAGC = -O3
CFLAGC = -O4
FCOMPL = f77
#FFLAGC = -O0 -g -static -u -C
#FFLAGC = -O3 -static -u
FFLAGC = -O4 -static -u
LIBS   = -lpgplot -lU77 -lI77 -lF77 -lm -lc

all: imagsimu

imagsimu:       imagsimu.h imagsimu.c Makefile
        $(FCOMPL) $(FFLAGC) -o imagsimu imagsimu.c $(LIBS)
        rm -f imagsimu.o imagsimu.u
        strip imagsimu
```

B.2 imagsimu.h

```
/*************************
imagsimu.h:

Header file for imagsimu.c.
**************************/


#include <stdio.h>
#include <math.h>
#include <strings.h>
```

```
#define RAND_MAX       2147483648.0

/*
 * #define RAND_SEED to an appropriate seed value (integer)
 * for initializing the the random number generator.
 */
#define RAND_SEED      42
#define SIZE           80
#define CELLS          (SIZE * SIZE * SIZE)

#define NCORE                  500
/* Number of cores for growing to domains.*/

#define NCELL                  2
/* Number of different cell for each kind order.
For B2 order, it is 2. For D03 order, it is 4.*/

#define NSTEPS                 100
/* Total simulation steps. */

#define D_POINT                9

static int lattice[SIZE][SIZE][SIZE];
static int image[SIZE][SIZE];
static int ampli_r[SIZE][SIZE], ampli_i[SIZE][SIZE];


static int nn_x[6] = {1, 0, 0, -1, 0, 0};
static int nn_y[6] = {0, 1, 0, 0, -1, 0};
static int nn_z[6] = {0, 0, 1, 0, 0, -1};

void randomize();
void grow();
void imaging();
int checkpoint();
void diff_out();
void latt_out();
void grayprint();

void srandom(int);
long random(void);

void pgbegin_();
void pgask_();
void pgenv_();
void pglabel_();
void pgmtext_();
void pgpoint_();
void pggray_();
void pgupdt_();
void pgend_();
```

B.3 imagsimu.c

```
/******************************
Program imagsimu.c

This program is designed to the effect on the TEM image from
different antiprase domain size and the overlap of the domains.

******************************/

#include "imagsimu.h"

main()
{
        int i, j, k;

        srandom(RAND_SEED);

        randomize();

        for (i=0; i<NSTEPS; i++){
                for (j=0; j< (10 * CELLS); j++)
                        grow();
                k = checkpoint();
                if (k == -1)
                        i = NSTEPS - 1;
                printf("%d\t%d\n", i, k);
        }

        imaging();
        diff_out();
        latt_out();
        grayprint();

}

void randomize()
{
        int i, x, y, z, s;

        for (x=0; x<SIZE; x++)
                for (y=0; y<SIZE; y++)
                        for (z=0; z<SIZE; z++){
                        lattice[x][y][z] = D_POINT;
                        }

        for (i=0; i<NCORE; i++){

            x = (int)(((double)random()/(double)RAND_MAX) * SIZE) % SIZE;
            y = (int)(((double)random()/(double)RAND_MAX) * SIZE) % SIZE;
            z = (int)(((double)random()/(double)RAND_MAX) * SIZE) % SIZE;

            s = (int)(((double)random()/(double)RAND_MAX) * NCELL) % NCELL;

            if (NCELL==2)
                s = 2 * s;
```

```
            lattice[x][y][z] = s;

            }

}

void grow()
{
        int i, x, y, z, mx, my, mz, s;

        x = (int)(((double)random()/(double)RAND_MAX) * SIZE) % SIZE;
        y = (int)(((double)random()/(double)RAND_MAX) * SIZE) % SIZE;
        z = (int)(((double)random()/(double)RAND_MAX) * SIZE) % SIZE;

        if (lattice[x][y][z] != D_POINT){

                for (i=0; i<6; i++){
                        mx = (x + nn_x[i]) % SIZE;
                        my = (y + nn_y[i]) % SIZE;
                        mz = (z + nn_z[i]) % SIZE;

                        if (lattice[mx][my][mz] == D_POINT)
                                lattice[mx][my][mz] = lattice[x][y][z];
                }
        }
}


void imaging()
{
        int x, y, z;

        for (x=0; x<SIZE; x++)
                for (y=0; y<SIZE; y++){
                        ampli_r[x][y] = 0;
                        ampli_i[x][y] = 0;
                        image[x][y] = 0;
                }

        for (x=0; x<SIZE; x++)
                for (y=0; y<SIZE; y++){
                        for (z=0; z<SIZE; z++){
                                if (lattice[x][y][z] == 0)
                                     ++ampli_r[x][y];
                                else if (lattice[x][y][z] == 1)
                                     ++ampli_i[x][y];
                                else if (lattice[x][y][z] == 2)
                                     --ampli_r[x][y];
                                else if (lattice[x][y][z] == 3)
                                     --ampli_i[x][y];
                        }

                        image[x][y] = ampli_r[x][y] * ampli_r[x][y]
                                    + ampli_i[x][y] * ampli_i[x][y];


                }
```

```
}

int checkpoint()
{
        int x, y, z, k;

        k = 0;

        for (x=0; x<SIZE; x++)
                for (y=0; y<SIZE; y++)
                        for (z=0; z<SIZE; z++)
                                if (lattice[x][y][z] == D_POINT)
                                     ++k;
        if (k != 0)
             return k;
        else
             return -1;
}

void diff_out()
{
        int x, y, z;
        char filename[20];

        int s = NCORE;

        FILE *fp, *fopen();

        sprintf(filename, "diff_inten.dat");
        fp = fopen(filename, "w");

/*      fprintf(fp, "Simulated diffraction intensities with %d seeds\n", s);
        fprintf(fp, "image\tampli_r\tampli_i\n");
*/
        for (x=0; x<SIZE; x++)
                for (y=0; y<SIZE; y++)
/*                      fprintf(fp, "%d\t%d\t%d\n", image[x][y], ampli_r[x][y],
ampli_i[x][y]);*/
                     fprintf(fp, "%d\n", image[x][y]);
        fclose(fp);
}

void latt_out()
{
        int x, y, z;
        char filename[20];

        int s = NCORE;

        FILE *fp, *fopen();

        sprintf(filename, "diff_latt.dat");
        fp = fopen(filename, "w");

        fprintf(fp, "Lattice with Antiphrase Domains for imagsimu.c\n");
```

```
        for (x=0; x<SIZE; x++) {
                for (y=0; y<SIZE; y++) {
                        for (z=0; z<SIZE; z++)
                                fprintf(fp, "%d", lattice[x][y][z]);
                        fprintf(fp, "\n");
                        }
                fprintf(fp, "\n");
        }
        fclose(fp);

}

/* call pgplot routins */

void grayprint()
{
      float image_max, image_min;
        int x, y, z;
        int dummy, nx, ny;
        int just, axis;
        float xmin, xmax, ymin, ymax;
        float fg, bg;
        int idim, jdim, i1, i2, j1, j2;
        float nimage[SIZE][SIZE];

        static float tr[6] = { -1.0, 1.0, 0.0, -1.0, 0.0, 1.0 };

        for (x=0; x<SIZE; x++)
          for (y=0; y<SIZE; y++)
            nimage[x][y] = (float)image[x][y]/SIZE;

        image_max = nimage[1][1];
        image_min = nimage[1][1];

        for (x=0; x<SIZE; x++)
                for (y=0; y<SIZE; y++){
                        if (nimage[x][y] > image_max)
                                image_max = nimage[x][y];
                        else if (nimage[x][y] < image_min)
                                image_min = nimage[x][y];
                }
        printf("%f\t%f\n", image_min, image_max);

        dummy = 0;
        nx = 1;
        ny = 1;

        pgbegin_(&dummy, "?", &nx, &ny, 1L);

        xmin = -1.;
        xmax = SIZE;
        ymin = -1.;
        ymax = SIZE;
        just = 1.;
        axis = -1.;

        pgenv_(&xmin, &xmax, &ymin, &ymax, &just, &axis);
```

```
        fg = image_max;
        bg = image_min;

        idim = SIZE;
        jdim = SIZE;
        i1 = 1;
        i2 = SIZE;
        j1 = 1;
        j2 = SIZE;

        pggray_(&(nimage[0][0]), &idim, &jdim, &i1, &i2, &j1, &j2, &fg, &bg, tr);

        pgend_();

}
```

Appendix C. Magnetization Data

Magnetic properties were measured with a vibration sample magnetometer at the National Institute of Standards and Technology. The magnetization data for two samples are shown in Table C.1, and the hysteresis loops are presented in Figures C.1 to C.4.

Table C.1: Magnetization data for FSN2.45.24 and FS2.45.24.

Sample	FSN2.45.24	FS2.45.24
Mr (A.m^2/kg)	0.426	0.404
Ms (A.m^2/kg)	92.0	129.0
H_c (kA/m)	0.725	0.642

FSN2.45.24:	$(Fe_3Si)_{0.95}Nb_{0.05}$ nanocrystalline alloy after annealing at 450 °C for 24 hours.
FS2.45.24:	Fe_3Si nanocrystalline alloy after annealing at 450 °C for 24 hours.

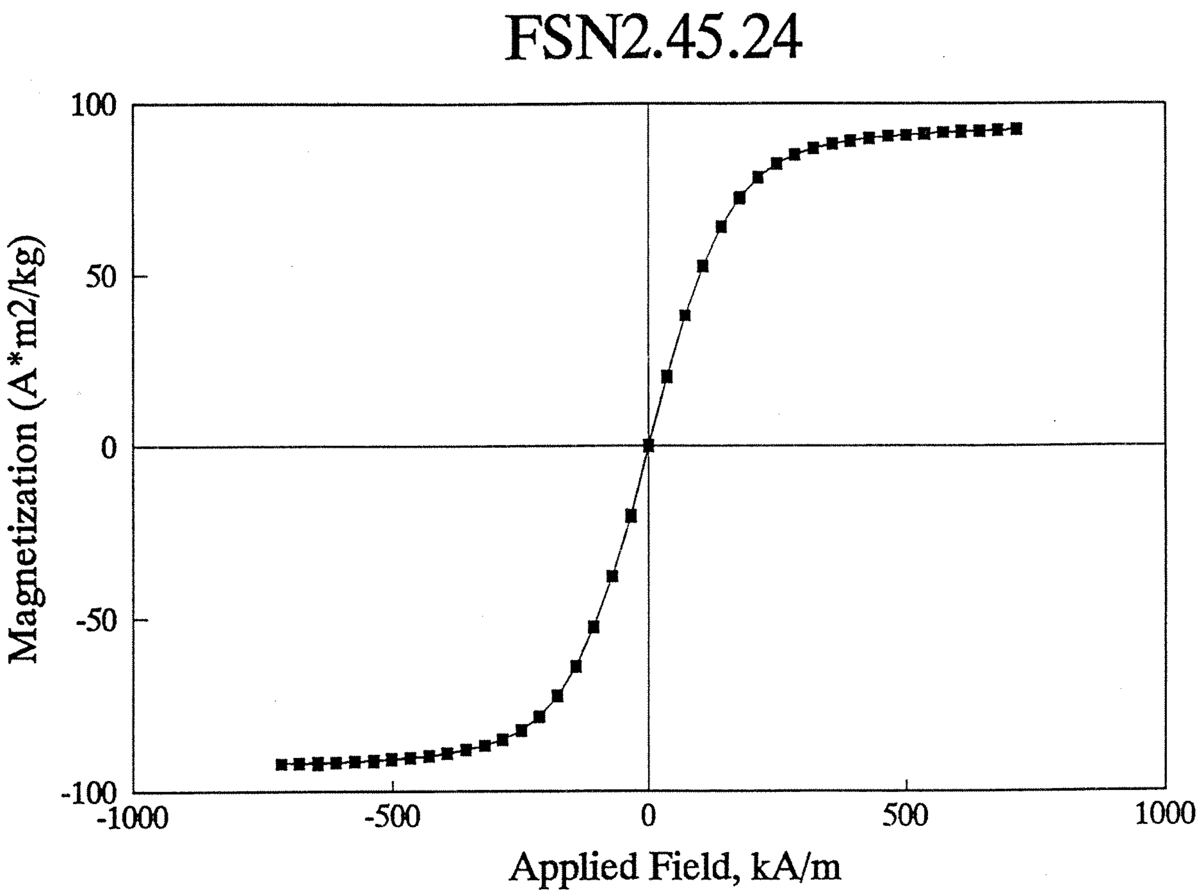

Figure C.1 Hysteresis loop (large scale) for $(Fe_3Si)_{0.95}Nb_{0.05}$ nanocrystalline alloy after annealing at 450 °C for 24 hours.

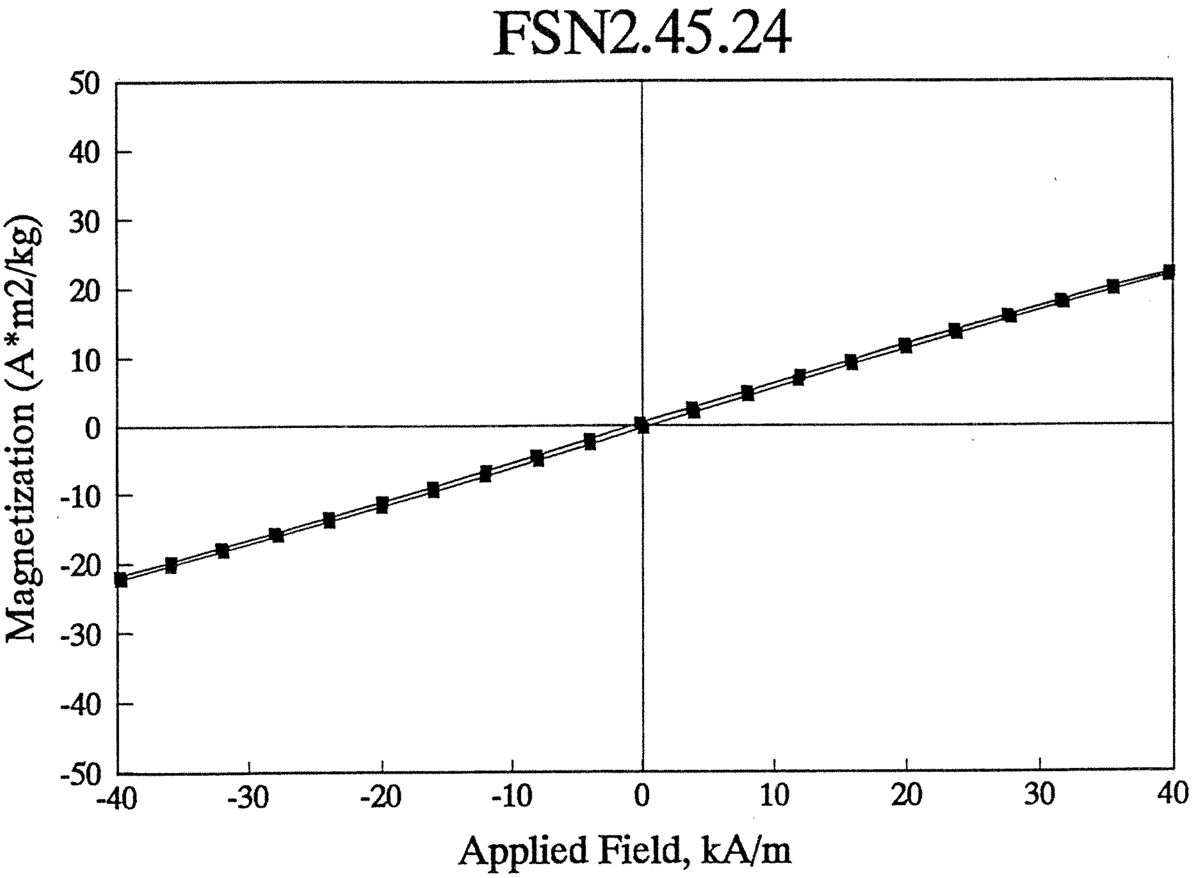

Figure C.2 Hysteresis loop (small scale) for $(Fe_3Si)_{0.95}Nb_{0.05}$ nanocrystalline alloy after annealing at 450 °C for 24 hours.

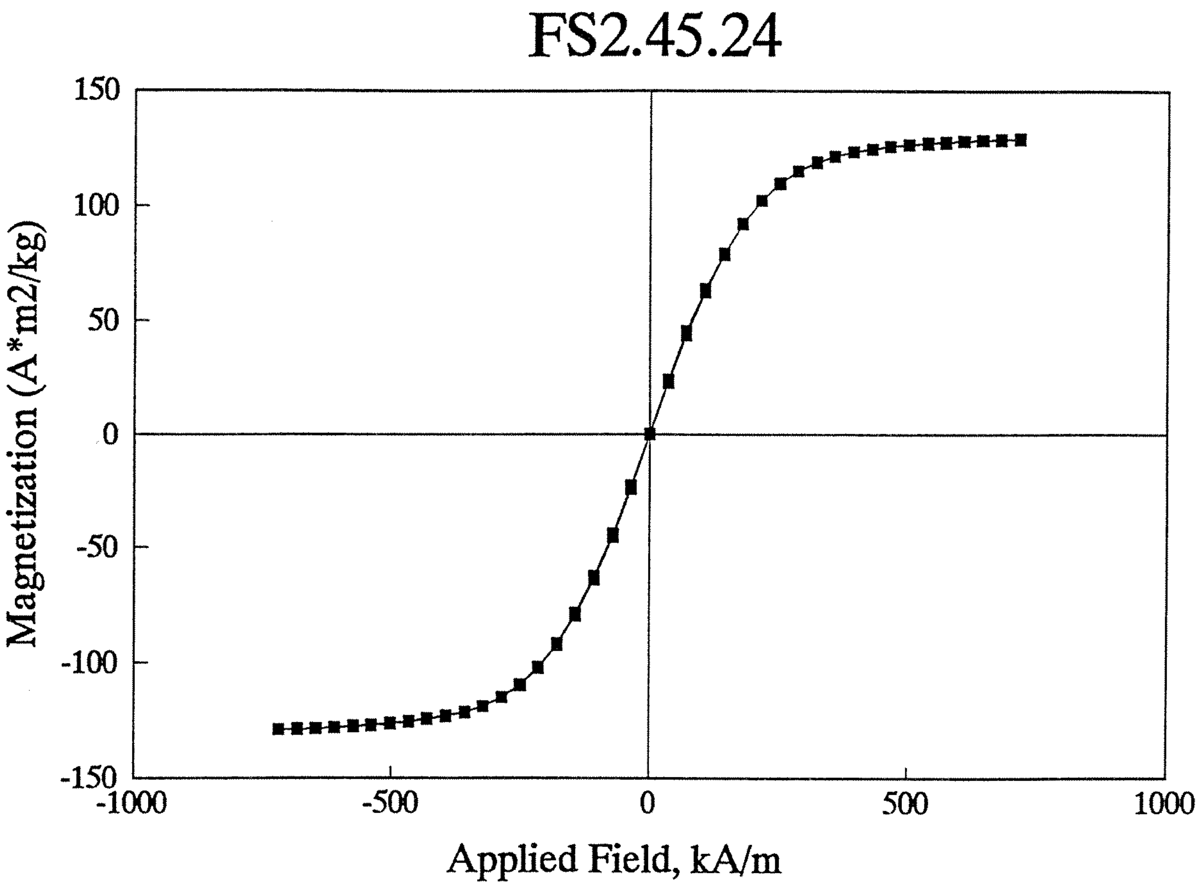

Figure C.3 Hysteresis loop (large scale) for Fe_3Si nanocrystalline alloy after annealing at 450 °C for 24 hours.

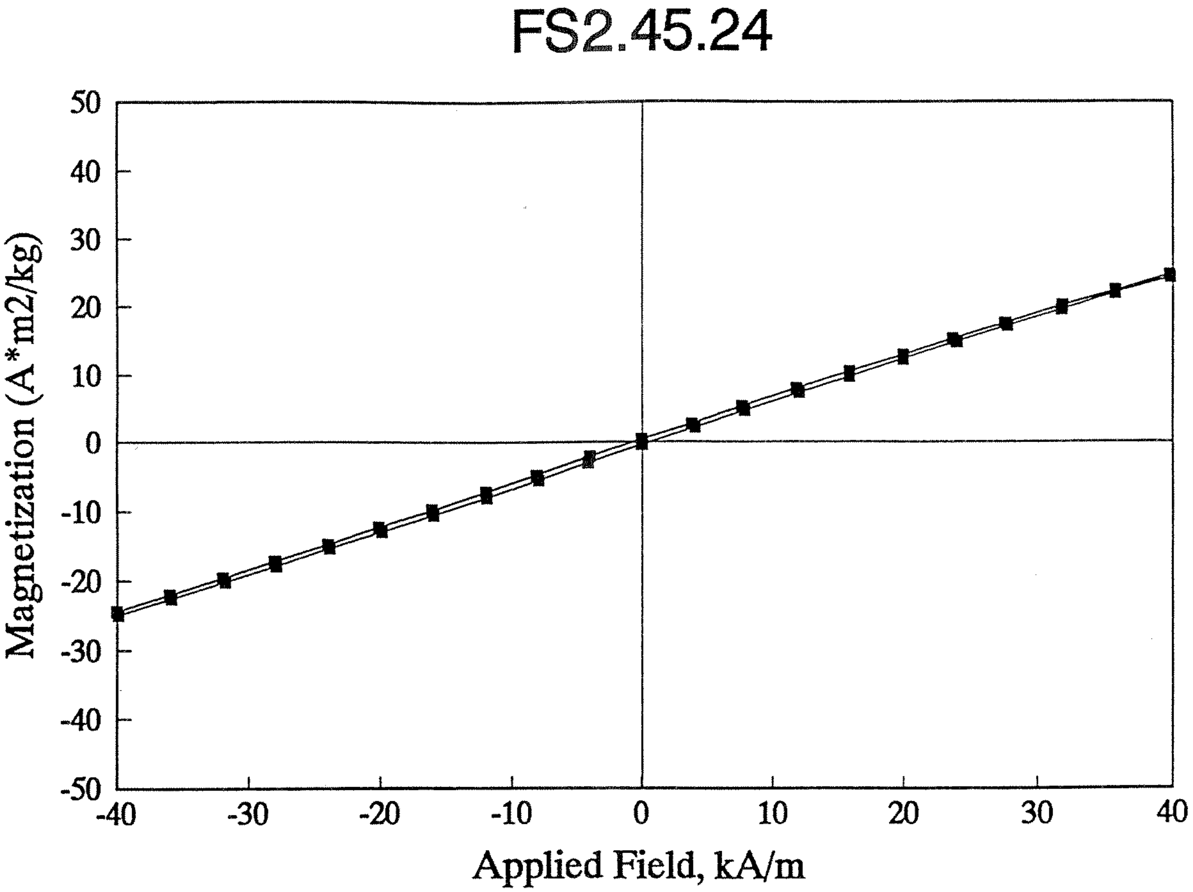

Figure C.4 Hysteresis loop (small scale) for Fe_3Si nanocrystalline alloy after annealing at 450 °C for 24 hours.